Low-level turbulence characteristics over inhomogeneous surface during wintertime

Babić, Karmen

UNIVERSITY OF ZAGREB

FACULTY OF SCIENCE

DEPARTMENT OF GEOPHYSICS

Karmen Babić

LOW-LEVEL TURBULENCE CHARACTERISTICS OVER INHOMOGENEOUS SURFACE DURING WINTERTIME

DOCTORAL THESIS

Zagreb, 2016

UNIVERSITY OF ZAGREB

FACULTY OF SCIENCE

DEPARTMENT OF GEOPHYSICS

Karmen Babić

LOW-LEVEL TURBULENCE CHARACTERISTICS OVER INHOMOGENEOUS SURFACE DURING WINTERTIME

DOCTORAL THESIS

Supervisor: Prof. dr. Zvjezdana Bencetić Klaić

Zagreb, 2016

SVEUČILIŠTE U ZAGREBU
PRIRODOSLOVNO-MATEMATIČKI FAKULTET
GEOFIZIČKI ODSJEK

Karmen Babić

KARAKTERISTIKE PRIZEMNE TURBULENCIJE ZIMI IZNAD NEHOMOGENE PODLOGE

DOKTORSKI RAD

Mentor: prof. dr. sc. Zvjezdana Bencetić Klaić

Zagreb, 2016.

Low-level turbulence characteristics over inhomogeneous surface during wintertime

Doctoral Thesis

in Meteorology

Submitted to the
Faculty of Science, Department of Geophysics
of the
University of Zagreb

in Partial Fulfillment of the Requirements for the Degree of
Doctor of Natural Science

by
Karmen Babić

Advisor
Prof. Dr. Zvjezdana B. Klaić

Zagreb, September 2016

This thesis was made under the supervision of prof. dr. Zvjezdana Bencetić Klaić as a part of the doctoral study at the Department of Geophysics, Faculty of Science, University of Zagreb.

Ovaj rad u potpunosti je izrađen na Geofizičkom odsjeku Prirodoslovno-matematičkog fakulteta Sveučilišta u Zagrebu. Mentorica prof. dr. sc. Zvjezdana Bencetić Klaić redovita je profesorica na Geofizičkom odsjeku Prirodoslovno-matematičkog fakulteta Sveučilišta u Zagrebu.

List of Abbreviations

ABL	Atmospheric Boundary Layer
BL	Boundary Layer
CL	Canopy Layer
DFT	Discrete Fourier Transform
FFP	Flux Footprint Prediction
FFT	Fast Fourier Technique
FP	Fourier Period
FT	Fourier Transform
HHF	Horizontally Homogeneous and Flat
IBL	Internal Boundary Layer
IEL	Internal Equilibrium Layer
IS	Inertial Sublayer
LES	Large Eddy Simulation
MFD	Multiresolution Flux Decomposition
MOST	Monin-Obukhov Similarity Theory
MR	Multiresolution
NBL	Nocturnal Boundary Layer
PF	Planar Fit
RSL	Roughness Sublayer
SBL	Stable Boundary Layer
SL	Surface Layer
TKE	Turbulent Kinetic Energy
WT	Wavelet Transform

Abstract

In this dissertation, the local similarity scaling approach was examined based on the multi-level measurements of atmospheric turbulence in the wintertime (December 2008 – February 2009) stable atmospheric boundary layer (SBL) established over a heterogeneous surface influenced by mixed agricultural, industrial and forest surfaces. The 62 m tower (levels 20, 32, 40, 55 and 62 m above ground) was situated in the middle of some 120 m $\times$ 480 m area of $h_c = 18$ m high walnut trees. The heterogeneity of the surface was characterized by spatial variability of both roughness and topography.

In a first step local similarity theory in terms of flux-variance and flux-gradient relationships was investigated. Nieuwstadt's local scaling approach was found to be suitable for the representation of all three wind velocity components. The roughness sublayer (RSL) influenced wind variances, and consequently the turbulent kinetic energy (TKE) and correlation coefficients at the lowest measurement level, but not the wind shear profile. After removing data points associated with the flux Richardson number (Rf) greater than 0.25, the observations support the classical linear expressions for the dimensionless wind shear (ϕ_m) even over inhomogeneous terrain. Leveling-off of ϕ_m at higher values of stability parameter was found to be a result of the large number of data characterized by small-scale turbulence ($Rf > 0.25$). Deviations from linear expressions were shown to be mainly due to small-scale turbulence rather than due to the surface heterogeneities, supporting the universality of the linear relationship. Additionally, the flux-gradient dependence on stability did not show different behavior for different wind regimes, indicating that the stability parameter is a sufficient predictor for flux-gradient relationships. Data followed the local z-less scaling for ϕ_m when the prerequisite $Rf \leq 0.25$ was imposed.

Further investigations focused on the combined influence of the RSL found above tall vegetation and the internal boundary layer (IBL) on the turbulence spectral characteristics and TKE budget. The traditional surface layer scaling was tested against the canopy scaling, which is generally valid for the RSL. It was found that canopy scaling can be successfully applied even within the transition layer. For the present complex site local isotropy was not found. Vertical velocity spectra were smaller than horizontal spectra. Similarly, dissipation rates (ε) determined

only from vertical spectra were smaller than ε estimates based on horizontal components. Therefore, it was necessary to normalize vertical wind speed spectra with ϕ_{ε_w} in order to get good correspondence with the Kansas spectral models. Extending the analysis to the Olesen approach, applied for the first time to the SBL over heterogeneous terrain, normalized spectra collapsed to one single curve.

Finally, analyzing the budget terms of the TKE equation, non-equilibrium conditions were found. The non-local dynamics are considered to be the main reason for the observed imbalance of TKE in the transition layer as well as for the observed breakdown of z-less regime in the strongly stable conditions above heterogeneous surface. In the RSL, the turbulent transport of TKE above vegetated canopies is considered to be the main cause of the observed TKE imbalance in the neutral conditions. A less systematic behavior of the residual term was observed indicating that the advection term has more pronounced influence on the RSL than the upper levels.

Key words: Stable boundary layer; Local scaling; Forest canopy; Roughness sublayer; Turbulent kinetic energy; Spectral models; TKE budget

Table of Contents

Chapter 1

Introduction

1.1 Motivation

Stable atmospheric boundary layers (SBLs) are influenced by many independent forcings, such as, (sub)mesoscale motions, which act on a variety of time and space scales, net radiative cooling, temperature advection, surface roughness and surface heterogeneity (e.g. Mahrt 2014), enhancing the complexities and posing challenges in the study of the SBL. The fate of pollutants in the boundary layer (BL) is strongly affected by turbulence which is extremely complicated over complex terrain. Moreover, due to weak turbulence the SBL is generally favorable for the establishment of air pollution episodes. Therefore, investigations of its characteristics are of the great importance.

In the scientific community substantial effort was made to address Monin-Obukhov similarity theory (MOST) in different conditions. Most of observational studies are based on measurements from a single tower, and sometimes they result in inconsistent conclusions on the applicability of similarity theory. These inconsistencies are mostly found for studies of MOST in complex terrain (e.g. de Franceschi et al. 2009; Martins et al. 2009; Nadeau et al. 2013; Kral et al. 2014) or for small scale turbulence for which z-less scaling regime should apply (e.g. Forrer and Rotach 1997; Pahlow et al. 2001; Cheng and Brutsaert 2005; Basu et al. 2006; Grachev et al. 2013). Most of atmospheric dispersion models, used for the air quality studies, as well as high-resolution regional climate models use similarity scaling to model flow characteristics and dispersion in such environments.

While many studies of turbulence characteristics within the roughness sublayer (RSL) over homogeneous tall forest canopies can be found in the literature, observational studies of turbulence above heterogeneous and patchy vegetation canopies are very scarce. Results of such field observations can be used for the validation of large eddy simulations (LES), which enable studies of transitions across changes in

land cover and influence on turbulent fluxes (Mammarella et al. 2008).

The relative importance of physical processes that govern turbulent fluid motions is illustrated in the turbulence kinetic energy (TKE) budget. The presence of a plant canopy will modify the BL near surface in a unique fashion by imposing aerodynamic drag on the flow and by creating turbulent motions in wakes of a plant element which adds further dimension to the balance of TKE (Dwyer et al. 1997). The overall goal of this thesis is to contribute to better understanding of still not completely explained turbulence characteristics over heterogeneous surface.

1.2 State of Research

1.2.1 Similarity Theory

Monin-Obukhov similarity theory (Obukhov 1946; Monin and Obukhov 1954) relates surface turbulent fluxes to vertical gradients, variances and scaling parameters. The assumptions underlying MOST include stationary atmospheric turbulence, surface homogeneity and the existence of an inertial sublayer (that is, surface layer, SL). Relations between these parameters (Businger et al. 1971; Dyer 1974) are based on several experimental campaigns conducted over horizontally homogeneous and flat (HHF) surfaces (e.g. Kaimal and Wyngaard 1990), where the original assumptions are considered to be met. Originally, MOST was based on surface fluxes, which were assumed to be constant with height, and equal to surface values within the SL (also referred to as constant-flux layer). In the unstable boundary layer, MOST has been extensively studied and proven useful in relating turbulent fluxes to profiles (Businger et al. 1971; Wyngaard and Coté 1972; Dyer 1974). However, the applicability of MOST in the stable SL (e.g. Mahrt 1998; Cheng et al. 2005; Trini Castelli and Falabino 2013) and over complex (e.g. Nadeau et al. 2013; Stiperski and Rotach 2016; Babić et al. 2016b) and heterogeneous surfaces is still an open issue due to many difficulties when applying traditional scaling rules since MOST assumptions may not be fulfilled.

Nieuwstadt (1984) extended Monin-Obukhov similarity in terms of a local scaling approach. This regime represents the extension of MOST above the SL. Accordingly, all MOST variables are based on the local fluxes at a certain height z instead of using surface values. As MOST should be valid over flat and homogeneous terrain, studies of the SBL in terms of SL and local scaling approaches were made over areas characterized by long and uniform fetch conditions, such as, Greenland, Arctic pack ice and Antarctica (e.g. Forrer and Rotach 1997; Grachev et al. 2007, 2013; Sanz Rodrigo and Anderson 2013). Forrer and Rotach (1997) concluded that local scaling is superior over SL scaling. This was mainly due to the fact that SL over

an ice sheet, with continuously stable stratification, can be very shallow (< 10 m). Moreover, for cases of strong stability, non-dimensional similarity functions for momentum and heat were in agreement with the results obtained from the local scaling approach. Grachev et al. (2013) examined limits of applicability of local similarity theory in the SBL by revisiting the concept of a critical Richardson number.

Although the above mentioned complexities make the attempt to classify the SBL incomplete, many different classification schemes for different types of SBL have been proposed (e.g. Holtslag and Nieuwstadt 1986; Mahrt 1998; Cheng and Brutsaert 2005; Grachev et al. 2005; Sorbjan and Grachev 2010; Mahrt 2014; Liang et al. 2014). The most commonly used are those schemes which distinguish between weakly and strongly stable regimes and describe changes with increasing stability. In the weakly stable regime, turbulence is continuous in both space and time due to atmospheric conditions associated with overcast sky or significant wind shear. If non-stationarity and heterogeneity effects are excluded, turbulence in this regime generally follows similarity theory (e.g. Mahrt 2014). On the other hand, the very stable regime is characterized with weak winds and strong stratification. These lead to weak, intermittent and sporadic turbulence, and break down of similarity relationships (e.g. Acevedo et al. 2008; Martins et al. 2009). However, the distinction between weakly and strongly stable regimes does not consider all complexities of the SBL, such as, intermittency (Salmond 2005) which is defined in terms of internal intermittency (resulting from interactions between turbulence and wind shear) and external intermittency (forced by non-stationary (sub)meso motions, e.g. Mahrt 2014). A variety of non-stationary (sub)meso motions causing intermittent turbulence includes gravity waves (e.g. Cheng et al. 2005), low-level jets (e.g. Cheng et al. 2005; Banta et al. 2006; van de Wiel et al. 2010), density currents (e.g. Sun et al. 2002), wave-like motions (e.g. Fritts et al. 2003; Nappo 2012), Kelvin-Helmholtz instability (e.g. Cheng et al. 2005) and many others. Majority of the above mentioned studies in complex terrain are mainly characterized by homogeneous surface roughness, while studies over heterogeneous and patchy vegetation are still scarce.

Even modest surface heterogeneity can significantly influence the nocturnal boundary layer (NBL) and lead to turbulence at higher Richardson numbers in comparison with homogeneous surfaces (Derbyshire 1995). Since the Earth's solid surfaces are mainly heterogeneous, the interest in flow and turbulence characteristics over complex surfaces has increased in recent decades. Moreover, a proper representation of turbulence is particularly important for parameterization of surface-atmosphere exchange processes in atmospheric models, such as dispersion (e.g. Enger and Koračin 1995), numerical weather prediction (e.g. Horvath et al. 2012) or regional climate models (e.g. Güttler et al. 2014). The turbulence characteristics have been studied through direct measurements for different complex surfaces including,

complex forest sites (e.g. Rannik 1998; Dellwik and Jensen 2005; Nakamura and Mahrt 2001), agricultural fields, such as, apple orchard (de Franceschi et al. 2009) or rice plantation (Moraes et al. 2005), metre-scale inhomogeneity (e.g. Andreas et al. 1998), urban areas (e.g. Wood et al. 2010; Fortuniak et al. 2013), and complex mountainous terrains (e.g. Rotach et al. 2008), addressing to both valley floors (e.g. Koračin and Enger 1994; Rotach et al. 2004; Moraes et al. 2005; de Franceschi et al. 2009) and steep slopes (Nadeau et al. 2013; Stiperski and Rotach 2016). However, most of these studies are associated with flows over homogeneous surfaces. In recent years much effort has been put into simulations of turbulent fluxes over relatively heterogeneous surfaces using LES. Bou-Zeid et al. (2007) used LES over surfaces with varying roughness lengths to assess the parameterization for the equivalent surface roughness and the blending height[1] in the neutral boundary layer at regional scales. Large eddy simulations of surface heterogeneity effects on regional scale fluxes and turbulent mixing in the SBLs were studied by Stoll and Porté-Agel (2009); Mironov and Sullivan (2010); Miller and Stoll (2013).

The vertical structure of the atmospheric boundary layer (ABL) is traditionally partitioned into a SL, an outer layer and the entrainment zone (e.g. Mahrt 2000). The SL, in turn, is subdivided into a canopy layer (CL), a roughness sublayer (RSL) and inertial sublayer. Over surfaces with small roughness elements the latter, which corresponds to the true equilibrium layer, is often identified with SL. These concepts are less applicable over heterogeneous surfaces but for the SBL they provide, nevertheless, a useful starting point. Above very rough surfaces, such as forests or agricultural crops, the RSL has a non-negligible extension. Due to the influence of individual roughness elements on the flow within the RSL, MOST is not widely accepted (e.g. Katul et al. 1999; Finnigan 2000). The existence of large-scale coherent turbulent structures within the RSL, which are generated at the canopy top through an inviscid instability mechanism (Raupach et al. 1996), is thought to be a reason for the failure of standard flux-gradient relationships (Harman and Finnigan 2007).

1.2.2 Spectral characteristics

Besides the mean variables and variances, spectral (and cospectral) characteristics of turbulence can be described within the framework of similarity theory. A classical references and most commonly used (co)spectral models in the SL over ideal HHF terrain are those of Kaimal et al. (1972) and Wyngaard and Coté (1972) obtained from the Kansas experiment. They found that with appropriate normalization, both the spectra and cospectra reduce to a family of curves which collapse to a single universal curve in the inertial subrange, while at low frequencies they show

[1] The height at which surface and local disturbances have been blended out (Wieringa 1976; Bou-Zeid et al. 2004).

dependence on the stability parameter. These results were based on 15 1-hr runs, 10 of which were unstable and 5 were stable. The universal functions obtained in this and following experiments over homogeneous and flat surfaces have led to well established (co)spectral turbulence characteristics. In some of the early observational and wind-tunnel studies of spectra and cospectra (Shaw et al. 1974; Raupach 1981; Anderson et al. 1986; Baldocchi and Meyers 1988; Amiro 1990; Brunet et al. 1994; Shaw et al. 1995) the emphasis was on comparison of spectra within and above the canopies. Moreover, the above canopy spectra were not analyzed in the same way as those over HHF terrain as reported by Kaimal et al. (1972).

In the past two decades, models of Kaimal were applied for other types of surfaces such as forest (e.g. Liu et al. 2001; Su et al. 2004; Mammarella et al. 2008) and urban areas (e.g. Roth 2000; Fortuniak and Pawlak 2015), but such studies are still sparse. Recent research efforts have focused on investigating departure of spectra measured in the RSL from the flat terrain shapes and scaling relationships. Liu et al. (2001) have used sonic anemometer data from two levels, one within and another above a uniform forest canopy, which covered an area of about 8000 km^2 and was composed of conifer and deciduous-mixed forest. They have found that normalized turbulent spectra have $-2/3$ slopes within the inertial subrange and the shapes of spectra were in good agreement with those of Kaimal. However, their results showed that turbulence was approximately isotropic within the canopy and anisotropic above the canopy. Additionally, compared to the flat terrain results, the velocity and temperature spectral peaks were shifted toward higher frequencies and TKE dissipation rates were much larger inside and above the canopy. They attributed the distinct features of their results to the dynamic forcing caused by the rough forest canopy surface. Su et al. (2004) investigated turbulence spectra and cospectra above the forest canopy of two mixed hardwood forest based on the long-term (nearly 40 000-hr runs) eddy-covariance measurements. They found different (co)spectral constants and stability functions needed to normalize and collapse (co)spectra in the inertial subrange compared to those of Kaimal et al. (1972). Opposed to these two studies which presented spectral turbulence characteristics for different stabilities, Mammarella et al. (2008) studied turbulence spectra of the near-neutral flow over two deciduous forest sites with short and long fetch sectors. For the short fetch sectors, turbulence spectra within and above the RSL showed a good collapse of spectral peaks when scaled by fixed length and velocity scales. The analysis for the long fetch case revealed that the RSL influence disappeared far from the canopy top and the traditional SL scaling was found to be valid.

For different types of applications most often used spectral models are those proposed by Kaimal et al. (1972). However, Olesen et al. (1984) have also proposed simple spectral models for all three velocity components in the SBL. These models

use non-dimensional wind shear and TKE dissipation rate similarity functions to normalize the spectra so that they adhere to one curve only irrespective of static stability. Their models were based on the Kansas and Minnesota experiments, and the SL scaling approach. Forrer (1999) extended this regime to the local scaling and applied it to the data collected over nearly ideal snow-covered surface of the Greenland ice sheet. Interestingly enough, the validity of these spectral models over more complex vegetated surfaces has not yet been reported in the literature.

1.2.3 Turbulent Kinetic Energy (TKE) Budget

Within the framework of the similarity theory the TKE budget can be investigated. Indeed, determining stability functions of the TKE budget terms has been one of the objectives in the field of boundary layer turbulence over the past forty years (e.g. Businger et al. 1971; Wyngaard and Coté 1971; Högström 1990; Oncley et al. 1996; Frenzen and Vogel 2001; Li et al. 2008; Duarte et al. 2015). Since the milestone Kansas 1968 experiment, many field campaigns were conducted which enabled deeper understanding of the behavior of different terms in TKE budget. The classical assumption for the SL measurements above HHF surfaces was that the TKE budget is locally balanced, i.e. the production from shear (and buoyancy in unstable conditions) will be dissipated locally over all stabilities, while transport terms are either negligible or they cancel each other (McBean and Elliot 1975; Wyngaard 2010). Wyngaard and Coté (1971) found local imbalance of TKE over wide range of stabilities, but still suggested local balance under neutral conditions. However, recent studies have challenged this assumption for all stabilities, showing that TKE is locally imbalanced and that transport terms are important (e.g. Högström 1990; Oncley et al. 1996; Frenzen and Vogel 2001; Pahlow et al. 2001; Li et al. 2008). These studies have found either excess or inadequate TKE dissipation, suggesting TKE gain or loss via transport terms, respectively. Högström (1990) argued that the excess of TKE dissipation in the neutral SL is connected to the so-called inactive turbulence which is transported to SL from the upper regions via pressure transport. Further, Högström et al. (2002) introduced a theory based on 'top-down' dynamic of detached eddies in order to explain the excess dissipation in the neutral SL. While the proposed theories may explain excess TKE dissipation, adequate explanation for the insufficient local dissipation is still missing. Li et al. (2008) have pointed out that the reason why results of observational studies regarding TKE balance differ among each other is still an open question.

This problem is especially emphasized in the SBL, where turbulence is influenced by many other factors such as, low-level jets (LLJs), gravity waves, density currents or Kelvin-Helmholtz shear instability (e.g. Cheng et al. 2005). The analysis

of TKE budget terms under the effect of LLJs has shown that the pressure transport term plays an important role close to the surface, but a consensus on whether the pressure transport is the source or sink term is still missing (Duarte et al. 2015, and references therein). A considerable amount of research has been done on TKE budget studies in the SL over homogeneous surfaces but little research focused on budgets above heterogeneous and rough surfaces (e.g. Christen et al. 2009). The first studies of TKE budgets within and above plant canopies were mainly focusing on turbulence characteristics within the canopy. Leclerc et al. (1990) and Meyers and Baldocchi (1991) analyzed TKE budgets within and above a deciduous forest canopy, while Brunet et al. (1994) and Raupach et al. (1996) used wind-tunnel studies to investigate the air flow within and above plant canopy. Dwyer et al. (1997) used LES of flow through and above a forest in order to calculate all the terms in the TKE budget equation with special emphasis on the role of the pressure transport term. The above mentioned studies have highlighted that turbulent and pressure transport terms were mostly responsible for the absence of the local equilibrium within the RSL. Some of the rare studies on TKE budgets above fetch-limited forests, such as those of Mammarella et al. (2008) and Yang et al. (2006) were focused on statically neutral conditions. A general missing piece in the literature are the studies of the TKE budget terms above heterogeneous surfaces in the SBL.

1.3 Research Objectives

The overall objective of this thesis is to address some of the open questions introduced above by applying local scaling approach when investigating turbulence characteristics in the SBL above an inhomogeneous surface. Multi-level turbulence observations were performed over heterogeneous terrain influenced by a mixture of forest, agricultural and industrial surfaces. These measurements are used to study applicability of the local similarity theory in the wintertime SBL, as well as spectral turbulence characteristics and budgets of the TKE. However, prior to investigating turbulence characteristics, an analysis of scales of motion in the SBL was necessary in order to adequately determine appropriate averaging time scales for calculation of turbulent fluctuations and turbulent fluxes. For this purpose, four different methods were used, two of which are based on Fourier spectral analysis and the other two on wavelet analysis. The main scientific objectives of this thesis are:

- **To examine the applicability of local similarity scaling in terms of flux-variance and flux-gradient relationships in the NBL over inhomogeneous surface.** Here the analysis is focused on investigating how heterogeneous surface influences wind variances and mean wind speed gradient and their stability dependence. The validity of the z-less regime is tested

for strongly stable conditions. Stability dependence of the dimensionless wind shear is compared to the respective flux-gradient relationships from the literature. Turbulence characteristics in the sub- and supercritical regimes are presented. The vertical extent of the tall canopy to which it influences measurements is determined.

- **To investigate turbulence spectral characteristics and TKE dissipation rate within and above the roughness sublayer.** The validity of the local isotropy hypothesis is tested for measurements above an inhomogeneous surface. The stability function of the dimensionless TKE dissipation is compared with the most commonly used formulations from the literature and a modified relationship is proposed. The appropriate scaling parameters needed to collapse spectra are obtained. Spectra obtained in this study are compared with the existing models which are valid for HHF terrain.

- **To determine the influence of tall canopy and heterogeneous surface cover on the TKE budget terms.** The dimensionless TKE budget terms are analyzed for the RSL and transition layer separately. For each of the terms parameterizations are proposed. Different dynamical properties of the two layers are highlighted.

The reminder of this thesis is structured as follows. In Chapter 2, a short theoretical background is given. In Chapter 3, experimental set-up and measurement site, extensive post-processing steps and analysis methods are described, while Chapter 4 presents results of the timescales analysis. In Chapters 5 and 6 the main objectives are addressed, including the applicability of the local similarity theory, the analysis of turbulence spectral characteristics and dissipation rates, and the analysis of TKE budget terms within and above the forest RSL. Summarizing conclusions and general outlook are drawn in Chapter 7.

Chapter 2

Theoretical Background

2.1 Stable Boundary Layer

The mean and turbulent characteristics of the ABL play an important role in determining the transportation, storage and dispersion of atmospheric pollutants. The BL is a part of the atmosphere that responds directly to the flows of mass, energy and momentum from the Earth's surface at time scales of an hour or less (e.g. Stull 1988, Fig. 2.1). The SBL develops when net radiation becomes negative due to radiative cooling of the layers close to the Earth's surface. The structure of the SBL is primarily determined by atmospheric static stability and processes governing mechanical generation of turbulence, such as, wind shear from synoptic or terrain induced flows or low-level jets (e.g. Stull 1988). These processes operate at a variety of different heights and scales within BL and their dominance can vary in time and space. Thus, equilibrium or steady-state conditions are rare. As a result, NBL may range from fully turbulent (e.g. Conangla et al. 2008) to intermittently turbulent (e.g. Mahrt 1998; Sun et al. 2002) or even non-turbulent (e.g. van de Wiel et al. 2003, 2007). Our current understanding of turbulence in the NBL has been slowly developing, largely due to the significant challenges associated with studying the NBL from observational, analytical and theoretical perspectives. Although individual field studies may be considered site specific, a number of authors have tried to address a research gap by field studies of the SBL, which have yield some important insights into the structure of processes operating in the NBL.

The classification of NBL regimes is difficult and often impossible due to the fact that a particular night over the land does not fit into a certain prototype (Mahrt 1999). Any attempt to classify a complex SBL is necessarily oversimplified. Therefore, the SBL over land is usually classified according to the strength of the thermal stratification ranging from weakly to very stable regime (e.g. Mahrt 1998; Mauritsen et al. 2007; Mauritsen and Svensson 2007). The weakly stable regime (Fig.

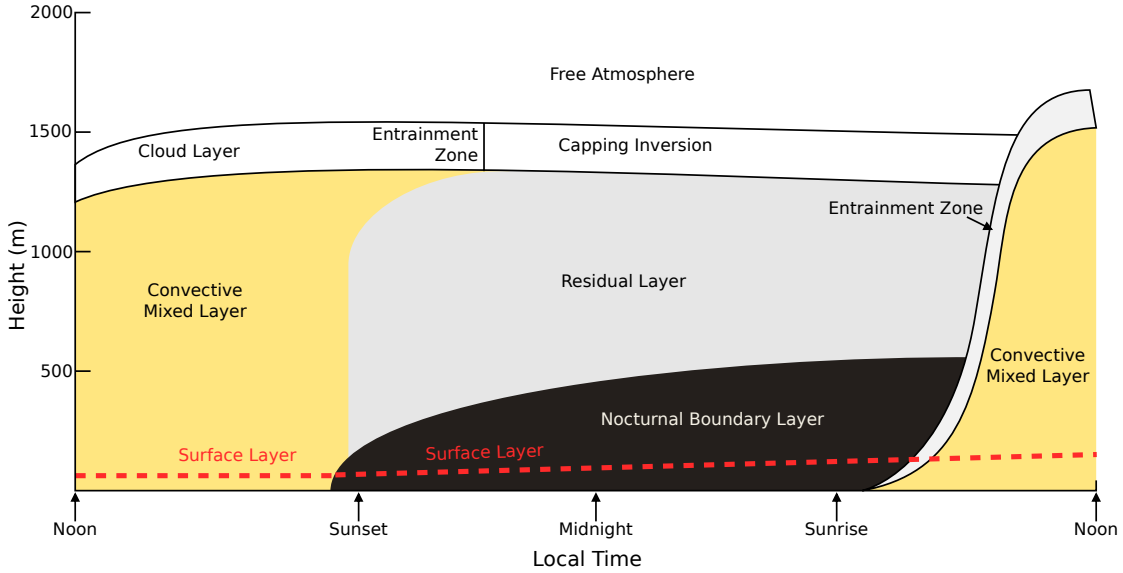

Figure 2.1: Schematic representation of the atmospheric boundary layer over land (adapted from Stull (1988)).

2.2a) occurs in conditions of moderate to strong winds leading to the mechanical production of relatively strong turbulence and mixing, or in situations with overcast skies which reduce the radiative cooling of the Earth's surface. In this regime the gradient Richardson number (Ri), which is a dynamical measure of the flow stability and is described in more detail in Section 2.2, is usually below its critical value, indicating continuous turbulence of moderate intensity which decreases with height. The weakly stable regime is the usual textbook example of the SBL with a well-defined top, and has been analyzed in terms of measurements, scaling arguments, similarity theory, laboratory studies and numerical modelling. In case of light winds and clear skies (under e.g. anti-cyclonic conditions) or due to warm advection, the stable stratification increases and allows intense surface radiative cooling and weaker turbulence. This results in a strongly stable regime (Fig. 2.2b), which is largely determined by local effects, such as orography or the terrain characteristics and heterogeneities (Mahrt et al. 2001; Sun et al. 2002; Cuxart et al. 2007). In the case of very strong stratification, turbulence becomes intermittent, detached from the surface or even totally suppressed. Ri is usually above the critical value and turbulence intensity often increases with height indicating that factors which generate turbulent mixing are acting above the surface layer. This induces downward turbulent transport and gives rise to the "upside-down" boundary layer (Mahrt 1998, 1999). Consequently, it is difficult to define the SBL height.

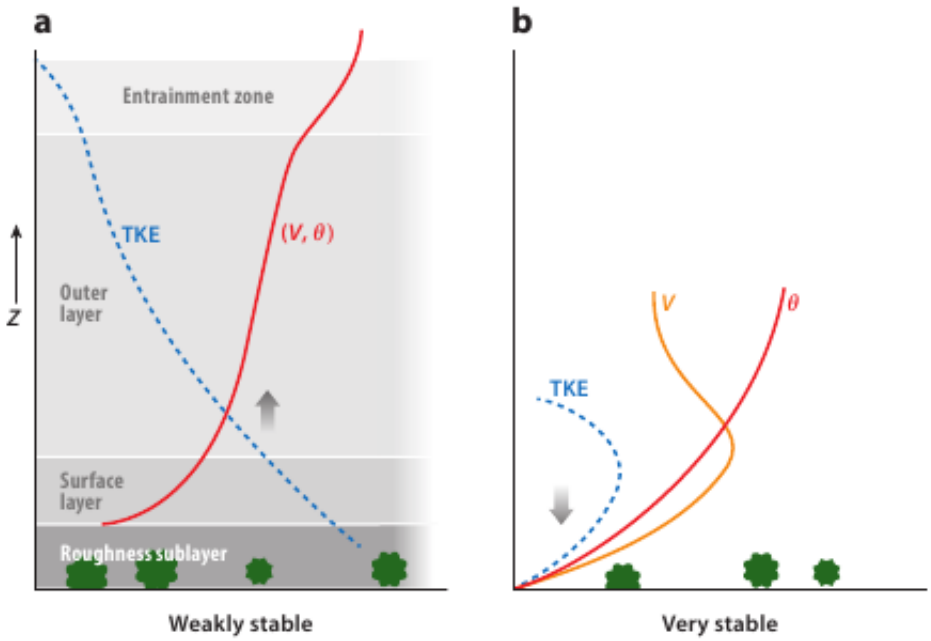

Figure 2.2: A simplified classification of the SBL into **(a)** weakly and **(b)** strongly stable regime (adopted from Mahrt (2014)). Vertical profiles of the wind speed (V), potential temperature (θ) and TKE are shown. **(a)** The vertical structure corresponding to the well-defined weakly stable regime. The gray arrow indicates the usual direction of the vertical transport of turbulence energy. **(b)** One of many different vertical structures of the very stable BL.

2.2 Similarity theory

The basic assumption of similarity theory is that the structure of the ABL can be described in terms of some characteristic parameters. Similarity theory is based on the organization of variables into dimensionless groups (e.g. Stull 1988). This is done by the dimensional analysis procedure called *Buckingham π theorem*. A proper choice of dimensionless groups should allow us to form empirical relationships between them, and these relationships should be universal, i.e. they will be valid everywhere all the time for the studied situation. Development of a similarity theory consists of four key steps:

1. selection of the relevant (key) variables
2. organization of variables into dimensionless groups
3. determination of the values of the dimensionless groups from experimental data
4. description of the relationship between groups.

This four-step procedure results in an empirical equation or a set of curves which show the same shape. Since these curves look self similar, therefore the name similarity theory. These empirical equations usually contain unknown coefficients, which

are obtained by regression against the observations. Finally, these equations are called similarity relationships. The key variables which usually appear in classes of similarity problems are called scaling variables for that class. Well-defined classes of similarity scaling are Monin-Obukhov similarity, mixed-layer similarity, local similarity, local free convection and Rossby-number similarity. Each of these classes is associated with specific scaling variables.

2.2.1 Local similarity scaling

Holtslag and Nieuwstadt (1986) presented an overview of scaling regimes for the SBL (Fig. 2.3). Each of the scaling regimes is characterized by different scaling parameters. The turbulence in the horizontally homogeneous SL can be described by MOST with surface fluxes of heat and momentum and the height z as scaling parameters. In this layer the relevant scaling parameter is the Obukhov length L (Obukhov 1946), given by

$$L = -\frac{u_*^3}{k\frac{g}{\overline{\theta_v}}(\overline{w'\theta_v'})_s}, \tag{2.1}$$

where $u_* = (\overline{u'w'}_s^2 + \overline{v'w'}_s^2)^{1/4}$ is the surface friction velocity, $(\overline{w'\theta_v'})_s$ is the surface kinematic heat flux, $\overline{\theta_v}$ is the virtual potential temperature, g is the acceleration due to the gravity, $k \approx 0.4$ is the von Kármán constant. Overbars and primes denote time averaging and fluctuating quantities, respectively. The SL is commonly defined as the region where turbulent fluxes and stress vary by less than 10 % of their surface values (Monin and Obukhov 1954) and it is often referred to as the constant flux layer. In this layer, z/L is considered a valid stability parameter. The physical meaning of the Obukhov length is that it represents the height above ground where an equilibrium condition is reached between the buoyant effects and mechanical production of turbulence. In the SBL, the buoyant suppression of turbulence is increasing with increasing stability, thus putting great importance on the shear production of turbulence to the flow in this layer of decreasing thickness, L. Hence, for increasing static stability we have a shorter Obukhov length and higher stability parameter.

Above the SL, the local scaling regime applies, a regime proposed by Nieuwstadt (1984). According to Nieuwstad's local similarity approach, properly scaled turbulence statistics should solely be a function of the local stability parameter $\zeta_\ell = (z - d)/\Lambda$, where z is the measurement height, d is zero-plane displacement height and Λ is the local Obukhov length. Even if Nieuwstadt (1984) was not referring to rough surfaces, we have introduced d as we will be concerned with data from a site where the canopy height is non-negligible. In the local scaling framework, the

local Obukhov length is based on the local fluxes at height z and varies with height

$$\Lambda(z) = -\frac{u_{*\ell}^3}{\kappa \frac{g}{\theta_v} \overline{w'\theta'_v}}, \tag{2.2}$$

where $u_{*\ell}$ indicates local friction velocity and $\overline{w'\theta'_v}$ is the local heat flux. Holtslag and Nieuwstadt (1986) showed that $\Lambda \simeq L$ in that part of the SBL which encompasses a layer between 10 and 50 % of the BL height at neutral stability and is exponentially decreasing with increasing stability (Fig. 2.3). This indicates that the use of $(z - d)/\Lambda$, which is required by local scaling, is almost equivalent to the SL scaling parameter $(z - d)/L$. Therefore, the local scaling approach can be viewed as an extension of MOST for the entire SBL.

For large values of z/Λ ($z/\Lambda \to \infty$), the dependence on z disappears because stable stratification restricts vertical motion thus, causing turbulence vertical scales to be very small. Wyngaard and Coté (1972) named this limit "local z-less stratification" (height-independent). Based on the observations from a tall tower (Cabauw, the Netherlands), Nieuwstadt (1984) found this limit to be for $\zeta_\ell > 1$.

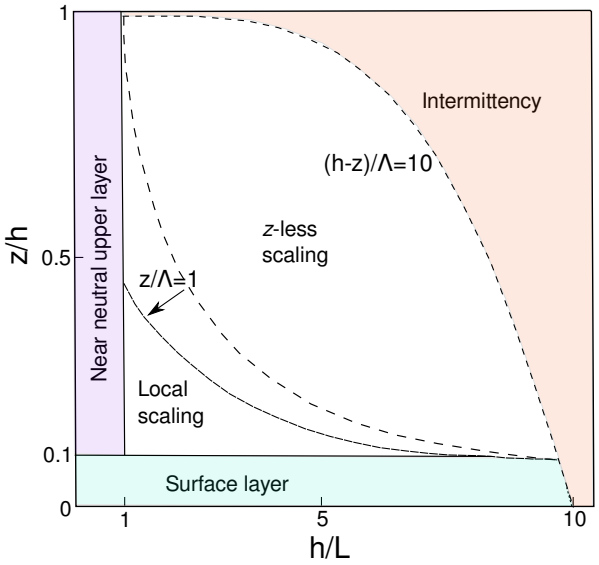

Figure 2.3: Schematic representation of scaling regimes in the NBL (adapted from Holtslag and Nieuwstadt 1986). The mean height of the turbulent ABL is indicated with h, z is the height above the ground, L and Λ represent Obukhov and local Obukhov length scale, respectively.

Evaluation of the second-order moments, especially of wind velocity standard deviations, provides good understanding of turbulence statistics. According to similarity theory, dimensionless quantities should be universal functions of the non-dimensional stability parameter. In the local scaling framework, standard deviations of wind speed components σ_i, where $i = (u, v, w)$ denotes longitudinal, lateral and

vertical velocity components, respectively, are scaled as

$$\phi_i = \frac{\sigma_i}{u_{*\ell}}, \tag{2.3}$$

where ϕ_i represents a set of universal similarity functions, different for each velocity component. In the literature different formulations of the ϕ_i functions can be found. A comprehensive review of various formulations of ϕ_i functions suggested by different studies and for different stabilities is presented by de Franceschi et al. (2009). A generally accepted form of the flux-variance similarity relationships in the SBL is

$$\phi_i(\zeta_\ell) = a_i(1 + b_i\zeta_\ell)^{c_i}, \tag{2.4}$$

where coefficients a_i, b_i and c_i need to be found experimentally. Accordingly, the non-dimensional wind shear defined as

$$\phi_m(\zeta_\ell) = \frac{k(z-d)}{u_{*\ell}}\frac{\partial \overline{u}}{\partial z}, \tag{2.5}$$

where $\overline{u}$ is the mean wind speed, is also a unique function of static stability. For neutral conditions ($\zeta_\ell = 0$), ϕ_m approaches unity. As the exact forms of the similarity functions are not predicted by similarity theory and they should be determined from field experiments, many different formulations have been proposed based on the data from different experiments (e.g. Dyer 1974; Beljaars and Holtslag 1991; Cheng and Brutsaert 2005; Grachev et al. 2007; Sorbjan and Grachev 2010). Thus, the results will first be compared to the linear relationship of Dyer (1974) obtained for the stable SL

$$\phi_m(z/L) = 1 + b_m\frac{z}{L}, \tag{2.6}$$

where $b_m = 5$. Högström (1988) modified several existing formulas for ϕ_m (and also for the non-dimensional temperature profile, ϕ_h), in order to comply with his assumptions of $k = 0.4$ and $(\phi_h)_{\zeta=0} = 0.95$. For Dyer's expression (2.6), he obtained a value $b_m = 4.8$. Additionally, the results are compared to the non-linear stability function of Beljaars and Holtslag (1991)

$$\phi_m(z/L) = 1 + a\frac{z}{L} + b\frac{z}{L}e^{-d\frac{z}{L}} - bd\frac{z}{L}(\frac{z}{L} - \frac{c}{d})e^{-d\frac{z}{L}}, \tag{2.7}$$

where $a = 1$, $b = 0.667$, $c = 5$, $d = 0.35$, as expressions (2.6) and (2.7) are probably the most often used for parameterization in numerical models. Eq. (2.6) was proposed for stabilities $0 < z/L \leq 1$ and it represents flux-profile relationship for the SL. For the explicit form (2.6), data were collected during the summer of 1968 in south-western Kansas, USA above a wheat stubble ($\sim$ 18 cm tall and 2400 m of uniform fetch, e.g. Businger et al. 1971). This relationship has been shown to fit

well the experimental data from different studies in the stability range $0 < z/L \leq 1$. Equation (2.7) was obtained based on the data from a 200-m tall tower in Cabauw (The Netherlands). This site is located in a flat terrain covered mainly with grass with no obstacles for 200 m away from the tower. In this relationship the Obukhov length based on surface values was used. Regarding the range of the stability parameter, this relationship is valid in the strongly stable conditions up to the value of $z/L \approx 7$. This equation is a modification of the relationship given first by Holtslag and de Bruin (1988) and it reduces the overestimation of the non-dimensional gradients for very stable conditions. The strength of this expression over the linear was found to be important for the weather forecast models. When linear relationships for the non-dimensional gradients were used in these models, surface tended to become thermally disconnected from the atmosphere in stable conditions.
Linear equations for ϕ_m (Eq. 2.6) for the stable SL together with the relations for the unstable conditions are traditionally called Businger-Dyer relations (Businger et al. 1971; Dyer 1974). Similar to the non-dimensional velocity variances we use the non-dimensional wind shear in its local form (see Eq. 2.5).

Critical Richardson number

Another widely used stability parameter is the flux Richardson number, defined as the ratio of the buoyancy term to the shear production term in the idealized TKE budget equation:

$$Rf = \frac{-\frac{g}{\bar{\theta}_v}\overline{w'\theta'_v}}{u_*^2 \frac{\partial U}{\partial z}}. \tag{2.8}$$

As already noted, it is a dynamical stability measure, meaning that it takes into account not just the sign of the buoyancy production/destruction term but also the strength of the shear production and it is dimensionless. For stable stratification it is positive and the production of turbulence is larger than damping if $Rf < 1$. For values $Rf > 1$, turbulence can not be maintained even if shear production exists because it is immediately damped by the stratification. For $0 < Rf < 1$ the flow is statically stable and dynamically unstable, meaning that the turbulence can exist. However, the definition of Rf does not take into account the TKE dissipation rate (ε) which contributes to the suppression of turbulence. The "critical" Richardson number above which suppression of TKE is dominating over production can be yield by equating the total suppression (buoyancy and dissipation terms) to total production, i.e. shear production of TKE:

$$\frac{\frac{g}{\bar{\theta}_v}\overline{w'\theta'_v} - \varepsilon}{\overline{u'w'}\frac{\partial \bar{U}}{\partial z}} = 1, \tag{2.9}$$

which gives

$$Rf_{cr} = 1 + \frac{\varepsilon}{\overline{u'w'}\frac{\partial \overline{U}}{\partial z}}. \tag{2.10}$$

Since the second term on the right hand side is always negative, the critical number is reached somewhere between $0 < Rf < 1$. Beyond Rf_{cr} turbulence occurs only sporadically and this state of the SBL is referred to as intermittent.

However, when turbulent fluxes are not available one might use gradient Richardson number Ri, which is based on the arguments of the K-Theory or eddy diffusivity theory. This theory relates turbulent correlations to vertical gradients and this gives the expression for Ri:

$$Ri = \frac{g}{\overline{\theta}_v} \frac{\frac{\partial \overline{\theta_v}}{\partial z}}{\left(\frac{\partial \overline{U}}{\partial z}\right)^2}. \tag{2.11}$$

In literature, a critical Richardson number is usually given in terms of Ri rather than Rf. However, the existence of a threshold beyond which the turbulence is suppressed is one of the fundamental problems of the SBL flows. Richardson (1920) assumed that when Ri exceeds some critical value (Ri_{cr}), turbulence would collapse to laminar flow and he found $Ri_{cr} = 1$. In the past six decades much research was focused on determining the critical Ri and Rf and a short overview is given in Grachev et al. (2013). The transition from turbulent to laminar flow (or from turbulent to non-turbulent flow in the general case) and vice versa still presents an ongoing issue, since controversial findings have been reported (e.g. Grachev et al. 2013, and references therein). While many different studies based on analytical, numerical, laboratory and observational studies suggest that $Rf_{cr} \approx 0.20 - 0.25$, Zilitinkevich et al. (2007) and Zilitinkevich et al. (2010) argued that there is no critical value for Ri.

Based on the observational dataset in the SBL, Grachev et al. (2013) argued that the upper limit for applicability of the local similarity theory is determined by the inequalities $Ri < Ri_{cr}$ and $Rf < Rf_{cr}$. They found both critical values to be equal to $Ri_{cr} = Rf_{cr} = 0.20 - 0.25$, with $Rf_{cr} = 0.20 - 0.25$ being the primary threshold. Since this thesis investigates the applicability of the local scaling approach in the SBL, their threshold values will be used in the analysis.

z-less scaling

The z-less concept requires that z cancels in the Eqs. (2.4) and (2.6). As a result, a linear relationship for the non-dimensional function ϕ_m is obtained, while

non-dimensional functions ϕ_i asymptotically approach constant values:

$$\phi_m(\zeta_\ell) = b_m\zeta_\ell, \tag{2.12}$$

$$\phi_i = b_i, \tag{2.13}$$

where b_m and b_i are experimentally determined coefficients. For convenience, throughout this thesis the notation $\zeta = \zeta_\ell$ will be used as all variables are based on local values.

2.3 Spectral characteristics of turbulence

Since turbulence energy is contained in whirls (or eddies) of different size, we can use spectral analysis to describe the content of turbulence energy related to the eddies of various size, as well as to frequency of fluctuations in measurements. Through the spectral representation the amount of kinetic energy, variance or eddy flux is associated with each scale of motion. Spectra are useful because they show the distribution of energy or variance with respect to frequency. Additionally, estimates in different frequency bands are often statistically independent of each other. The Fast Fourier Transform (FFT) enables estimates of spectral densities for large samples (e.g. Panofsky and Dutton 1984).

In the turbulent part of the atmospheric energy spectrum we can distinguish three major regions: the energy-containing range, the inertial subrange and the dissipation range (e.g. Kaimal and Finnigan 1994). In the energy-containing range TKE is produced by the mean flow and buoyancy (energy contained in large eddies). It is characterized by the Eulerian integral length scale λ. When the turbulence spectrum is plotted against the wavenumber (Fig. 2.4), maximum energy occurs at this scale $\lambda \sim 1/\kappa$, where κ is the length of the wave number vector $\vec{\kappa}$. The energy-containing range is usually followed by the inertial subrange which was theoretically derived by Kolmogorov (1941) who used dimensional analysis for that. For sufficiently high Reynolds numbers he assumed that the flow is locally homogeneous and almost isotropic in this range. Isotropic turbulence does not depend on the original geometry (e.g. Panofsky and Dutton 1984). Production and destruction of energy is negligible in this region. In a simplified concept for this range, turbulent eddies are consecutively split up into smaller eddies until the smallest ones release their energy in dissipation. Thus, in this range of the spectrum, turbulence should uniquely be determined by the TKE dissipation rate ε and viscosity ν. A characteristic length scale η for the viscous eddies can then be defined by means of dimensional analysis:

$$\eta = \left(\frac{\nu^3}{\varepsilon}\right)^{1/4}, \tag{2.14}$$

where η represents the Kolmogorov microscale at which turbulence dissipates into heat due to the viscosity. This defines the dissipation range.

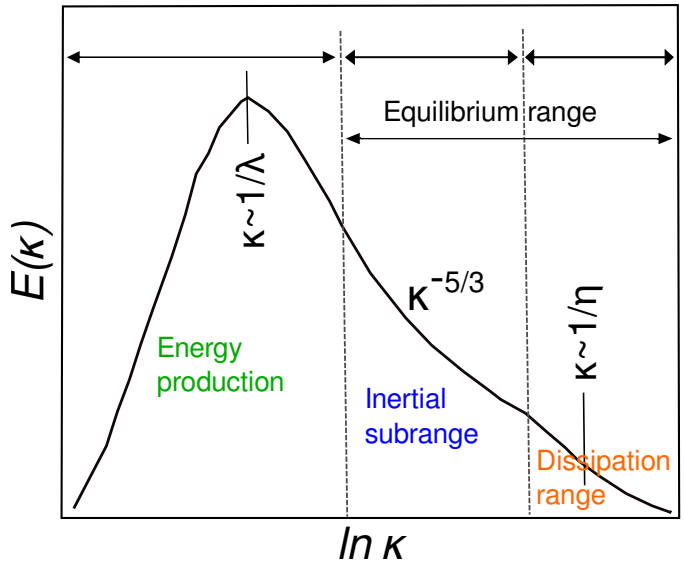

Figure 2.4: Schematic representation of the turbulence spectrum $E(\kappa)$ dependent on the wave number κ. Ranges of energy production, inertial subrange and dissipation range are indicated. λ represents Eulerian integral length scale and η is Kolmogorov microscale. (Adapted from Kaimal and Finnigan (1994).)

Turbulence extracts energy from the mean flow at the low wave number range, $\kappa \approx \lambda^{-1}$. Turbulent eddies exhibit the cascade of the TKE from the energy-containing range down to higher wave numbers. This process of energy cascade is regulated by the dissipation rate ε. The higher this rate is, the faster the energy is transported. This rate of energy supply/dissipation, per unit mass of fluid is:

$$\varepsilon = \begin{cases} \text{energy supplied to fluid per unit mass and time} \\ \text{energy cascading from scale to scale, per unit mass and time} \\ \text{energy dissipated by viscosity, per unit mass and time} \end{cases}$$

The dimensions[1] of ε are:

$$\varepsilon = \frac{ML^2T^{-2}}{MT} = L^2T^{-3}. \tag{2.15}$$

The range of length scales much smaller than λ is called the *equilibrium range*. In this range the spectrum is nearly isotropic and generally in equilibrium. Therefore, the energy will depend on the parameters that determine the nature of the small-scale flow, that is

$$E = E(\kappa, \varepsilon, \nu), \qquad \kappa \gg \lambda^{-1}. \tag{2.16}$$

[1] L represents length scale in meters, T a time in seconds and M is mass in kg.

The inertial subrange is that part of the equilibrium range which is not affected directly by viscosity and we can write:

$$E = E(\kappa, \varepsilon), \qquad \eta^{-1} \gg \kappa \gg \lambda^{-1}. \tag{2.17}$$

Based on the dimensional analysis Kolmogorov derived the shape of three-dimensional velocity spectrum (i.e. TKE spectrum) in the inertial subrange

$$E(\kappa) = \alpha_K \varepsilon^{2/3} \kappa^{-5/3}, \tag{2.18}$$

where α_K represents a universal (Kolmogorov) number within the isotropic inertial subrange ranging between 1.53 and 1.68 (e.g. Stull 1988). According to this, the spectra exhibit $-5/3$ slope in the inertial subrange and, thus, Eq. (2.18) is called *Kolmogorov's* $\kappa^{-5/3}$ *law*. While the production of energy at larger scales is an anisotropic process, turbulence in the inertial subrange is locally isotropic. The concept of locally isotropic turbulence was first introduced by Kolmogorov (1941) and his theory relies on the assumption of gradual lost of anisotropy as energy is transferred to smaller scales. Under the assumption of local isotropy, Kolmogorov proposed the existence of a range of scales, i.e. inertial subrange, in which ε controls the dynamics of turbulence. This is also known as Kolmogorov's similarity hypothesis. Under the local isotropy hypothesis the longitudinal velocity spectrum $F_{1,1}(\kappa_1)$, lateral $F_{2,2}(\kappa_1)$ and vertical velocity spectrum $F_{3,3}(\kappa_1)$ are derived from Eq. (2.18):

$$F_{1,1}(\kappa_1) = \frac{18}{55} \alpha_K \varepsilon^{2/3} \kappa_1^{-5/3}, \tag{2.19}$$

$$F_{2,2}(\kappa_1) = F_{3,3}(\kappa_1) = \frac{24}{55} \alpha_K \varepsilon^{2/3} \kappa_1^{-5/3}, \tag{2.20}$$

where κ_1 represents the one-dimensional wave number. Therefore, in the inertial subrange spectral densities of lateral and vertical velocity components are approximately equal, while that of the longitudinal velocity spectrum is smaller by 1/3:

$$F_{2,2}(\kappa_1) = F_{3,3}(\kappa_1) = \frac{4}{3} F_{1,1}(\kappa_1). \tag{2.21}$$

Consequently, the spectra for v and w will be placed higher than the u spectrum in the inertial subrange, and in the log-log representation all three spectra should fall of as $\kappa_1^{-5/3}$. An additional consequence of local isotropy is that all correlations between velocity components and between velocity components and scalars vanish and therefore no turbulent fluxes in the inertial subrange. Thus, the test for the existence of the inertial subrange comprises three steps (e.g. Kaimal and Finnigan 1994):

1. $-5/3$ power law,
2. $4/3$ ratio between transverse and longitudinal velocity spectra,
3. vanishing (or very small) cospectral levels .

2.3.1 Dissipation rate of the turbulent kinetic energy

The dissipation rate of the TKE can be determined based on the Eq. (2.19):

$$\varepsilon = \left[\frac{\kappa_1^{5/3} F_{i,i}(\kappa_1)}{\alpha_i}\right]^{3/2}, \tag{2.22}$$

where α_i $(i = u, v, w)$ represents Kolmogorov constant for each velocity component corresponding to $\alpha_u = (18/55)\alpha_K$ and $\alpha_{v,w} = (24/55)\alpha_K = 4/3\alpha_u$. For measurements performed in frequency space, we invoke Taylor's hypothesis to transform from wavenumber space to frequency scales: $\kappa_1 = 2\pi f/\overline{u}$, where f is natural frequency and $\overline{u}$ is the mean wind speed. The relationship between power spectra in wavenumber and frequency space is found based on the consideration of a logarithmic spectrum, that is, wavenumber-weighted spectrum, which represents the variance:

$$\int_0^\infty F_{i,i}(\kappa_1)d\kappa_1 = \sigma_u^2 = \int_0^\infty S_{i,i}(f)df. \tag{2.23}$$

It follows:

$$\kappa_1 F_{i,i}(\kappa_1) = f S_{i,i}(f). \tag{2.24}$$

Based on Eqs. (2.22) and (2.24) we can determine the dissipation rate ε for measurements done in frequency space:

$$\varepsilon = \frac{2\pi}{\overline{u}}\left[\frac{f^{5/3} S_{i,i}(f)}{\alpha_i}\right]^{3/2}. \tag{2.25}$$

2.3.2 Surface layer spectral scaling

The concept of scaling provides more insight into the multi-length structure of the flow when it is applied to spectra (Antonia and Raupach 1993). Since eddies of different size contribute to spectra, the spectra are assumed to scale with those scaling parameters at the origin of the eddies (Olesen et al. 1984). For example, under statically unstable conditions, spectra are influenced by both small scale eddies originating in the layer close to the ground (i.e. surface layer) and by large-scale eddies having their origin above the SL (Kaimal et al. 1976). In the SBL, close to the ground 3-dimensional eddies are damped by the buoyancy effects and the vicinity of the ground, therefore turbulent spectra are mostly determined by SL

scaling parameters.

First expressions for the SL velocity spectra were proposed by Kaimal et al. (1972). These models were based on the experimental data from the Kansas (1968) experiment and are considered as a classical reference today. Kaimal et al. (1972) used SL spectral scaling arguments to estimate the form of the turbulence spectra $S_u(f)$, $S_v(f)$ and $S_w(f)$ as functions of the stability parameter z/L.

In the framework of SL similarity scaling, friction velocity u_* is used to non-dimensionalize the velocity spectra in the SL. From Eqs. (2.19) and (2.24) the inertial subrange logarithmic u spectrum normalized with u_*^2 has the form

$$\frac{fS_u(f)}{u_*^2} = \frac{\alpha_u}{(2\pi k)^{2/3}} \left(\frac{kz\varepsilon}{u_*^3}\right)^{2/3} \left(\frac{fz}{\overline{u}}\right)^{-2/3}, \tag{2.26}$$

where α_u is a universal Kolmogorov constant for longitudinal wind component estimated from different experiments to be about 0.5 and k is von Kármán constant. The non-dimensional dissipation rate of TKE ϕ_ε is equal to

$$\phi_\varepsilon = \frac{kz\varepsilon}{u_*^3}, \tag{2.27}$$

and the non-dimensional frequency is equal to $n = fz/\overline{u}$. Thus, the form of longitudinal wind component spectra in the inertial subrange is expressed as:

$$\frac{fS_u(f)}{u_*^2} = \frac{\alpha_u}{(2\pi k)^{2/3}} \phi_\varepsilon^{2/3} n^{-2/3} = a_u \phi_\varepsilon^{2/3} n^{-2/3}, \tag{2.28}$$

where $a_u = \alpha_u/(2\pi k)^{2/3}$. Analog forms are valid for lateral and vertical velocity spectra. According to Högström (1990) the Kolmogorov constant for the longitudinal wind component α_u ranges from 0.36 to 0.56. As a consequence of local isotropy, values of α_v and α_w should be equal to $4/3\alpha_u$. ϕ_ε is a universal function of the stability parameter ζ. Both α_i and ϕ_ε must be determined empirically from spectral measurements. Using the value of $k = 0.35$ obtained from Kansas data and $\alpha_u = 0.5$, Kaimal et al. (1972) estimated the constants $a_i = \alpha_i/(2\pi k)^{2/3}$ to be $a_u = 0.3$ and $a_v = a_w = 0.4$. These estimates were obtained with 10% accuracy and no clear dependency on stability.

Kaimal et al. (1972) included $\phi_\varepsilon^{2/3}$ into the normalization of the velocity spectra. In this way the dependence on the stability parameter is removed and consequently all spectra in the inertial subrange collapse to a single straight line with a $-2/3$ slope (when plotted on a log-log scale). Additionally, based on the Kansas hot-wire measurements of ε, Wyngaard et al. (1971) gave the following interpolation formula for ϕ_ε for the SBL:

$$\phi_\varepsilon^{2/3} = 1 + 2.5|z/L|^{3/5}, \qquad 0 \le z/L \le 2. \tag{2.29}$$

In many other studies assuming local equilibrium conditions, ϕ_ε was found to have a liner dependence on ζ:

$$\phi_\varepsilon^{2/3}(\zeta) = (1 + b_\epsilon \zeta)^{2/3}, \qquad \zeta > 0. \tag{2.30}$$

The empirically determined parameter b_ϵ is estimated as $b_\epsilon = 3.7$ (Garratt 1972), $b_\epsilon = 4.0$ (Wyngaard 1975) and $b_\epsilon = 5.0$ (Kaimal and Finnigan 1994) .

2.3.3 Models of velocity spectra

Kaimal et al. (1972) derived the relationships which uniquely defined the behavior of the spectra in the inertial subrange for neutral stabilities. Considerable similarity in the shape of spectra was observed, with the fall off according to $-2/3$ on the high frequency side. Therefore, the empirical formulae have a corresponding form. They presented formulae which fitted best their neutral ($z/L = 0$, $\phi_\varepsilon(z/L = 0) = 1$) velocity spectra:

$$\frac{fS_u(f)}{u_*^2} = \frac{105n}{(1 + 33n)^{5/3}}, \tag{2.31}$$

$$\frac{fS_v(f)}{u_*^2} = \frac{17n}{(1 + 9.5n)^{5/3}}, \tag{2.32}$$

$$\frac{fS_w(f)}{u_*^2} = \frac{2n}{1 + 5.3n^{5/3}}. \tag{2.33}$$

Therefore, mathematical expressions (2.31) to (2.33) are used to model the observed turbulence spectra, which enables a comparison with other atmospheric and laboratory data. These expressions have one of the two following forms:

$$\frac{fS(f)}{u_*^2} = \frac{An}{(1 + Bn)^{5/3}}, \tag{2.34}$$

$$\frac{fS(f)}{u_*^2} = \frac{An}{1 + Bn^{5/3}}. \tag{2.35}$$

These two models can be written in a more general form

$$\frac{fS(f)}{u_*^2} = \frac{An^\gamma}{(1 + Bn^\alpha)^\beta}, \tag{2.36}$$

where $A, B, \alpha, \beta, \gamma$ are constants which depend on atmospheric stability. γ represents a low-frequency slope on a log-log plot, which is very near $+1.0$. In the high-frequency range, the spectra are characterized by the slope $\gamma - \alpha\beta$. The spectra given by Eq. (2.34) are broader than those given by Eq. (2.35), thus this model is

called "the blunt model", while the spectra expressed by Eq. (2.35) are called "the pointed model". The position of the spectrum is determined with constants A and B.

Analytical models given by Eq. (2.36) are used by many authors to describe spectra obtained during different experiments and different atmospheric stabilities. In the above mentioned spectral models for stable stratification, the spectral intensity peak is reduced and shifted to higher frequencies as stability increases. The spectral maximum represents typical scales of the turbulence. That is, the wavelength at the spectral peak λ_m represents the size of eddies with the most energy:

$$\lambda_m = z/n_m, \tag{2.37}$$

where n_m is the frequency of the spectral maximum. Kaimal et al. (1972) found the following approximations for the locations of the spectral maximum (peak) in statically stable conditions:

$$(n_m)_w \simeq 5(n_m)_u \simeq 2(n_m)_v. \tag{2.38}$$

According to Kaimal and Finnigan (1994) the behavior of $(\lambda_m)_w$ in the stable SL and the layer immediately above can be expresses as follows:

$$(\lambda_m)_w = \begin{cases} z(0.55 + z/L)^{-1}, & 0 \leq z/L \leq 1 \\ zL(0.45z + 1.1L)^{-1}, & 1 \leq z/L \leq 2 \\ L, & z/L \geq 2. \end{cases} \tag{2.39}$$

Olesen et al. (1984) have constructed spectral models of the velocity spectra for the SBL. Using their models, spectra can be normalized so that they all coincide to one curve only, irrespective of static stability. Graphically, this means that all observed spectra are transported along the frequency axis until the positions of their maxima coincide, and along the $fS(f)/u_*^2$-axis until their high-frequency asymptotes coincide. Mathematically, the stable spectra are normalized to adhere to one curve by defining the factor q, which is a function of stability:

$$q = \frac{n_m}{(n_m)_{neutral}}. \tag{2.40}$$

Olesen et al. (1984) assumed n_m to be proportional to the dimensionless velocity gradient ϕ_m, thus, q is identical to ϕ_m. Based on the Kansas data, they set up a spectral model for wind velocities in statically stable conditions at low heights:

$$\frac{fS_u(f)}{u_*^2} = \frac{79n/\phi_m}{1+263\,(n/\phi_m)^{5/3}}\left(\frac{\phi_\varepsilon}{\phi_m}\right)^{2/3}, \tag{2.41}$$

$$\frac{fS_v(f)}{u_*^2} = \frac{13n/\phi_m}{1+32\,(n/\phi_m)^{5/3}}\left(\frac{\phi_\varepsilon}{\phi_m}\right)^{2/3}, \tag{2.42}$$

$$\frac{fS_w(f)}{u_*^2} = \frac{3.5n/\phi_m}{1+8.6\,(n/\phi_m)^{5/3}}\left(\frac{\phi_\varepsilon}{\phi_m}\right)^{2/3}. \tag{2.43}$$

2.4 Budget of TKE

The TKE is an important variable for BL flows, as it indicates turbulence intensity. In order to get insight into the nature of turbulent production and destruction in the BL it is useful to examine the terms in the TKE equation. If we choose a coordinate system[2] aligned with the mean wind and neglect subsidence, a simplified form of the TKE budget equation is (e.g. Stull 1988; Kaimal and Finnigan 1994):

$$\underbrace{\frac{\partial \overline{e}}{\partial t}}_{\text{(I)}} = \underbrace{-\overline{u}\frac{\partial \overline{e}}{\partial x}}_{\text{(II)}} \underbrace{-\overline{u'w'}\frac{\partial \overline{u}}{\partial z}}_{\text{(III)}} + \underbrace{\frac{g}{\overline{\theta}_v}\overline{w'\theta'_v}}_{\text{(IV)}} \underbrace{-\frac{1}{\overline{\rho}}\frac{\partial \overline{w'p'}}{\partial z}}_{\text{(V)}} \underbrace{-\frac{\partial \overline{w'e}}{\partial z}}_{\text{(VI)}} \underbrace{-\varepsilon}_{\text{(VII)}}, \tag{2.44}$$

where $\overline{e} = \frac{1}{2}(\overline{u'^2}+\overline{v'^2}+\overline{w'^2})$ is TKE/m and p is the atmospheric pressure. Components of Eq. (2.44) represent physical processes which act as sources or sinks of turbulence. Term (I) represents local storage of TKE, (II) is the mean advection term, term (III) represents the shear production, which is almost always positive. The buoyant term (IV) represents a loss term in the SBL since the heat flux is negative, so we note this term as buoyancy destruction. The fifth term is the pressure transport term, which describes how TKE is redistributed by vertical pressure perturbations. It is difficult to measure, so it is often obtained indirectly as a residual after measurement of all other terms. This term is often associated with buoyant motions or gravity waves. Term (VI) represents turbulent transport of TKE. It represents the rate at which TKE is moved around by velocity fluctuations. The last term represents the viscous dissipation of TKE, that is the conversion of TKE into internal energy.

According to the MOST framework, the normalized TKE budget is obtained by multiplying all terms on the right side of Eq. (2.44) by $k(z-d)/u_{*\ell}^3$, and for a stationary flow is equal to

$$0 = -\phi_a + \phi_m - \zeta - \phi_p - \phi_t - \phi_\varepsilon, \tag{2.45}$$

[2] In this coordinate system downward heat flux is negative.

where ϕ_a represents dimensionless advection, ϕ_m is shear production, $\zeta = (z-d)/\Lambda$ is buoyant destruction, ϕ_t is turbulent transport, ϕ_p is pressure transport and ϕ_ε is dimensionless turbulent dissipation. Under the assumption of horizontal homogeneity ϕ_a becomes zero. If the sum of turbulent and pressure transport terms were negligible (which is a common assumption, e.g. Wyngaard (2010)), then there should be a local equilibrium, i.e. TKE produced by local shear is destroyed locally by buoyancy and dissipation over all stabilities

$$\phi_\varepsilon \approx \phi_m - (z-d)/\Lambda. \tag{2.46}$$

This relationship suggests the general form of ϕ_ε to the better known ϕ_m (Fortuniak and Pawlak 2015). Wyngaard and Coté (1971) suggested local balance under statically neutral conditions ($(z-d)/\Lambda = 0$) with $\phi_m = \phi_\varepsilon = 1$ and $\phi_t + \phi_p = 0$. However, in recent decades this assumption was challenged by many experimental studies which presented evidence of local imbalance (e.g. Högström 1990; Frenzen and Vogel 2001; Li et al. 2008; Duarte et al. 2015). The observed imbalance, showing excess or inadequate TKE dissipation under neutral conditions, underlines the importance of the transport (and possibly advection) terms to either gain or loss of TKE, respectively.

The turbulent transport term can be calculated directly from the observations. Wyngaard and Coté (1971) suggested that non-dimensional turbulent transport term is small in the stable BL but were not able to find the correlation to the stability parameter, while Högström (1996) found it to be constant in neutral and weakly stable conditions. Li et al. (2008) extended the traditional parameterization for ϕ_t used for the unstable conditions

$$\phi_t = a + b(z-d)/\Lambda \tag{2.47}$$

to the stable conditions as well.

The remaining two terms, the pressure transport and advection terms, are usually considered as a residual term, due to many difficulties involving their measurements. Spatial measurements of TKE in streamwise direction, needed to calculate the advection term directly, are not easily performed with tower-based measurements. Also, for calculation of the pressure transport term accurate measurements of small pressure fluctuations are needed, but these are extremely difficult to measure with current sensor technology available. Despite this, direct measurements of the pressure transport term were reported in the literature, e.g., McBean and Elliot (1975); Cuxart et al. (2002), but these are known to contain much uncertainty.

Chapter 3

Data and Methods

3.1 Experimental set-up and site description

A 62 m high tower was located in the vicinity of the small industrial town Kutina, Croatia (tower coordinates: 45^{o}28'32"N, 16^{o}47'44"E). The tower was placed above a grassy surface and it was surrounded by approximately 18 m high black walnut (*Juglans nigra*) trees. The closest trees are approximately $20-25$ m away from the tower and they encompass an area of approximately 120×480 m^2 (Fig. 3.1). The tower is situated in a rather heterogeneous surrounding regarding both a larger spatial scale (Fig. 3.1(a)) and immediate vicinity of the measurement site (on the order of ~ 1 km distance, Fig. 3.1(b)). To the east of the tower, crop fields which extend to the aerial distance of > 1 km are found. South-southeast of the tower, about 800 m to 1.5 km distant a large petrochemical industry plant is placed. In a sector that encounters winds from the north-northwest to the northwest, low, forested hills are located. They are covered with a dense forest, while at lower elevations, cultivated orchards and vineyards are found. Foots of these hills are roughly 1.3 km away from the measurement site. Thus, due to different surface roughness features measurements in the SBL at the measuring site may be contaminated by local advective fluxes, drainage flows and/or orographically-generated gravity waves. These features are related to (sub)mesoscale motions which do not obey similarity scaling and are therefore removed from our data by the rigorous data quality control and post-processing options as described later in the thesis (Section 3.2). Thus, the focus of this thesis is on the micrometeorologically complex local site characteristics, which may be more typical for "real sites" than the usually investigated homogeneous reference sites.

Data used in this thesis were collected during wintertime (1 December 2008 – 28 February 2009) and correspond to the nocturnal period from 1800 to 0600 local time. Turbulence measurements of three-dimensional wind and sonic temperature

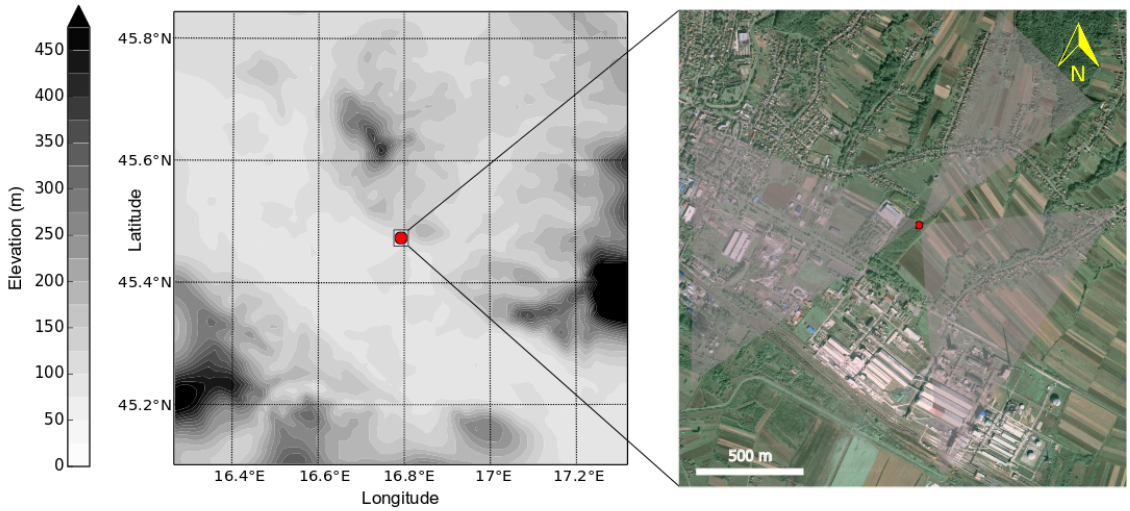

Figure 3.1: **(a)** Topographic map with contour lines each 25 m of the area surrounding the measurement site (red dot) representing inhomogeneous terrain on a larger spatial scale. **(b)** Google Maps image (Image©2015 DigitalGlobe) of the observational site. Measurement tower is indicated with a red dot ($45^o28'32''$ N, $16^o47'44''$ E).

were continuously measured using identical WindMaster Pro (Gill Instruments) ultrasonic anemometers that sampled at 20 Hz. Data were measured at five levels above the canopy height, hereafter at level 1 ($z_1 = 20$ m above the surface), level 2 ($z_2 = 32$ m), level 3 ($z_3 = 40$ m), level 4 ($z_4 = 55$ m) and level 5 ($z_5 = 62$ m). Measurement levels were prescribed prior to the experiment through existing tower

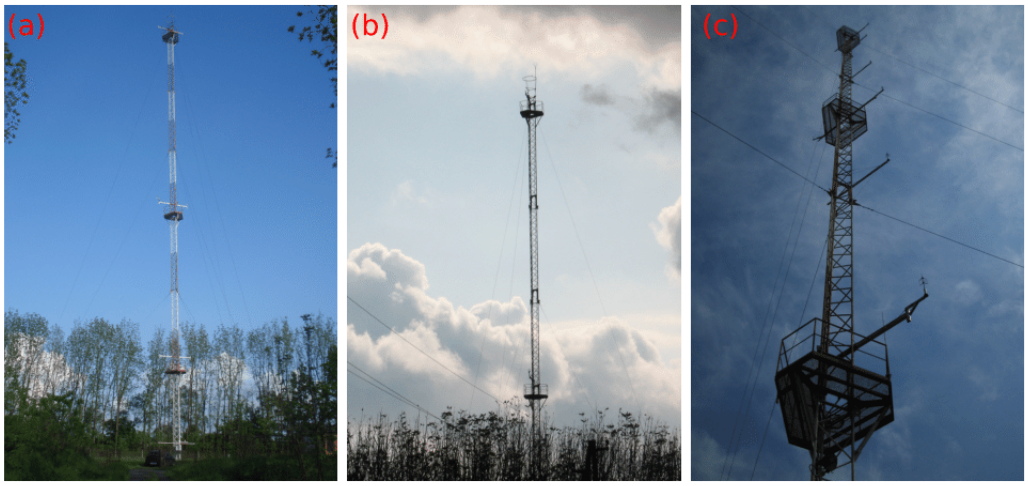

Figure 3.2: Measurement tower.

infrastructure (Fig. 3.2). Given the complicated and spatially inhomogeneous characteristics of the measurement site, an idealized vertical structure is considered as a zero-order approach in the analysis. An estimate of vertical layers for statically neutral conditions was done using different models available in the literature and

serves as a simple model for the interpretation of the results. For stably stratified conditions these estimates will not be fully appropriate, but will provide the gross picture.

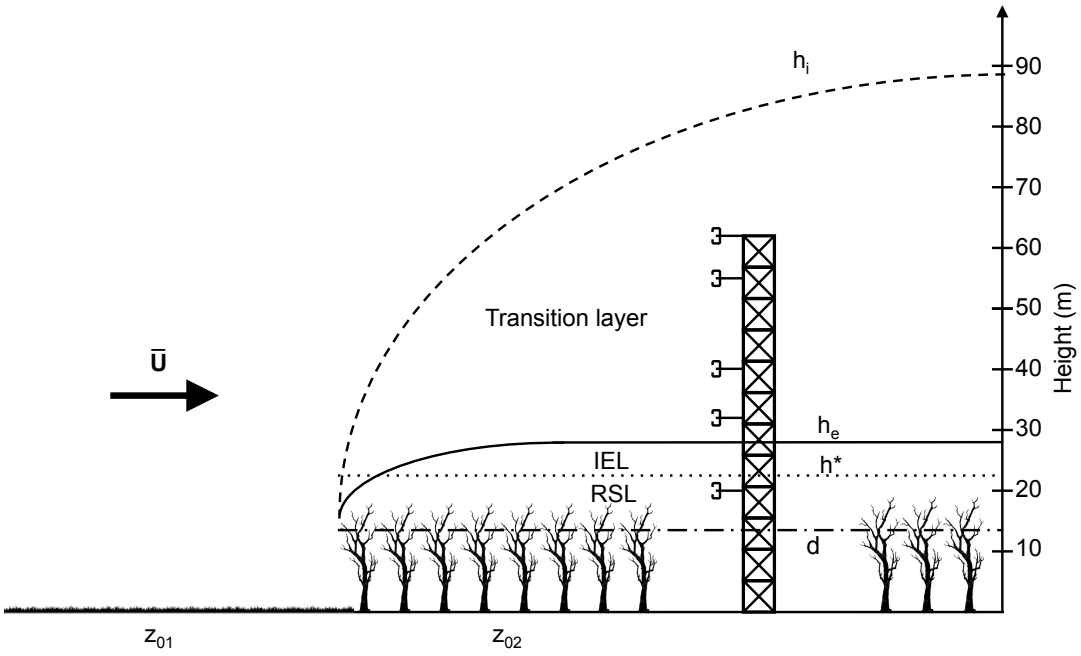

Figure 3.3: Conceptual sketch of idealized vertical layers after a step change in surface roughness for the long fetch case ($\sim$ 400 m) under neutral conditions. The depth of the IBL (h_i), which develops due to the change in roughness conditions, is estimated based on the model of Cheng and Castro (2002). Above the $h_i + d$ the flow is in equilibrium with the upwind surface. Within the internal equilibrium layer (IEL) the flow is in equilibrium with the forest. The transition layer indicates the transition zone between upwind and downwind equilibrium conditions. The dotted line denotes the height of the RSL, h^*, estimated based on the relation given by Raupach (1994). The dash-dot line shows the zero-plane displacement height (d) estimated as $3/4h_c$ (e.g. Stull 1988; Kaimal and Finnigan 1994). z_{01} and z_{02} correspond to upwind and downwind roughness lengths, respectively. The black arrow denotes the mean wind ($\overline{U}$) direction.

Conceptually, when the air flows over changing terrain, the downwind surface conditions are likely to influence the measurements via internal boundary layers (IBLs), which grow in height (h_i) with downwind distance (Fig. 3.3) (e.g. Cheng and Castro 2002; Dellwik and Jensen 2005). Only the lowest portion of the IBL ($\sim$ 10 % of h_i) is in equilibrium with the new surface (internal equilibrium layer, IEL) while the flow above the IBL is in equilibrium with the upstream surface conditions. The IEL can, finally, be identified with the inertial sublayer (IS). However, if the new surface is very rough, its lower part must be considered as a RSL. Within the upper part of the IEL, i.e. the IS, turbulent fluxes are approximately constant with height, MOST is valid and the mean wind speed follows the expected logarithmic profile. Within the RSL, the flow is influenced by the distribution and structure of canopy elements (Monteith and Unsworth 1990; Rotach and Calanca 2014), with

momentum and scalars transported by turbulence, wake effects and very weakly by molecular diffusion (Malhi 1996). Above the height of the IEL (h_e) stress and fluxes start to decrease due to the upwind influence. This layer is defined as a transition layer (Fig. 3.3). Due to the very tall roughness elements we use the zero-plane displacement height (d) as our reference - hence the IBL is assumed to range from $z = d$ up to $z = h_i + d$. Ideally, after a long enough flow over the new surface, the IBL fills the entire boundary layer. Since we are interested in evaluating the degree to which local scaling applies under inhomogeneous fetch conditions, we map the idealized SBL structure to the IBL. The transition layer then becomes the outer part of the inhomogeneously forced SBL.

We have estimated the length scales introduced above as follows: h_i is estimated based on the model of Cheng and Castro (2002)

$$\frac{h_i}{z_{02}} = 10.56(\frac{x}{z_{02}})^{0.33}, \tag{3.1}$$

where x is the distance to the roughness change from the position of measurement (fetch) and z_{02} is the roughness length of the new surface. Following Cheng and Castro (2002), h_e can be determined as

$$\frac{h_e}{z_{02}} = 1.47(\frac{x}{z_{02}})^{0.37}. \tag{3.2}$$

The depth of the RSL (h^*) depends on different properties, such as canopy density, roughness length for momentum and tree height. Raupach (1994) estimated the height of the RSL as

$$\frac{h^* - d}{h_c - d} = 2. \tag{3.3}$$

For the zero-plane displacement we use a straightforward methodology, $d = 3/4h_c$ (e.g. Stull 1988; Kaimal and Finnigan 1994), where $h_c = 18$ m is the average canopy height, which is estimated through direct measurements. Additionally, for the walnut forest we used $z_{02} \approx 1$ m (the lower value for the roughness length over forest, $z_0 = 1$ m, according to Foken (2008), his Table 3.1).

The estimated height of the IBL at our site (Tab. 3.1) varied between ~ 40 and 80 m for short (≈ 55 m) and long (≈ 400 m) fetch conditions, respectively. Estimated values of h_e at the location of the tower ranged between 7 and 14 m according to Cheng and Castro (2002) for short and long fetch cases, respectively. These estimates indicate that the second measurement level is above the IEL height ($z = d + h_e$) for all wind directions. Also, the height of the RSL at our measurement site is $h^* = 1.25h_c$, that is, approximately 23 m. Using the above estimates, we find that level 1 is situated within the RSL for all wind directions. For cases characterized

Table 3.1: Height of the equilibrium layer (h_e) and of the internal boundary layer (h_i) estimated based on the model of the Cheng and Castro (2002) (Eqs. 3.1 and 3.2) for different fetch (x) values corresponding to particular wind directions (WD). Note that these heights indicate the height above the displacement height d. In the determination of the fetch length, holes in the forest or corridors of vegetation other than forest were disregarded if their size was small enough.

WD (^{o})	30	60	90	120	150	180	210	240	270	300	330	360
x (m)	92	89	69	56	58	77	391	415	110	84	78	105
h_e (m)	7.8	7.7	7.0	6.5	6.6	7.3	13.4	13.7	8.3	7.6	7.4	8.2
h_i (m)	47	46	43	40	40	44	76	77	50	46	44	49

with the short fetch, the IEL will most likely be within the RSL ($h_e + d < h^*$), while only for wind direction with large fetch conditions (200–250^o) the growing IEL will encompass the RSL and a thin IS will form. Levels 2 and 3 are in the transition layer for all wind directions, while levels 4 and 5 are even above h_i for the short fetches (105–175^o). The highest measurement level reflects the upwind surface conditions for fetches shorter than 100 m. Hence, a potential RSL influence should be detectable if level 1 behaves differently. If levels $2-5$ do not show different behavior, this can be taken as an indication that our crude mapping assumption has some validity.

3.2 Post-processing of the data

3.2.1 Treatment of the raw data

Instruments were mounted 3 m away from the triangular lattice tower (booms facing to the northeast) to minimize any flow distortion effect by the tower. Considerable loss of data was incurred due to intermittent winter icing or temporary instrument malfunction (Table 3.2). During this period, light nocturnal winds were common at the site at the lowest measurement level (Fig. 3.4). We assume that the sonic temperature $T_s = T(1 + 0.51q)$, where T is the air temperature, is close to the virtual potential temperature θ_v and q is the specific humidity. Automated quality control procedures were not used since they may be too strict for the SBL analysis of weak turbulence. Raw 20-Hz data were first divided into 30-min intervals. These intervals were checked for large data gaps, and all 30-min intervals with more than 1% of missing data were omitted from further analyses. After the consistency limits check, i.e. the data having unrealistically high/low values were removed, spikes (defined as data points within the time series which deviate more than four standard deviations from the median value of the particular 30-min averaging window) were also removed. If the number of spikes within the 30-min interval was less than 1% of the total data, spikes were replaced by linear interpolation from neighboring val-

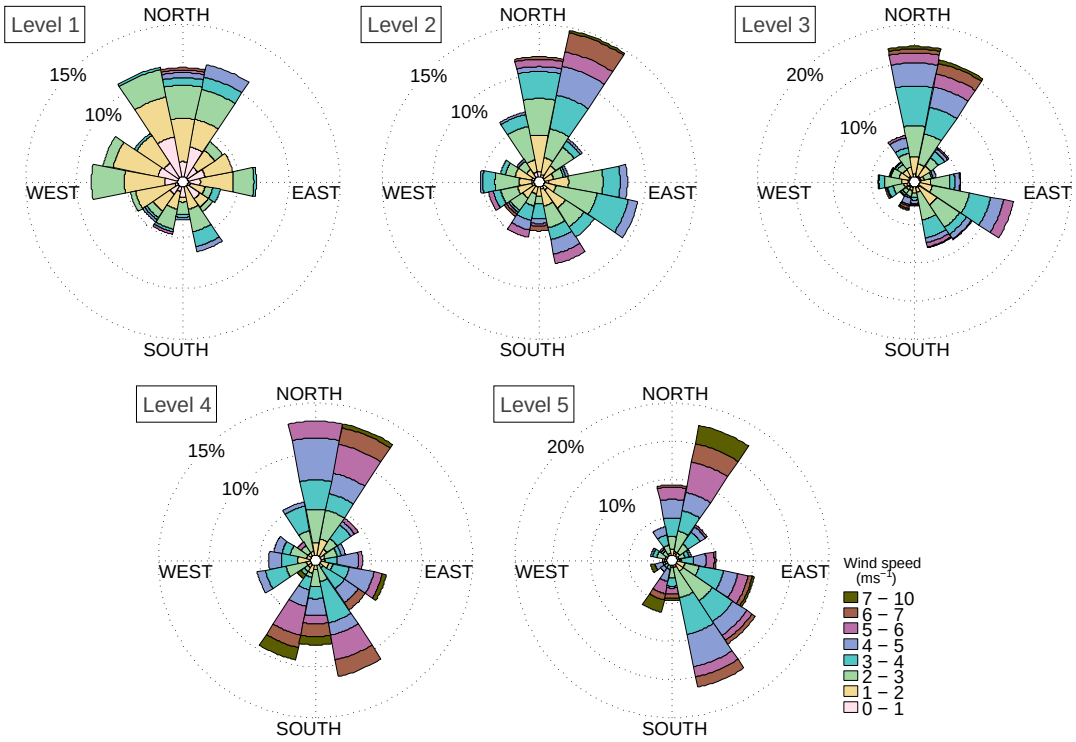

Figure 3.4: Wind roses at the measurement site for 30-min averaged data for the analyzed period (December 2008 - February 2009). Levels 1 to 5 correspond to measurement heights of 20, 32, 40, 55 and 62 m above the ground, respectively.

ues. The angles of attack were calculated for each measurement and for each flux averaging period, and flagged it if angles of attack exceeded 15^o. The number of 30-min intervals available for the further post-processing is labeled as "minimum QC" (Table 3.2). A cross-correlation correction of the time series is already implemented in the Gill Instruments software.

3.2.2 Coordinate rotation

Although double rotation of the data is the most commonly used to correct for sonic misalignment, according to Mahrt (2011) and Mahrt et al. (2013) it should not be applied to SBL data under weak-wind conditions. In the very SBL direction-dependent mean vertical motions may occur where minor surface obstacles can significantly perturb the flow. In a setup like ours, characterized by tall vegetation and/or complex terrain, a non zero 30-min mean vertical wind component may exist. In such situations, a planar fit (PF) method (Wilczak et al. 2001) would be better since it is based on an assumption that the vertical wind component is equal to zero only over longer averaging periods. The mean streamline plane is defined based on the measurements made during the 88-night period for each of five levels (Table 3.2). This period is long enough to encompass

all wind directions and has a sample size that will allow robust averaging. The PF method performs a multiple linear regression on the 30-min wind components to obtain the mean streamline plane (Aubinet et al. 2012):

$$\overline{w}_0 = b_0 + b_1\overline{u}_0 + b_2\overline{v}_0, \tag{3.4}$$

from which the regression coefficients b_0, b_1 and b_2 are deduced, where u_0, v_0 and w_0 indicate measured, unrotated 30-min wind components. Coefficient b_0 indicates the instrumental offset in the vertical wind component and must be subtracted from w_0 from further calculations. The coordinate rotations are performed around the z-axis, the new x-axis and the new y-axis resulting in the yaw α_{PF}, pitch β_{PF} and roll γ_{PF} angles. Since the rotations are not commutative and the regression coefficients are computed from the components in the sonic anemometer coordinate system, the pitch and roll rotations must be applied before the yaw rotation. All the rotations are applied to each individual flux-averaging period. According to Wilczak et al. (2001) these angles can be obtained as

$$\sin\beta_{PF} = \frac{-b_1}{\sqrt{b_1^2+b_2^2+1}}, \quad \cos\beta_{PF} = \frac{\sqrt{b_2^2+1}}{\sqrt{b_1^2+b_2^2+1}}, \tag{3.5}$$

$$\sin\gamma_{PF} = \frac{b_2}{\sqrt{1+b_2^2}}, \quad \cos\gamma_{PF} = \frac{1}{\sqrt{1+b_2^2}}, \tag{3.6}$$

$$\alpha_{PF} = \tan^{-1}\left(\frac{\overline{v_2}}{\overline{u_2}}\right). \tag{3.7}$$

3.3 Determining turbulence averaging time scale

Basu et al. (2006) have shown that using an averaging window of inappropriate length can lead to false conclusions concerning the behavior of the turbulence. In stable flows, use of an averaging time that is too large leads to serious contamination of the computed flux by incidentally captured mesoscale motions (Howell and Sun 1999; Vickers and Mahrt 2003). Here we distinguish two different averaging scales: the turbulence averaging scale needed for the definition of the turbulence fluctuations (τ) and a flux averaging time scale.

3.3.1 Fourier analysis

Continuous time series obtained by tower-mounted sonic anemometers record atmospheric motion at scales that span over several orders of magnitude. The application of the eddy covariance method requires the separation of the instantaneous signal into the mean and fluctuating parts (e.g. Večenaj et al. 2011, 2012; Babić

et al. 2012). The implicit assumption that allows us to separate the flow field into mean and fluctuating parts is that of the existence of mesoscale spectral gap (e.g. Večenaj et al. 2012).

The concept of Reynolds averaging is used to analyze the boundary layer turbulence. Reynolds averages are ensemble averages that can be applied only to statistically stationary processes. Because atmospheric observations are inherently non-stationary (in a statistical sense), they must be transformed into time series that are statistically stationary (Section 3.4) so that one may apply Reynolds decomposition. Since single point measurements in space are functions of time, we must assume an ergodic hypothesis and replace ensemble averages with time averages. This action guarantees that the mean of fluctuating components remains zero, while it does not change the mean value for any given variable. The assumption of stationarity is never fulfilled because the majority of meteorological variables show a diurnal cycle. However, quasi-stationary conditions can be achieved by choosing an appropriate flux averaging interval. According to Kaimal and Finnigan (1994), a 1-h period is as long as we can extend the averaging period without accounting for the non-stationarity in the form of diurnal or large scale variations. However, in the SBL this averaging interval is even smaller. For a given time series for any function of a single independent variable $x(t)$ we write:

$$x(t) = \overline{x}(t) + x'(t). \tag{3.8}$$

In this way, we separate the slowly varying, almost "passive" large scale changes in $x(t)$, which we write as $\overline{x}(t)$, from the rapid, "active" turbulent variations, $x'(t)$, about $\overline{x}(t)$. The time average is defined as follows:

$$\overline{x}(t) = \overline{x} = \frac{1}{\tau}\int_0^{\tau} x(t)dt. \tag{3.9}$$

We then remove this mean in the period τ, which represents the size of a moving average, to define the turbulent perturbation. This averaging interval can be derived from the spectrum of atmospheric motions, which often show a gap between periods of 20 min to 1 hour (e.g. Van Gorsel 2003).

One of the ways to perform a spectral analysis is by Fourier analysis. Here, we estimate turbulence averaging intervals by applying two methods, both based on Fourier analysis. As already noted, assuming Taylor's frozen turbulence hypothesis we can make conversion from space scales (wave number) to the frequency domain. In this context, spectral analysis is a very useful tool for deriving information on large-scale to small-scale eddy energy transport. The value of the spectrum at a specific frequency is equal to the mean energy in that eddy size. For the calculation of the power spectra and cospectra of the three dimensional wind velocity components

and sonic temperature a Fast Fourier Technique (FFT) is used.

The Fourier theorem states that function $g(t)$, which is a time series of a meteorological parameter with turbulent fluctuations (i.e. wind components or sonic temperature), can be represented by a system of orthogonal sine and cosine functions with appropriate amplitude and phase:

$$g(t) = \sum_{k=-\infty}^{\infty} c_k e^{ikt}, \tag{3.10}$$

$$c_k = \frac{1}{2\pi} \int_{-\infty}^{\infty} g(t) e^{-ikt} dt, \qquad e^{ikt} = \cos(kt) + i \sin(kt). \tag{3.11}$$

The Fourier transform (FT) uses this concept to transform between time and frequency domains. For the same continuous function $g(t)$, the FT is defined as

$$\hat{G}(f) = \int_{-\infty}^{\infty} g(t) e^{-i2\pi ft} dt, \tag{3.12}$$

with f being natural frequency. The inverse FT is

$$g(t) = \frac{1}{2\pi} \int_{-\infty}^{\infty} \hat{G}(f) e^{2\pi ft} df. \tag{3.13}$$

The time integral over the frequency spectrum (3.12) corresponds to the variance.

3.3.2 Ogive functions

The second method based on Fourier analysis used for estimating an appropriate flux averaging time was introduced by Desjardins et al. (1989) and Oncley et al. (1990) for the investigation of turbulent fluxes. This method uses the cumulative or running integral of the cospectrum to determine the frequency at which there is no more contribution to the covariance (e.g. Foken 2008; Babić et al. 2012). This cumulative integral is an ogive function defined by

$$Og_{xy}(f_0) = \int_{\infty}^{f_0} Co_{xy}(f) df, \tag{3.14}$$

where Co_{xy} represents the cospectrum of any two variables x and y (e.g. Oncley et al. 1996; Metzger and Holmes 2008). The integral ranges from a higher frequency (highest frequency recorded) toward a lower frequency (frequency of interest).

The ogive plots show the cumulative contribution of eddies of increasing period to the covariance. If the ogive reaches an asymptote at some frequency f_c, this indicates that there is no more flux beyond this frequency (Moncrieff et al. 2004). The flux averaging time scale is equal to $\tau_F = 1/f_c$. τ_F denotes the minimum averaging time necessary to include all flux contributions, that is, the time scale

which separates local turbulent fluxes that produce surface-layer turbulence from mesoscale/diurnal fluxes (Foken et al. 2006). The ogive and cospectrum provide the same information because a point on the ogive curve is equal to the integral under the cospectral density curve. Another advantage of the ogive plots is that we can determine whether we have sampled the data for a long enough period without needing to compare our measurement to some chosen standard that can be inappropriate for our conditions (Moncrieff et al. 2004).

3.3.3 Multiresolution flux decomposition

The Multiresolution Flux Decomposition (MFD; Howell and Mahrt 1997; Vickers and Mahrt 2003) decomposes variances and/or covariances of physical quantities locally. Multiresolution (MR) analysis applied to time series orthogonally decomposes the record by averaging time series using different averaging lengths (i.e., averages on different time scales). Using the MFD method turbulent fluxes can be analyzed. MR cospectra can be interpreted as fluxes decomposed into values, which are computed from moving averaging windows of different widths. Therefore, the location which corresponds to the maximum in MR cospectra in the time scale domain depends on the time scale of the fluctuations. Contrary to this, the peak in the Fourier cospectra depends on the periodicity. Additionally, the MR cospectra satisfy Reynold's averaging rules at all scales since each mode of the MFD corresponds to a simple unweighted (nonoverlaping) moving average.

We first consider a time series $x_i(t)$ consisting of $i = 1, 2, 3, \ldots, 2^M$ points. MR decomposition divides the data record of length $N = 2^M$ into simple averages of different segments (scales m) of width 2^m ($m = 0, 1, 2, \ldots, M$) consecutive data points (Fig. 3.5). The first step in the MR decomposition is to calculate the simple average over the record. This represents the lowest order mode, that is, the largest averaging timescale and corresponds to $m = M$. This average is then removed from the record. In the next step the means of the two half records are calculated and removed from the corresponding half record. In the third step the averages of the four subrecords are removed, and so forth. The procedure is applied until the highest order mode is reached, which corresponds to $m = 0$ and denotes the shortest averaging scale.

For example, for a given scale m, the averaging segments are sequenced as $n = 1, 2, 3, \ldots, 2^{M-m}$, n representing the position of the segment within the series. The average for the n-th segment at scale $m+1$ is given by (Vickers and Mahrt 2003)

$$\overline{x_n}(m) = \frac{1}{2^m} \sum_{i=2^m(n-1)+1}^{n2^m} xr_i(m), \tag{3.15}$$

where 2^m is the window averaging length, $xr_i(m)$ is the residual series with segment averages for windows of width $> 2^m$ points removed. The integer n identifies the position of the $2^{(M-m)}$ different averaging windows of 2^m points (Fig. 3.5(a)). The $n = 1$ averaging window includes the first 2^m points of the data record, the $n = 2$ average includes the points $i = 2^m, \ldots, 2^{(m+1)} - 1$, and so forth (Fig. 3.5(b)). The MR spectra represent the second moment about the mean of the segment averages and are given by

$$D_x(m+1) = \frac{1}{2^{M-m}} \sum_{n=1}^{2^{M-m}} \overline{x_n}^2(m). \tag{3.16}$$

In an analog way, MR cospectrum of two time series x_i and y_i is:

$$D_{xy}(m+1) = \frac{1}{2^{M-m}} \sum_{n=1}^{2^{M-m}} \overline{x_n}(m)\overline{y_n}(m). \tag{3.17}$$

The sum of $D_{xy}(m)$ over averaging scales $m = 1, 2, \cdots k$ is exactly the eddy covariance flux calculated using an averaging scale of length 2^k points. The maximum in the MR cospectra (decrease in the magnitude with the increasing scale) is associated with the turbulence. Based on the MR cospectra, Vickers and Mahrt (2003) defined a cospectral gap scale (τ_{gap}). This gap scale is then used to separate between turbulence and mesoscale motions. The gap scale can be detected if one of the following criteria is fulfilled: the cospectra changed the sign (zero crossing) or level off at an averaging time scale longer than the turbulence time scale. The leveling off of the cospectra is identified with the accumulative flux changes less than 1% with an increase in the time scale. The accumulative flux can be obtained by summing up the contributions to the flux starting at the smallest scale.

3.3.4 Wavelet analysis

Wavelet analysis differs from other quantitative analytical tools that are usually used to analyze turbulent time series (such as Fourier analysis) primarily in that it is a local transform, and the analysis takes place at a variety of different scales (e.g. Salmond 2005). This yields information about the temporal location of different features (characterized by different frequencies) within the data set to be retained. In this way the wavelet analysis zooms in on a particular feature of the signal and studies locally with a level of detail corresponding to the scale of the feature. Therefore, this technique will be used to filter the signal, thus effectively isolating the turbulent signal from other processes, such as gravity waves or background noise that contaminate the data set.

In this thesis only basic concepts of wavelet analysis are presented following

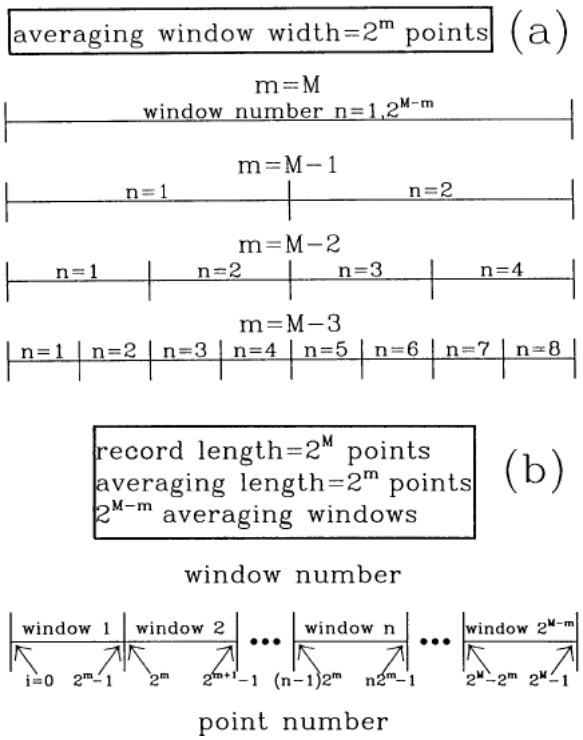

Figure 3.5: **(a)** Schematic representation of the multiresolution flux decomposition method representing averaging window basis set and **(b)** partitioning of the set into 2^{M-m} averaging windows. Adopted from Howell and Mahrt (1997)

Torrence and Compo (1998). A more detailed description can be found in many reference works (e.g. Daubechies 1992; Farge 1992; Lau and Weng 1995).

The wavelet transform (WT) is defined for a time series x_n consisting of N measurements with equal time step δt and $n = 0, 1, 2, \ldots, N-1$. The continuous WT of a discrete series x_n is defined as the convolution of x_n with a scaled and translated version of $\psi(\eta)$ (Torrence and Compo 1998):

$$W_n(s) = \sum_{n=0}^{N-1} x_n \mathbf{\Psi}^* \left[\frac{(n-n')\delta t}{s} \right], \tag{3.18}$$

where $\mathbf{\Psi}^*$ indicates the complex conjugate of the wavelet function $\psi(\eta)$, n' is localized time index and s denotes wavelet scale. The term $\frac{(n-n')\delta t}{s}$ represents a non-dimensional "time" parameter and we denote it as η. The function $\psi(\eta)$ represents normalized function ψ_0 and has unit energy:

$$\psi(\eta) = \left(\frac{\delta t}{s} \right)^{1/2} \psi_0(\eta), \tag{3.19}$$

where $\psi_0(\eta)$ is a wavelet function which has a zero mean and is localized in both time and frequency space (fulfills the admissibility condition) (Farge 1992). In this thesis for the wavelet function $\psi_0(\eta)$ the non-orthogonal complex Morlet wavelet

was chosen:

$$\psi_0(\eta) = \pi^{-1/4} e^{i\omega_0 \eta} e^{-\eta^2/2}, \tag{3.20}$$

with $\omega_0 = 6$ being the non-dimensional frequency for which the admissibility condition is satisfied. The Morlet wavelet was found to be suitable for statistical analysis and for the pattern recognition in turbulence data (e.g. Farge 1992; Salmond 2005; Cuxart et al. 2002; Terradellas et al. 2005; van den Kroonenberg and Bange 2007). By varying the wavelet scale s and translating along n, it can be shown how the amplitude of any feature versus the scale changes with time as well as how this amplitude changes with time. Equation 3.18 shows a convolution of x_n and $\mathbf{\Psi}^*$ and this convolution should be done N times for each scale s. This is considerably faster if calculated in Fourier space. The convolution theorem[1] allows us to do all N convolutions simultaneously using a discrete Fourier transform (DFT). Using the convolution theorem and inverse FT, Eq. 3.18 can be rewritten as

$$W_n(s) = \sum_{k=0}^{N-1} \hat{x}_k \widehat{\mathbf{\Psi}}^*(s\omega_k) e^{i\omega_k n \delta t}, \tag{3.21}$$

where $\hat{x}_k$ is a DFT of x_n

$$\hat{x}_k = \frac{1}{N} \sum_{n=0}^{N-1} x_n e^{-2\pi i k n/N}. \tag{3.22}$$

The angular frequency ω_k is defined as

$$\omega_k = \begin{cases} \frac{2\pi k}{N\delta t}, & k \leq \frac{N}{2} \\ -\frac{2\pi k}{N\delta t}, & k > \frac{N}{2} \end{cases} \tag{3.23}$$

$(k = 0, 1, 2, \ldots, N-1)$. The FT of the function $\psi(\eta)$ is given by $\hat{\psi}(s\omega)$

$$\hat{\psi}(s\omega_k) = \left(\frac{2\pi s}{\delta t}\right)^{1/2} \hat{\psi}_0(s\omega_k). \tag{3.24}$$

The function $\hat{\psi}(s\omega_k)$ is a normalization of $\hat{\psi}_0(s\omega_k)$ which ensures that the WTs given by Eq. (3.21) at each scale s are comparable to each other and to the transforms of other time series. The WT uses a fully scalable window of changeable width as the transform is computed at different scales, and therefore it optimizes the time resolution.

The wavelet power spectrum ($WPS_n(s)$) is defined as squared absolute amplitude of the complex wavelet coefficients

[1] The convolution theorem states that the FT of any convolution can be interpreted as the product of its FTs.

$$WPS_n(s) = \frac{W_n(s)W_n^*(s)}{s} = \frac{|W_n(s)|^2}{s}. \tag{3.25}$$

The power spectrum is divided by scale it associates in order to correct the bias observed in favor of large scales or low frequencies (Liu et al. 2007).

A set of scales s ($s = s_j$) used in the WT can be chosen arbitrarily in the case of non-orthogonal wavelets; in this case a more complete picture can be built up (Torrence and Compo 1998). The scales s_j are defined as follows

$$s_j = s_0 2^{j\delta j}, \qquad j = 0, 1, \ldots, J \tag{3.26}$$

where s_0 describes the smallest resolvable scale, δj is the spacing between the scales and J is the largest scale

$$J = \frac{1}{\delta j} \log_2 \left(N\delta t / s_0 \right). \tag{3.27}$$

The relationship between equivalent Fourier period (FP) and the wavelet scale s is given by:

$$FP = \frac{4\pi s}{\omega_0 + \sqrt{2 + \omega_0^2}}. \tag{3.28}$$

For the Morlet wavelet (with $\omega_0 = 6$) the wavelet scale is almost equal to the FP. Thus, $s_0 = 2\delta t$ should be chosen to have the equivalent FP approximately $2\delta t$. Smaller values of δj will give finer resolution, and a δj of about 0.5 is the largest value that ensures adequate sampling in scale.

The local wavelet power spectrum is defined as a vertical slice through the wavelet scales at a certain time. Thus, the time-averaged wavelet spectrum over a certain period is

$$\overline{W}_n^2(s) = \frac{1}{n_a} \sum_{n=n_1}^{n_2} |W_n(s)|^2, \tag{3.29}$$

where the new index n indicated the midpoint of n_1 and n_2 and $n_a = n_2 - n_1 + 1$ represents the number of point averaged over. The global wavelet power spectrum is the average over all the local wavelet spectra

$$\overline{W}^2(s) = \frac{1}{N} \sum_{n=0}^{N-1} |W_n(s)|^2. \tag{3.30}$$

The results of wavelet analysis applied to our data are presented in Chapter 4, Section 4.4.

3.4 Stationarity of the time series

Stationarity of the time series is a fundamental assumption of similarity theory. Thus, it should be tested prior to evaluation of similarity theory. Večenaj and De Wekker (2015) performed a comprehensive analysis to detect non-stationarity based on various tests proposed in the literature. They found that the Foken and Wichura (1996) test most often detects the largest number of non-stationary time intervals among all the tests investigated. They concluded that non-stationarity significantly decreases if detrending or high-pass filtering is applied, since highly non-stationary (sub)mesoscale motions are removed by filtering. Therefore, while testing non-stationarity of our datasets, we first removed the linear trend for each 30-min interval and then applied the Foken and Wichura (1996) test to the filtered time series. The stationarity test of Foken and Wichura (1996) assumes that second order moments of stationary time series converge to stable values with increasing averaging time, that is

$$FW = \left| \frac{\overline{Q_{x,y}}(5\text{min}) - Q_{x,y}(30\text{min})}{Q_{x,y}(30\text{min})} \right| \cdot 100\%, \tag{3.31}$$

where $Q_{x,y}$ represents any second order moment (variances and covariances) averaged over 5 and 30 minutes. FW denotes the absolute value of the ratio between the difference of the flux averaged over six 5-min subrecords and the flux averaged over the total 30-min interval, to the flux obtained over the total 30-min period. The observed time series is declared non-stationary if the FW fraction is above the threshold value of 30%.

The percentage of non-stationary periods for our dataset over heterogeneous terrain in the SBL varied between 20 and 30 % depending on the level of observation (Tabe 3.2). This result indicates slightly lower number of stationary intervals compared to results obtained in recent studies over complex mountainous terrain of Večenaj and De Wekker (2015) and Stiperski and Rotach (2016).

3.5 Statistical uncertainty

The statistical uncertainty (or sampling error) is inherent to every turbulence measurement. The assessment of the statistical uncertainty is related to the averaging period. In order to estimate statistical uncertainty we followed Stiperski and Rotach (2016). This test was performed on the time intervals which were declared stationary by the foregoing test. The statistical uncertainty was estimated for the momentum and heat fluxes, and for the variances:

$$a_x^2 = \frac{4(z-d)}{T_a \overline{u}} \left[\frac{\overline{(x')^4}}{\overline{(x')^2}^2} - 1 \right], \tag{3.32}$$

$$a_{xy}^2 = \frac{z-d}{T_a \overline{u}} \left[\frac{\overline{(x'y')^2}}{u_{*\ell}^4} - 1 \right], \tag{3.33}$$

where x' and y' represent turbulent fluctuations of any turbulence variable. This was done for the fixed averaging period T_a= 30 min. Although over ideally flat and homogeneous surfaces one might choose 20 % as a limit of statistical uncertainty, we chose the 50 % to assure both, high quality data sets, and a significantly large amount of input data for the similarity analysis (e.g. Stiperski and Rotach 2016). Thus, for the subsequent analysis only 30-min intervals associated with statistical uncertainty below 50 % were chosen. The uncertainty was largest for the kinematic heat flux while for variances it was on average smaller than 50 %.
Finally, according to the QC recommendations proposed by e.g. Klipp and Mahrt (2004) and Grachev et al. (2014) the following thresholds were imposed: data with the local wind speed less than 0.2 ms^{-1} were omitted, while minimum thresholds for the kinematic momentum flux, kinematic heat flux, and standard deviation of each wind speed component were 0.001 $\mathrm{m}^2\mathrm{s}^{-2}$, 0.001 Kms^{-1} and 0.04 ms^{-1}, respectively.

Table 3.2: Number of 30-min intervals that satisfy the minimum QC (no large data gaps, no unrealistic values and no spikes) within the observational period of 88 nights (out of the total of 2112 intervals). The number of stationary and also the number of time intervals which are stationary and have uncertainty < 50 % (used for the analysis in this study) is given.

Criteria	Level 1	Level 2	Level 3	Level 4	Level 5
Minimum QC	647	802	1898	564	803
Stationary	482	576	1323	388	649
Stationary & Uncertainty $< 50\%$	342	388	760	225	357

3.6 Estimation of the flux footprint

Footprints are estimated and used in order to facilitate an interpretation of the results. Recently, Kljun et al. (2015) presented a new parameterization for Flux Footprint Prediction (FFP) which has improved footprint predictions for elevated measurement heights in stable stratification. Furthermore, the effect of the z_0 has been implemented into the scaling approach. It is based on the scaling approach of flux footprint results of a thoroughly tested Lagrangian footprint model. The two-

dimensional flux footprint model of Kljun et al. (2015) (http://footprint.kljun.net/) was used to estimate the distance of the surface upwind of the measurement tower, that defined the fetch (flux footprint function) for the measurements at each level during statically stable conditions. As input parameters the mean standard deviations of lateral wind component (σ_v = 0.40, 0.45, 0.41, 0.46 and 0.46 ms^{-1} for levels from 1 to 5, respectively), the mean local Obukhov lengths (Λ = 33, 28, 38, 45 and 39 m), the mean friction velocities (u_* = 0.23, 0.20, 0.19, 0.22 and 0.21 ms^{-1}) and correspondingly, mean wind velocity for each measurement height (U = 1.9, 2.9, 3.1, 4.0 and 4.1 ms^{-1}) were used. The height of the SBL was set to 250 m since the result did not exhibit noticeable sensitivity to its choice. The peak location of the footprint function, i.e. location of the maximum influence on the measurement, increases with increasing height and varies between 19 and 405 m from the lowest to the highest observational level, respectively. Additionally, the distance from the receptor that includes 90 % of the area influencing the measurement (x_R) increases with height, where $x_R \approx$ 65, 331, 570, 1260 and 1300 m, correspond to levels 1 to 5, respectively.

Chapter 4

Timescales in the nocturnal boundary layer

The application of the eddy covariance method requires separation of instantaneous signal into the mean and fluctuating parts (e.g. Metzger and Holmes 2008; Večenaj et al. 2011, 2012). The concept of this decomposition has existed for over a century and was introduced by Osborne Reynolds in, what is now considered, his classic paper (Reynolds 1895). One of the key features of this approach is the averaging, which defines the mean, variance and covariance and consequently simplifies the governing equations for turbulent flow (e.g. Stull 1988). The implicit assumption that allows us to separate the flow field into its mean and fluctuating parts is that of the mesoscale spectral gap (e.g. Večenaj et al. 2012). The first evidence of this gap in the horizontal wind speed spectrum was observed by van der Hoven (1957). In his study, a separation of scales was evident due to the appearance of a large spectral gap that contained very low energy between the microscale and synoptic scale peaks. Many numerical atmospheric models use grid spacing that falls within the spectral gap, which means that large-scale motions can be resolved, while the small-scale features, such as covariances of momentum, sensible heat, moisture and concentration, are parameterized in order to close the Reynolds averaged equations (e.g. Stull 1988).

The application of the Reynolds decomposition requires transformation of non-stationary atmospheric motions into statistically stationary time series. Turbulent motions are unsteady by definition (e.g. Agrawal 1997). However, a turbulent flow can be statistically stationary. According to e.g. Pope (2000), random field $u(x,t)$ is statistically stationary if all statistics are invariant under a shift in time; in other words, the statistical properties do not change in time. The transformation into statistically stationary time series can be performed using a mean removal process or filter. The mean removal process determines the integral time scale for turbulent time series, τ. It is important, however, to make a distinction between the averaging

time T, which is required for the convergence of statistical moments (e.g. Lumley and Panofsky 1964; Sreenivasan et al. 1978; Lenschow et al. 1994), and the time scale τ. We require that the averaging time is much longer than the period of fluctuations in the original time series, $\tau/T << 1$ (Kristensen 1998). In statistically stationary processes, $T \approx \tau$ (e.g. turbulence generated in laboratory experiment). However, for non-stationary processes, τ represents the time scale of the slowest energetic motions, while T represents the averaging time that governs the convergence of variance (Metzger and Holmes 2008).

In experiments performed during the past several decades, time periods between 10 and 60 min were usually used as the averaging interval T over which to calculate means and products of turbulence variables regardless of static stability, turbulence levels or other factors (Oncley et al. 1996). Based on results from the 1968 Kansas data, Wyngaard (1973) showed that the averaging time increases with the order of the moment of the statistic and with increasing static instability. For example, for Reynolds stress components $\overline{u'w'}$ and $\overline{v'w'}$, τ was predicted to be on the order of hours for statically unstable conditions and it was larger than times needed for convergence of scalar covariances and other lower order statistics.

A multitude of papers on methods describing techniques for the mean removal operation, such as temporal filtering (Moore 1986; McMillen 1988), linear detrending (Stull 1988; Kaimal and Finnigan 1994) or sliding windows (Rannik and Vesala 1999; Sakai et al. 2001; Večenaj et al. 2010) can be found. Each of these methods, however, requires a specification of the integral time scale to define the "mean" quantity. Vickers and Mahrt (2003) propose a multiresolution flux decomposition method for selecting an appropriate time scale for the mean removal process during statically stable and near-neutral conditions. It has been shown that different integral time scales should be used for different conditions of atmospheric stability. For example, Sozzi and Favaron (1997) found that good averaging time under convective conditions is $30-60$ min, while Metzger and Holmes (2008) found that for the same conditions over Utah's western desert, an appropriate mean removal time scale is between 20 and 27 min. Vickers and Mahrt (2003) have shown that the average time scale increases with instability because of large convective eddies and decreases with increasing stability due to the suppression of large eddies by stratification. They found an average time scale of 9 min for near-neutral conditions, which decreases sharply with increasing stability to 100 s for strong static stability. Many studies indicate that an appropriate integral time scale is highly site specific and therefore should be calculated locally.

This chapter describes the application of two methods based on a Fourier analysis and two methods based on wavelet analysis to estimate characteristic time scales in statically stable, wintertime, night-time ground-based layer.

4.1 Fourier analysis

The first of four methods employed to determine an appropriate turbulence averaging time scale is Fourier spectral analysis. The spectra were calculated by multiplying the 2-hr periods of u, v, w time series with a Hamming window with 2^{16} data points (approximately 54.5 min) and 50 % overlapping; a FFT algorithm was used to perform the FT. The FFT was then multiplied by its complex conjugate, and the real part of this product was maintained.

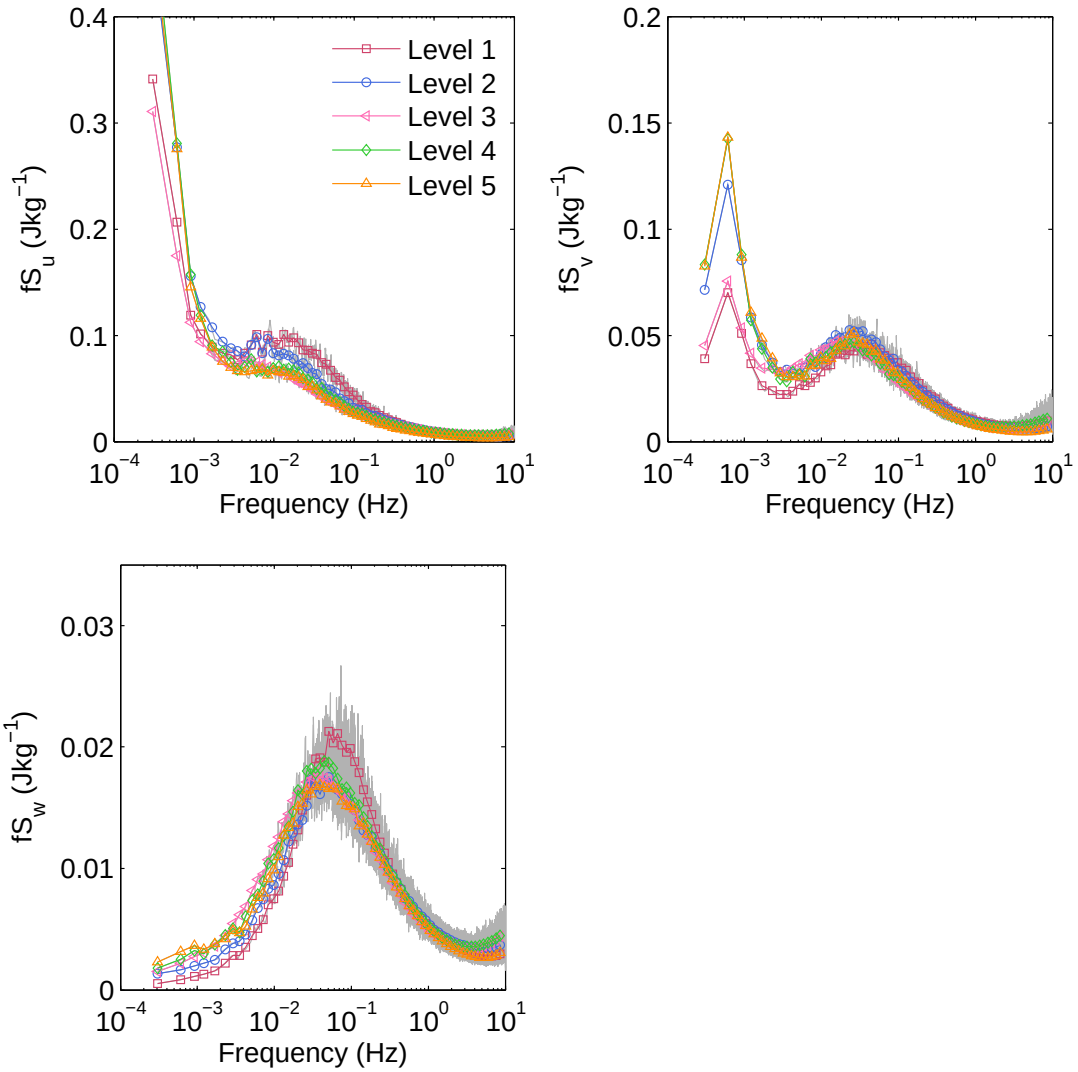

Figure 4.1: A log-linear representation of the mean energy spectrum of the velocity components (top left: longitudinal top right: lateral, lower panel: vertical) at all five measurement levels. The background gray lines indicate the mean raw spectra.

Figure 4.1 shows a log-linear representation of the frequency weighted average spectra of all three velocity components at all five measurement levels. This type

of spectral representation is proportional to the energy since the area under any portion of the spectral curve is proportional to the variance, i.e. energy (e.g. Stull 1988). Although, the individual spectra are quite scattered (not shown), the mean u and v spectra show an existence of an energy gap, which is more pronounced for the lateral wind component since it contains less energy at larger scales compared to the longitudinal component. The observed energy gap is found between approximately 400 and 100 s and this corresponds to the time scale τ. The vertical velocity component has the lowest energy magnitudes compared to the horizontal components, and its spectra reveal no energy gap. This is expected since the large scale motions have typically small vertical velocities and consequently low energy levels. The area under the fS_w curve represents the turbulent portion of the spectral energy indicating the largest contribution coming from eddies at time scales between 250 and 1 s.

4.2 Ogive functions

A relevant flux averaging time scale can be determined from the cospectrum of the kinematic heat flux (e.g. Oncley et al. 1996; Foken et al. 2006; Metzger and Holmes 2008). As described in Section 3.3, the ogive function is a cumulative integral of the cospectrum, and thus, when an ogive starts to converge from a certain frequency, this can be interpreted that there is no more contribution to the flux beyond this frequency. Therefore, the period corresponding to this frequency can be considered as the flux averaging period.

Figure 4.2 shows the mean raw and smoothed kinematic heat flux ($\overline{w'\theta'}$) cospectra as well as the corresponding ogives for all five levels. The cospectra were calculated using the same technique as described for the velocity components spectra. We consider corresponding ogives in order to estimate the appropriate averaging time scale. As pointed out by Foken et al. (2006), in an ideal case, the ogive function increases during integration from high frequencies to low frequencies until a certain value is reached and remains more or less constant before a 30 min integration time. Because of the variability of spectra, deviations of 10 % for the plateau value can be tolerated. We note that in our case this condition is fulfilled for the mean ogives at nearly all levels. This means that 30 min is a reliable estimate of the averaging period T for the calculation of turbulent flux, because we can assume that the whole turbulent spectrum is covered within that interval and that there are only negligible flux contributions from longer scales (Foken et al. 2006). Additionally, an appropriate time averaging is needed to reduce the random errors in the turbulent fluxes. Namely, random errors are defined as the errors due to an insufficient averaging period for which the time mean converges to the ensemble mean as required

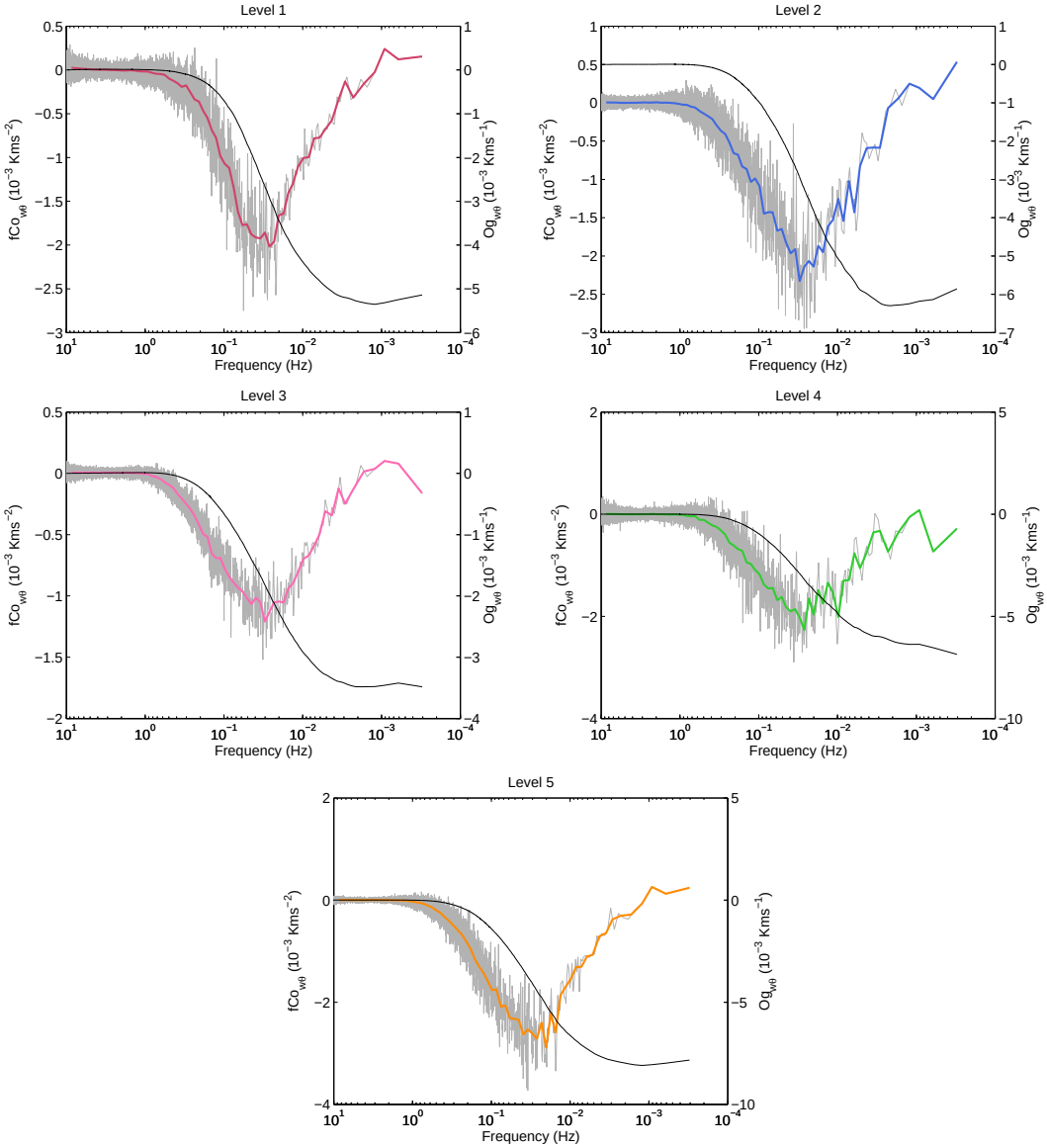

Figure 4.2: The mean raw cospectrum (gray, left y-axis) and ogives (black, right y-axis) of the kinematic heat flux for all five measurement levels (indicated on the top x-axis). Colored curves correspond to the smoothed cospectrum, which was obtained by averaging raw cospectrum within each of 62 frequency bands equally spaced on logarithmic scale.

by the ergodic hypothesis. However, maximum possible averaging times are limited by the diurnal evolution of the ABL to periods not much longer than 1h in order to avoid strong influence of non-stationarity effects (e.g. Stull 1988). Thus, we consider $T = 30$ min to be an optimal period over which turbulent fluxes were averaged.

4.3 Multiresolution Flux Decomposition

The multiresolution decomposition enables the investigation of scales of motion responsible for scalar fluxes (e.g. Vercauteren et al. 2016). For this purpose, the

MFD of the heat flux is often used to separate turbulence scales from motions on larger scales. The first step is, thus, to identify the gap scale in the MR cospectra, which is typically associated with very small MFD flux values. Since the heat flux in the SBL is nearly always downward, the cospectra show a negative peak at averaging scales shorter than the gap scale. This peak is followed by a decrease of flux magnitude towards larger time scales and then followed by a sign change or by leveling off. This smaller-scale portion is then identified as the turbulent portion of the flux.
If the gap timescale is employed in the calculation of turbulent fluctuations, contamination by mesoscale motions should be removed. Accordingly, Vickers and Mahrt (2003) have shown better agreement with similarity relationships when the turbulent portion of the total flux was isolated, then when considering the total flux calculated using a fixed averaging time scale. However, the gap region is typically harder to identify for the more stable cases and the cospectra can be erratic.

Figure 4.3 illustrates the total heat flux distribution across the scales of motions by showing individual and averaged MR cospectra for each 30-min record at each level. We note that individual cospectra can vary substantially between the records and although most of them indicate downward heat flux, some periods with weak upward heat flux can be observed. As the averaging scale increases, the MR cospectra start to vary erratically indicating the influence of submeso motions to the heat flux (e.g. Vercauteren et al. 2016). It is worth noting that a large number of data is included in this analysis and no filtering is done based on the stability or stationarity criteria, since these depend on the choice of the appropriate turbulence averaging scale. However, when averaged over many half hour periods, MR cospectra reveal the average picture of scales of motion for the investigated period. For each level we note the presence of the negative peak in the cospectra which is followed by a decrease of the flux magnitude and leveling off of the heat flux. The corresponding integral times scales inferred from the average spectra appear to be somewhat smaller than 200 s. Additionally, the submeso motions do not seem to contribute significantly to the heat flux as they appear to average out to small value, except for the largest scales ($\approx$ 1000 s). Our average MR cospectra show similarities with the Cluster 2 cospectra in the study of Vercauteren et al. (2016), but with somewhat larger turbulent scale. For scales smaller than 200 s, some small variability between individual cases is observed for levels $2-4$ (shown by the error bars). For larger scales, the cospectra average to a small value, but the variability between the records is large.

In this thesis, based on the spectral analysis and MFD method a gap timescale of 100 s was chosen in order to avoid any contribution from submeso motions for the statically strongly stable periods. This is shorter than previously found for one

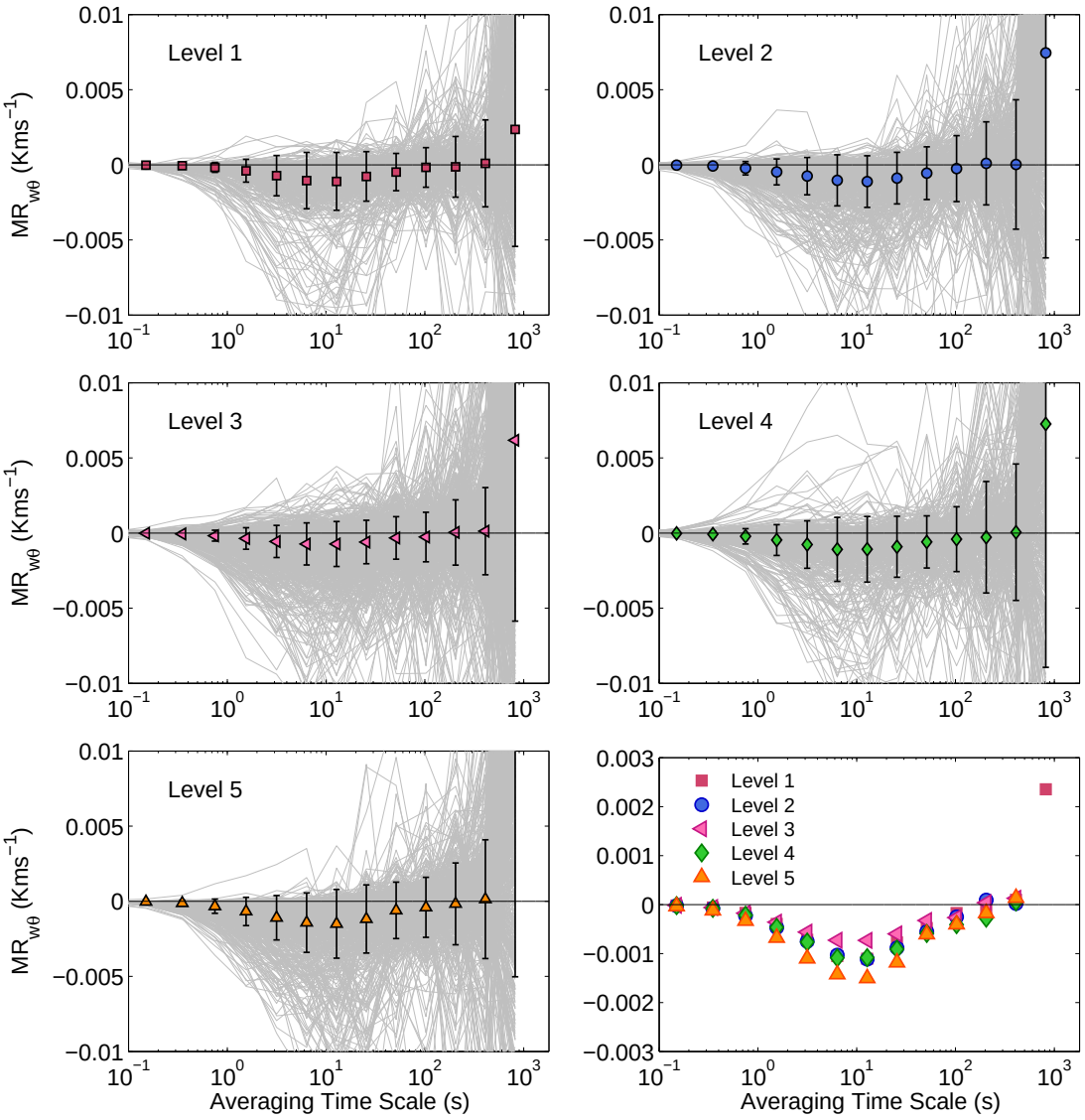

Figure 4.3: Multiresolution decomposition (MRD) of the sensible heat flux. Individual MR cospectra calculated for each 30-min period are shown in gray, while the averages of individual MR cospectra for each level are shown with corresponding symbol and color. Error bars show ± one standard deviation of the between-record variability.

night case study (Babić et al. 2012). This timescale is therefore used for a high-pass filtering of the time series of raw u, v, w and T_s by applying a moving average. Since averaging over longer time period reduces random flux errors in the case of relatively stationary turbulence, turbulent variances and covariances in the present study correspond to 30-min averaged data. The mean wind speed and wind direction were derived from the sonic anemometer data.

4.4 Wavelet analysis

As already pointed out, the wavelet method gives a time-frequency representation of the time series, which provides an opportunity to determine the dominant modes of the signal as well as their time evolution. A first application of the wavelet method to study the SBL was given in Terradellas et al. (2001) and Cuxart et al. (2002). Terradellas et al. (2001) used the wavelet transform to detect and characterize structures in the SBL, while Cuxart et al. (2002) used it to study pressure perturbations and its vertical structure based on measurements from the CASES-99 field experiment (Poulos et al. 2002). The application of the wavelet method in their study allowed the estimation of the turbulent pressure fluxes which are usually difficult to determine directly due to inadequate sampling rate. Consequently, the contribution of the pressure transport term to the TKE budget equation could be discussed. Few years later, Terradellas et al. (2005) used the wavelet method to estimate TKE and turbulent fluxes and found that it performs much better as a filter than the traditional averaging method. They also analyzed two different coherent structures: a density current and a train of internal gravity waves. Salmond (2005) presented a technique based on the wavelet analysis which objectively isolates intermittent turbulent bursts within vertical velocity time series allowing the quantitative description of global intermittency in the very SBL. This technique was used to get insight into the complex relationship between the air quality and intermittent turbulence, showing that the strength and duration of turbulent bursts can play an important role in determining local surface concentrations. For the verification of the gap time scales determined by MFD method, van den Kroonenberg and Bange (2007) used the wavelet transformation. They obtained the identical gap time scale between turbulent and mesoscale fluxes by both methods. The additional information about the homogeneity of the fluxes and the variability of the scales with time was obtained from the wavelet covariance.

I applied wavelet analysis in order to get an insight into turbulence characteristics, i.e. its intermittency and time variability of the scales. Figure 4.4 shows a time-frequency representation of the wavelet power spectrum of the normalized vertical velocity component measured during the night 5–6 December 2008. Wavelet analysis allows the investigation of how turbulent activity is changing during the night, and we can observe a period of strong turbulence at scales between 1 and 200 s, but also periods without turbulence. An approximately 2.5 h long period (between 1930 and 2200 LST), which is especially evident at higher levels far above the canopy, without almost any turbulent activity was observed. This period was characterized by small wind speeds (< 4 ms^{-1} even at the highest 62 m level), weak heat flux and very weak mixing (not shown). Around 2300 LST a frontal passage

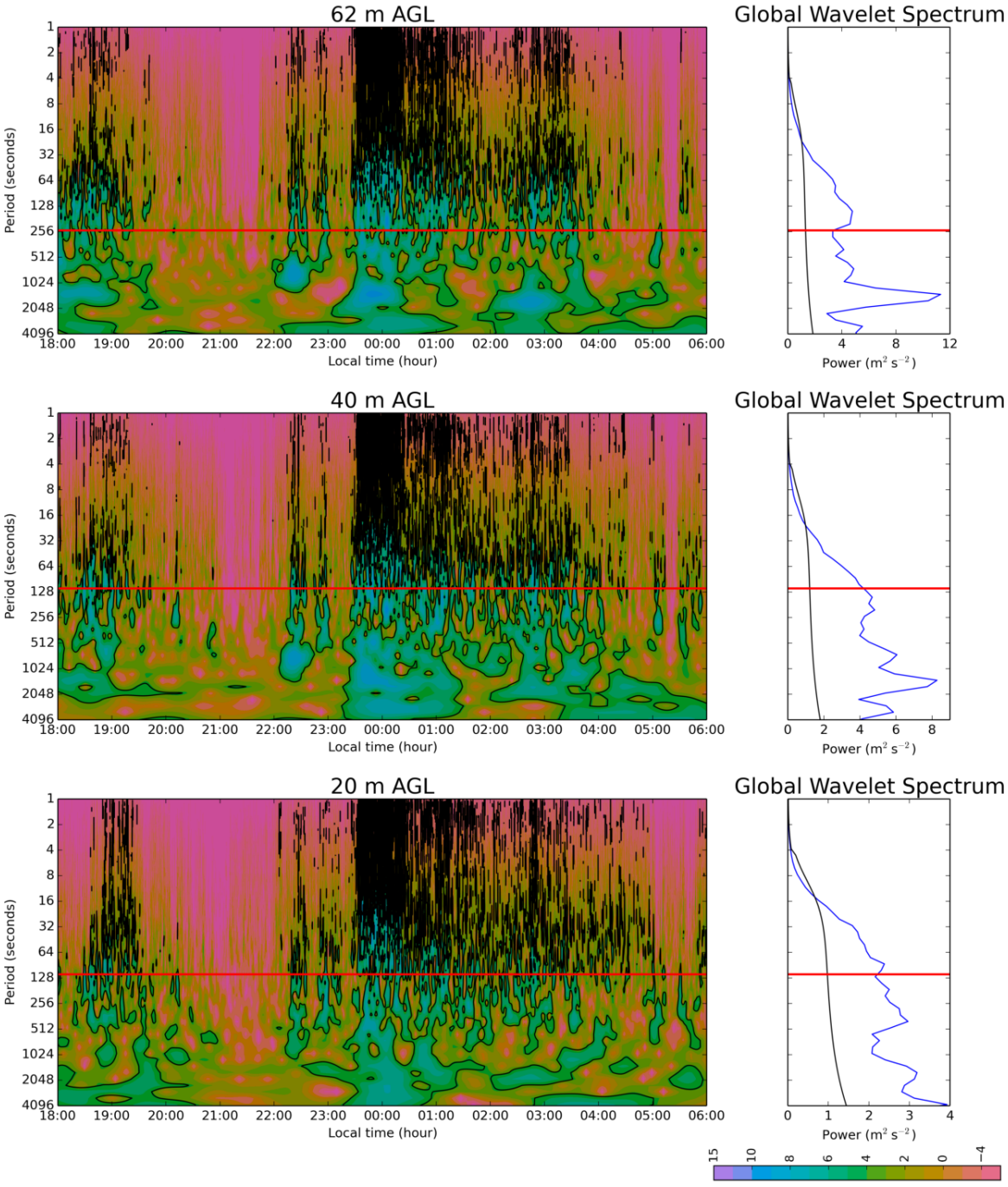

Figure 4.4: Wavelet power spectrum of the vertical wind speed recorded on the night 5 – 6 Dec 2008. On the right a global wavelet spectrum, which is the average of all local wavelet spectra, is shown. Red horizontal lines indicate the gap time scale observed in the Fourier spectra while black contours show 95% confidence level.

occurred, which increased turbulent mixing and heat flux, and recorded wind speeds were > 4 ms^{-1} at the four upper levels and around 3.5 ms^{-1} at the 20 m level in the period between 2300 and 0400 LST (not shown). This can be observed in the wavelet power spectrum as an increased energy. A defined peak of energy con-

strained to a relatively narrow range of periods between 9 and 17 min is observed around 2230 LST in the layer 32–62 m as well as defined structures which correspond to time scales between 17 and 34 min with energy maxima observed around 1800–1900, 2330–0030 and 0200–0300 LST. This indicates that wavelet analysis can be a powerful tool in investigating coherent structures in the SBL (e.g. Barthlott et al. 2007). These structures observed in our case study indicate possible occurrence of gravity waves since observed periods are not unusual for gravity waves (e.g. Terradellas et al. 2001). However, this is only a hypothesis and detailed investigation of coherent structures is out of the scope of this thesis. The global wavelet spectrum shown for this one night case study, which represents the average over all local wavelet spectra, shows relatively good corresponence to the choice of the turbulence averaging time scale for the entire dataset.

Chapter 5

Evaluating Local Similarity Theory

In Chapter 4 turbulence timescales were analyzed using four different methods and appropriate averaging time scales for calculation of turbulent fluctuations and turbulent fluxes were obtained. This chapter addresses the first objective of the thesis, i.e. the applicability of local similarity scaling in terms of flux-variance and flux-gradient relationships in the NBL over inhomogeneous surface.

5.1 Flux-variance similarity

Variances of wind velocity components provide important information on turbulence intensity for the modeling of TKE as well as for transport of scalar quantities. In this section we evaluate similarity of scaled standard deviations of wind velocity components. Normalized standard deviations of wind components are plotted as a function of the local stability parameter in Figs. 5.1 and 5.3. Figure 5.1 shows that scatter of the data (gray symbols) increases with increasing height, where standard deviations of 0.27, 0.29, 0.41, 0.36 and 0.34 ms^{-1} correspond to levels from 1 to 5, respectively. Note that the number of data is the largest at level 3. Moreover, after applying strict quality control criteria the scatter is substantially reduced (standard deviations in the range 0.21 – 0.23 ms^{-1}). This is similar to results of Babić et al. (2016b), and opposed to some other studies in complex terrain, e.g. Wood et al. (2010); Fortuniak et al. (2013); Nadeau et al. (2013). Stationary data that exceed uncertainty threshold of 50 % are presented in order to show the influence of small fluxes (which are difficult to measure and hence uncertain) on the scatter of $\sigma_w/u_{*\ell}$ (presented as gray symbols in Fig. 5.1). As seen from Fig. 5.1, this criterion is crucial for excluding the high values of the scaled vertical wind variance in the strongly stable regime where z-less scaling should be valid. Without exclusion of

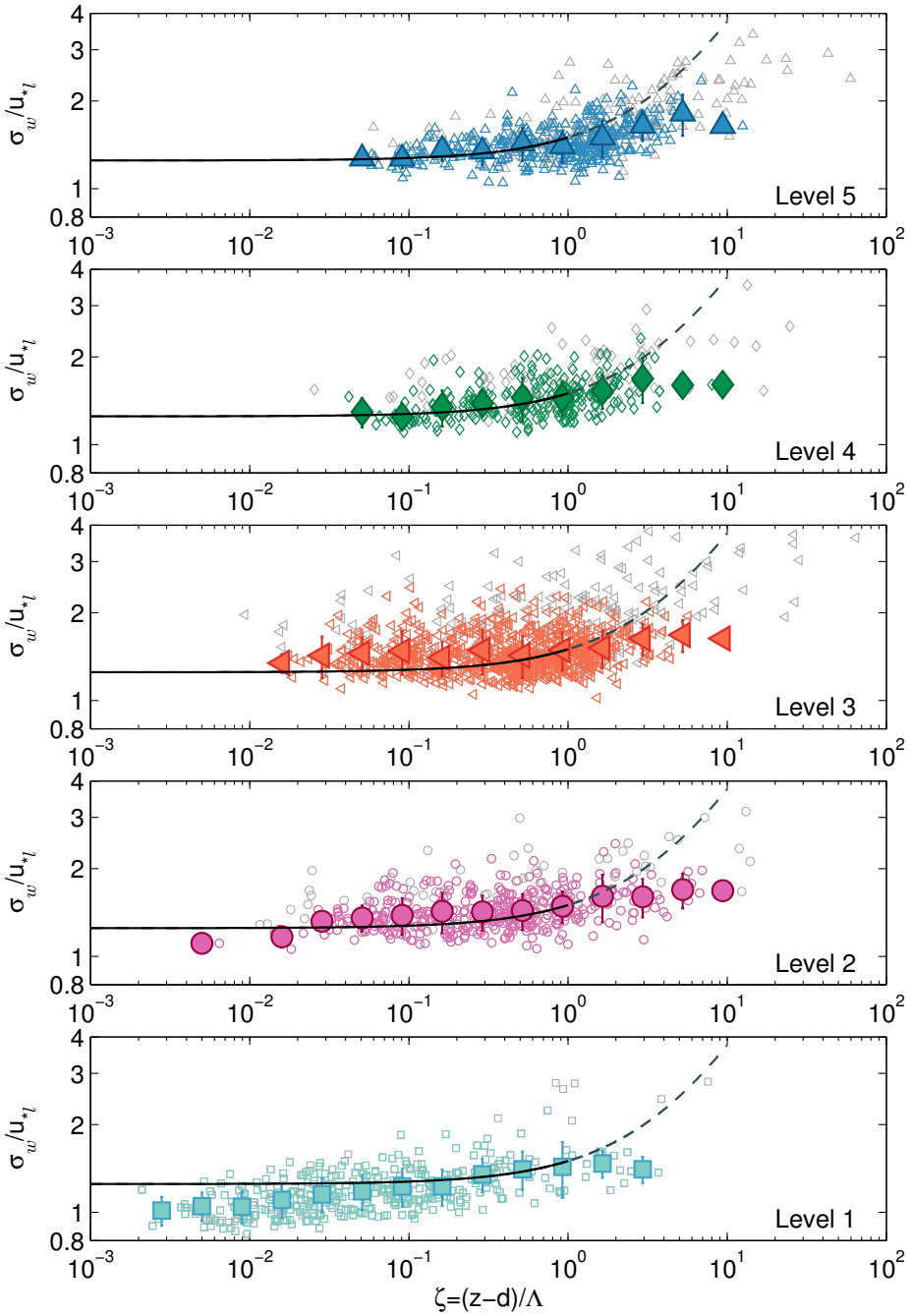

Figure 5.1: Scaled standard deviation of vertical velocity fluctuations as a function of stability. Black solid line ($0 < \zeta < 1$): $\phi_w = 1.25(1 + 0.2\zeta)$ (from Kaimal and Finnigan 1994). Thin dashed line is an extension for $1 < \zeta < 10$. Individual data at each level are shown as background symbols (gray symbols represent stationary data which exceed uncertainty threshold of 50%). Error bars indicate one standard deviation within each bin. The bin size is determined in a logarithmic scale using fifteen equally spaced bins in the stability range $0.002 < \zeta < 12.5$.

highly uncertain data, an incorrect conclusion on the validity of z-less scaling might be drawn. In the subsequent analysis these data are omitted. Individual data as

well as bin-averages in all figures correspond to data (namely, wind and temperature variances and turbulent fluxes) which satisfy an uncertainty limit < 50 %.

To evaluate the similarity of the scaled standard deviations the relationship form (2.4) was used, where a_i, b_i and c_i $(i = u, v, w)$ are free fitting parameters (e.g. Wood et al. 2010). The best-fit coefficients were obtained using a robust least-squares fit of all 30-min data (Table 5.1). We note that values of fitting parameter a_i (neutral limit) for all three non-dimensional velocity variances are smallest at the lowest measurement level. Also, they are smaller than the canonical values found for flat and uniform terrain ($\sigma_u/u_* = 2.39 \pm 0.03$, $\sigma_v/u_* = 1.92 \pm 0.05$ and $\sigma_w/u_* = 1.25 \pm 0.03$, Panofsky and Dutton (1984)), which clearly indicates influence of the RSL. This justifies estimates of the vertical structure and footprints described in Chapter 3. Turbulence characteristics and transport of scalar and turbulent quantities in this layer are determined by the presence of coherent structures which are generated at the canopy top (e.g. Finnigan and Shaw 2000; Shaw et al. 2006). These coherent eddies and extra mixing are generated by an inviscid instability mechanism (Raupach et al. 1996). Values of $a_{v,w}$ at levels $2-5$ are larger compared to the Panofsky and Dutton (1984) values for the neutral range, while the a_u value for level 2 is larger. For three other levels values are slightly smaller, Table 5.1. Values of $\sigma_w/u_{*\ell}$ larger than 1.25 (value reported for "ideal" flat terrain) are often observed over non-uniform terrain and may be attributed to horizontal momentum transport (Katul et al. 1995).

As already mentioned, flux-variance similarity relationships are influenced by self-correlation. Small values of fitted coefficients b_i and/or c_i indicate the best-fit curve which converges to a constant, i.e. a_i. Consequently, values of R^2_{data} tend to converge to small values or even to zero, while $\langle R^2_{rand} \rangle$ are usually larger which leads to negative values of $R^2_{data} - \langle R^2_{rand} \rangle$. The same result was obtained by Babić et al. (2016b) and, as they pointed out, this presents a limitation of the method since it relies on the linear correlation coefficient and does not allow for a reliable conclusion about self-correlation in the SBL.

Table 5.1: Fitted relationships for non-dimensional standard deviations of wind components. Functional forms (Eq. 2.4) of non-dimensional standard deviations of velocity components were tested using a robust least-squares method.

Level	Height*	$\sigma_u/u_{*\ell}$	$\sigma_v/u_{*\ell}$	$\sigma_w/u_{*\ell}$
Level 1	20 m	$2.10(1+7.27\zeta)^{0.09}$	$1.30(1+1506\zeta)^{0.1}$	$0.94(1+656\zeta)^{0.06}$
Level 2	32 m	$2.48(1+0.57\zeta)^{0.12}$	$2.10(1+9\zeta)^{0.1}$	$1.34(1+3.39\zeta)^{0.08}$
Level 3	40 m	$2.32(1+0.15\zeta)^{0.36}$	$2.00(1+1.9\zeta)^{0.1}$	$1.43(1+0.18\zeta)^{0.26}$
Level 4	55 m	$2.24(1+0.79\zeta)^{0.15}$	$1.70(1+6.7\zeta)^{0.1}$	$1.21(1+15.94\zeta)^{0.07}$
Level 5	62 m	$2.13(1+0.75\zeta)^{0.17}$	$2.00(1+0.9\zeta)^{0.2}$	$1.30(1+0.59\zeta)^{0.22}$

* above ground level

Table 5.2 presents a review of $\sigma_{u,v,w}/u_{*\ell}$ published in the literature for different terrain characteristics under neutral conditions. As already noted, dimensionless velocity variances in the RSL are often lower in comparison with the flat terrain reference of Kaimal and Finnigan (1994). Present results for $\sigma_{u,v}/u_{*\ell}$ at the lowest measurement level are in the range of values obtained within RSLs over forest (Rannik 1998) and urban (Rotach 1993) areas. For levels $2-5$, neutral values are close to those reported by Moraes et al. (2005) and Wood et al. (2010). Using local scaling over the city of London (measurements at 190 m above the ground), Wood et al. (2010) obtained near-neutral limits of $\sigma_i/u_{*\ell}$ $(i = u, v, w)$, which are in accordance with those reported for flat and homogeneous terrain where MOST applies. They concluded that MOST was not affected by many factors, since London is quite flat and there are consistent building heights across a wide area which produced a longer upwind fetch causing the London boundary layer likely to be in equilibrium with the surface. Results for $\sigma_w/u_{*\ell}$ are consistent with Nieuwstadt (1984) who found it to be constant (~ 1.4) in the stability range $0.1 < \zeta < 2$.

Table 5.2: Comparison of non-dimensional standard deviations of the wind speed values in statically neutral conditions from different studies. These near-neutral values correspond to the mean value of scaled standard deviations of wind in the range $0 \leq \zeta \leq 0.05$.

Reference	Site description	$\sigma_u/u_{*\ell}$	$\sigma_v/u_{*\ell}$	$\sigma_w/u_{*\ell}$
Panofsky and Dutton (1984)	Flat (reference)	2.39 ± 0.03	1.92 ± 0.05	1.25 ± 0.03
Rotach (1993)	Urban RSL	2.2	1.5	0.94
Rannik (1998)	Pine forest RSL	2.25 ± 0.31	1.82 ± 0.29	1.33 ± 0.14
Moraes et al. (2005)	Complex (valley)	2.4	2.2	1.2
Wood et al. (2010)	Urban BL	2.36	1.92	1.40
This study - Level 1	Heterogeneous	2.13	1.65	1.11
This study - Levels $2-5$	Heterogeneous	2.41	2.08	1.37

5.1.1 Influence of surface inhomogeneity

Due to the fact that measurements were performed in a very heterogeneous landscape, possible influences of different land-use types on turbulence statistics were investigated by considering changes for different wind directions. Figure 5.2(a) shows the normalized standard deviation of the vertical wind component for each observational level averaged over the entire stability range versus wind direction. For the wind sector $45-90$ deg there is no consistent increase of $\sigma_w/u_{*\ell}$ with height, possibly due to the fact that this narrow wind sector is characterized by a sudden change of surface roughness (from agricultural fields to rough forest) and also by a short fetch (some 70 m). This might indicate a more complex vertical structure than depicted in Fig. 3.3 with flow which has not reached an equilibrium yet. In the $300-360$ deg wind sector, the non-dimensional variance of the vertical

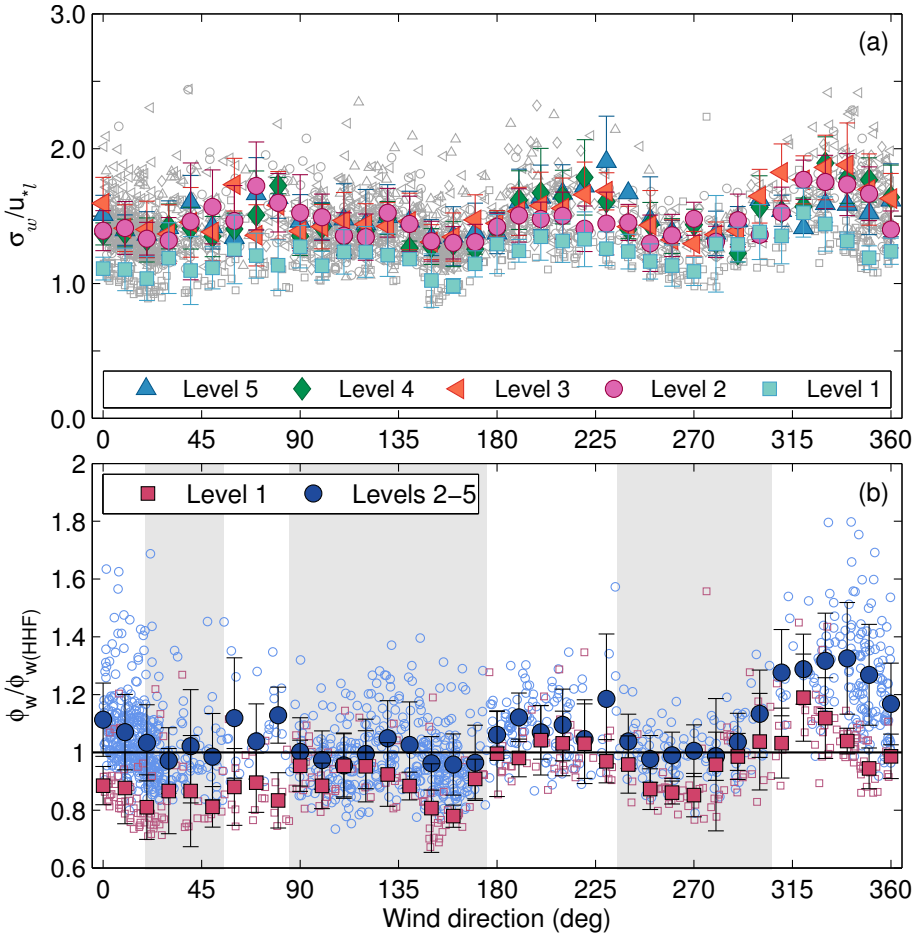

Figure 5.2: **(a)** Scaled standard deviation of vertical velocity fluctuations asfunction of wind direction (regardless of stability). Individual data points at each level corresponding to the particular wind sector are shown as background symbols. Colored filled symbols correspond to bin averages over the entire stability range at each observational level (see inlet). Error bars indicate one standard deviation within each bin. **(b)** Observed dimensionless standard deviation of vertical wind speed relative to the SL similarity prediction for HHF terrain (Kaimal and Finnigan 1994, denoted "HHF") for stability $0 < \zeta < 1$, plotted versus wind direction. Shaded light gray areas indicate the wind azimuths which correspond to the undistorted surface conditions. The flow from other wind directions is considered to be distorted.

wind has lower values at the highest level in comparison with values at levels $2-4$. I hypothesize that this is due to influence of drainage flows from hills located north of the measurement site. Drainage flows are thermally-driven and they occur during the night over sloping terrain often leading to the formation of low level jets. However, the necessary information to substantiate this hypothesis are lacking. In the $190-260$ deg sector, $\sigma_w/u_{*\ell}$ increases with height indicating the flow which has adjusted to the new surface. This sector has the longest fetch (over 300 m) and highly rough but uniform underlying surface (Figs. 3.1, 3.3).

Observed changes of the normalized vertical wind variance with varying wind direction reflect the influence of the surface inhomogeneity (and possibly topography). This influence is seen from the ratio of observed non-dimensional variance of the vertical wind and corresponding values of commonly used similarity formulas for $\sigma_w/u_{*\ell}$ in the "ideal" HHF terrain (e.g. Kaimal and Finnigan (1994), $\sigma_w/u_* = 1.25(1 + 0.2\zeta)$) in the stability range $0 < \zeta < 1$ (Fig. 5.2(b)). We observe that ratio of these two similarity functions at the lowest measurement level is typically < 1, except for the flow from sectors $\approx 200 - 220$ deg and $300 - 340$ deg, which correspond to the high roughness and long fetch (Fig. 3.1) and high wind speeds (Fig. 3.4), respectively. At upper levels values of the ratio $\phi_w/\phi_{w(HHF)}$ are larger than unity for wind azimuth ranges $55 - 80$, $170 - 230$ and $300 - 360$ deg (Fig. 5.2). For these levels, the average $\phi_w/\phi_{w(HHF)}$ ratio in Fig. 5.2 varies between 0.96 and 1.33, which is similar to values of Rannik (1998) for the study over a forest, and the standard deviation for 10 deg wide bins is between 0.08 and 0.22.

Accordingly, I separately analyzed the velocity variances for different wind directions corresponding to undistorted and distorted sectors, respectively. Based on $\phi_w/\phi_{w(HHF)} \approx 1$ undistorted wind directions were defined to correspond to wind directions $20 - 55$ deg, $85 - 175$ deg and $235 - 295$ deg (light gray shaded area in Fig. 5.2). All other wind directions were considered as distorted. The number of data within each group was nearly evenly distributed except for the highest level. Namely, the percentage of data corresponding to the undistorted sectors was 47, 56, 54, 52 and 64 % for levels from 1 to 5, respectively.

Figure 5.3 shows all three non-dimensional standard deviations at the lowest level and for levels $2 - 5$ for undistorted and distorted wind direction sectors separately. We note that the scatter is larger for horizontal components than for the vertical wind component. Also, as one might expect, the scatter is larger for the distorted sectors compared to undistorted. Normalized variances at level 1 show much less dependence on the wind direction compared to levels $2 - 5$. This reflects the rather local RSL impact that determines the statistics. That is, RSL turbulence appears to be affected by a fetch of less than 100 m from the tower as was estimated by the flux-footprint model (Section 3.2) rather than by the more distant complex surface. Differences between distorted and undistorted sectors at this level are only found in the near-neutral regime with larger magnitudes for the distorted sectors.

For levels $2 - 5$ we observe that the overall shape of the curves for the two sectors is quite similar for all three wind variances. Dimensionless longitudinal and vertical wind variances show higher values in distorted sectors, while the lateral wind variance seems to be independent on the wind direction. Similar to level 1, the lateral wind component shows a more pronounced increase with stability than the longitudinal and vertical variances. The dimensionless vertical wind variance

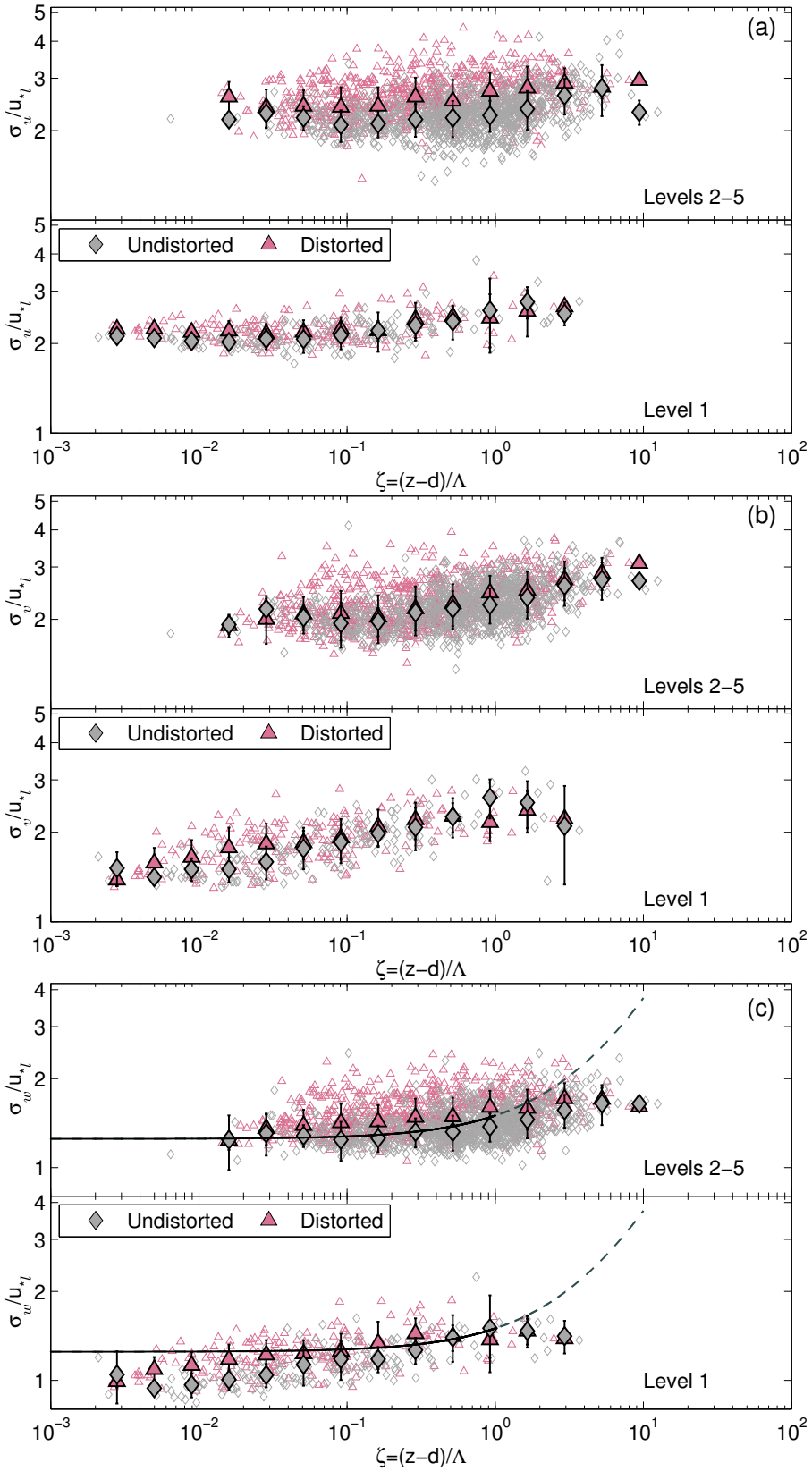

Figure 5.3: Scaled standard deviations of **(a)** longitudinal, **(b)** lateral and **(c)** vertical velocity fluctuations as functions of stability for level 1 (lower sub-panels) and levels $2-5$ (upper sub-panels) for distorted (pink triangles) and undistorted (gray diamonds) wind sectors. For further explanation see Fig. 5.1.

in undistorted sectors can be represented quite well with the similarity relationship valid for flat and homogeneous terrain (Kaimal and Finnigan 1994) in the stability range $0.01 < \zeta < 1$.

Based on modeled footprints particular wind sectors were related to corresponding surface types, accordingly. For undistorted wind directions $20 - 55$ deg and $85 - 175$ deg the underlying surface is associated with agricultural fields, while the $235 - 295$ deg sector corresponds to somewhat rougher but quite uniform surface covered mostly with the forest (Fig. 3.1). This implies that measurements at levels $2-5$ associated with undistorted sectors correspond to a layer which is in equilibrium with the underlying surface of more uniform roughness.

In the strongly stable regime (for $\zeta > 1$) the normalized variances show a tendency for a leveling-off, thus suggesting that z-less scaling might be appropriate. This implies that even for highly inhomogeneous terrain local scaling appears to be appropriate for all three velocity variances and that the local Obukhov length is relevant length scale. Additionally, in the strong stability limit the z-less scaling seems to be appropriate for longitudinal and vertical wind variances.

5.1.2 Subcritical and supercritical turbulence regimes

Grachev et al. (2013) showed that the inertial subrange, associated with the Richardson-Kolmogorov cascade, dies out when both the Ri and Rf exceed a critical value of approximately $0.20 - 0.25$, with $Rf_{cr} = 0.20 - 0.25$ being the primary threshold. They argued that a collapse of the inertial subrange is caused by the collapse of energy-containing/flux-carrying eddies. This leads to the invalidity of Kaimal's spectral and cospectral similarity (Kaimal 1973), and consequently, to violations of flux-profile and flux-variance similarity. Based on these results, Grachev et al. (2013) classified the traditional SBL into two major regimes: subcritical and supercritical. In the former ($Ri < Ri_{cr}$ and $Rf < Rf_{cr}$), a well defined inertial subrange is observed, turbulence statistics can be described by similarity theory and it is associated with so-called "Kolmogorov turbulence". The supercritical regime ($Ri > Ri_{cr}$ and $Rf > Rf_{cr}$) was characterized with the collapse of the inertial subrange and related to the small-scale, decaying turbulence, which they refer to as "non-Kolmogorov turbulence", and strong influence of the Earth's rotation even near the surface. Figure 5.4 shows the dependence of Rf (Eq. 2.8) on the local stability parameter at the measuring site. Dyer's parameterization (Dyer 1974) predicts an asymptotic limit to $Rf_{cr} = 0.2$ (solid black line), but this under-predicts Rf for higher stabilities for which Rf increases above $Rf_{cr} = 0.25$ (supercritical regime). The range of stability available for the analysis of the profile data is $0 < \zeta < 5$. For example, at levels 4 and 5, 40 % and 50 % of data points have $Rf >$

Rf_{cr}, respectively. Thus, higher levels, which correspond to higher stabilities, are characterized by small-scale turbulence.

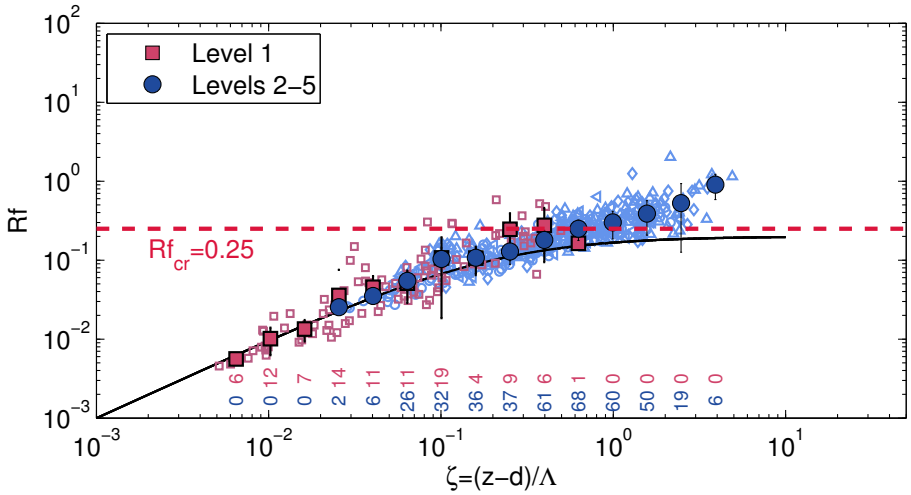

Figure 5.4: Stability dependence of the flux Richardson number for all five levels. Red squares and blue circles denote bin averages for the lowest level and for levels $2-5$, respectively. Error bars indicate one standard deviation within each bin. Number of data points inside each bin for the two subsets of the data is also given.

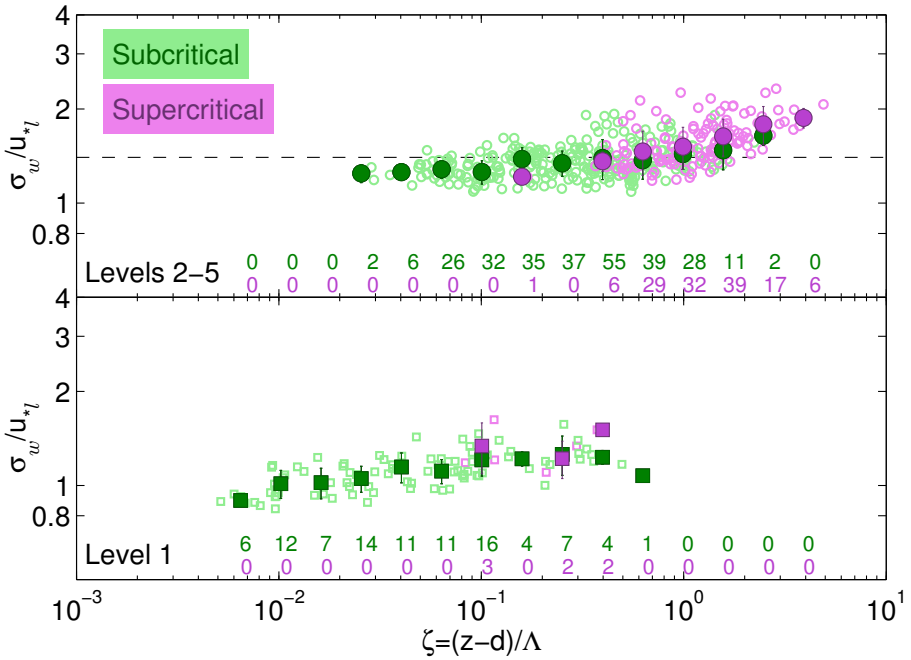

Figure 5.5: Scaled standard deviation of vertical velocity fluctuations as a function of stability. Data from the lowermost level (squares) and for levels $2-5$ (circles) in the subcritical (green) and supercritical (violet) regime are presented. The dashed line is equal to 1.4 which is the mean value of all data for levels $2-5$ in the subcritical regime. The number of data in each regime is indicated with the corresponding color.

Grachev et al. (2013) have found that $Rf_{cr} = 0.20$ was the primary threshold

for $\sigma_w/u_{*\ell}$. The normalized standard deviation of the vertical wind speed was reported to asymptotically approach to constant in the subcritical regime indicating consistency with z-less scaling in this regime. In the supercritical regime $\sigma_w/u_{*\ell}$ was monotonically increasing with increasing stability. The turbulence characteristics at present site (exemplified by the vertical velocity variance, Fig. 5.5) do not show a clear distinction between sub- and supercritical regimes as was found in Grachev et al. (2013) and for the non-dimensional vertical gradient of mean wind (Fig. 5.9). In the subcritical regime the number of data points at levels $2-5$ with $\zeta > 1$ is equal to 25 and is represented by only two bin averages. While Grachev et al. (2013) had a much broader range of stability in both regimes (they obtained z/Λ as small as 0.02 for the supercritical and up to 5 for the subcritical regime, respectively), in present dataset the results for these two regimes are almost indistinguishable (Fig. 5.5). Additionally, for the supercritical regime Grachev et al. (2013) observed an increase of $\sigma_w/u_{*\ell}$ in the range $3 < \zeta < 100$. For this regime an increasing tendency for the two highest levels is observed, but this is probably not significant because of the small number of data and restricted stability range (upper limit is $\zeta = 5$). Note that the number of data points here is much less compared to Figs. 5.1 and 5.3 because only 100 simultaneous 30-min intervals were available for the calculation of the Rf. Similar results are found for the horizontal wind variances (not shown).

5.2 Turbulent Kinetic Energy

Estimation of TKE is very important for atmospheric numerical modeling, since turbulent mixing is often parameterized using TKE. Here the TKE, defined as, $e = \frac{1}{2}(\overline{u'^2} + \overline{v'^2} + \overline{w'^2})$, which represents a TKE per unit mass (e.g. Stull 1988) is investigated. Fig. 5.6 shows e scaled by the u_*^2. In numerical models which use 1.5-order closure or TKE closure, TKE is predicted with a prognostic energy equation, and eddy viscosity is specified using the TKE and some length scale. Since TKE is essentially the sum of variances (divided by 2), according to Kansas values for neutral conditions (Kaimal and Finnigan 1994), the value of scaled TKE is equal to 5.48 for HHF terrain.

Over HHF terrain in Antarctica, Sanz Rodrigo and Anderson (2013) found that for neutral to moderate stabilities non-dimensional TKE is roughly constant up to $\zeta = 0.5$. Above this value, non-dimensional TKE grows until it reaches $\zeta = 10$ (corresponding to the ABL top), which is followed by an asymptotic value for stronger stabilities (Fig. 5.6, dashed black line, Eq. 5.1). They proposed a

simple empirical parameterization:

$$\frac{TKE}{u_{*\ell}^2}(\zeta) = \begin{cases} \frac{1}{\alpha_0} + b_E\zeta \;\;, \zeta \leq 10 \\ \frac{1}{\alpha_0} + b_E 10\,, \zeta > 10 \end{cases} \tag{5.1}$$

where $\alpha_0 = 0.22$ is the neutral limit value and $b_E = 0.5$.

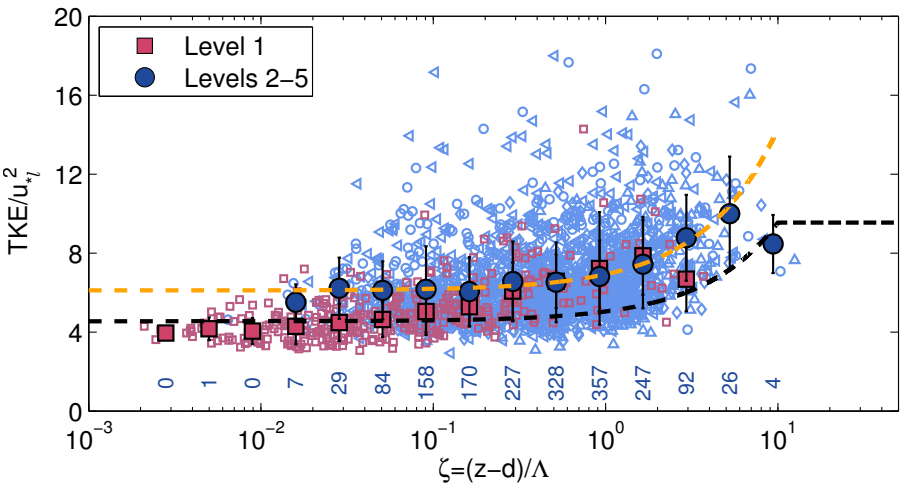

Figure 5.6: Dependence of non-dimensional turbulent kinetic energy on stability. The black dashed line is an empirical fit (Eq. 5.1). Individual data at each level are shown in background symbols, while red squares and blue circles represent bin-averages for the lowest and four higher levels, respectively. Error bars indicate one standard deviation within each bin. The number of data within each bin for levels $2-5$ is also indicated. The orange curve is a fit to present data (for levels $2-5$).

The above linear relation was fitted to present data from levels $2-5$ in the stability range $0.006 < \zeta < 8.30$ (Fig. 5.6, orange dashed line) using the least-squares method. Figure 5.6 shows a clear influence of the RSL on the lowest measurement level, which does not correspond to the proposed near-linear expression (5.1). The RSL influence also results in a reduced value of non-dimensional TKE for the neutral range ($TKE/u_{*\ell}^2 \approx 4.25$ based on values from Tab. 5.2) in comparison with the value of 4.5 found by Sanz Rodrigo and Anderson (2013). Their value is smaller than the reference value of 5.48 for HHF terrain probably due to higher air density in the Antarctica causing reduced values of $TKE/u_{*\ell}^2$ compared to mid-latitudes. We note that the relation of the type given by Eq. 5.1 fits the data for levels $2-5$ quite well (Fig. 5.6, orange dashed curve), but with slightly different coefficients $\alpha_0 = 0.16$, which corresponds to a neutral value of $TKE/u_{*\ell}^2 = 6.1$, and $b_E = 0.8$. The fitted neutral value of dimensionless TKE for levels $2-5$ is close to the value of 6.01, which is obtained based on values from Tab. 5.2.

Similar to wind variances, analysis of the TKE with respect to wind direction shows similar distinction between the distorted and undistorted sectors. While values of normalized TKE are similar for the two sectors at the lowest level, at levels

$2-5$ magnitudes of $TKE/u_{*\ell}^2$ in the distorted sectors are larger. The dependence of $TKE/u_{*\ell}^2$ on the stability parameter can be represented with a linear relationship, but the best fit coefficients are somewhat changed: $\alpha_0 = 0.19$ and 0.14 and $b_E = 0.97$ and 0.95 for undistorted and distorted sectors, respectively (not shown). The behavior of the normalized TKE in the sub- and supercritical regime was found to be consistent with the behavior of the normalized wind variances and no discernible difference between these two regimes was observed (not shown).

5.3 Correlation coefficients

In order to estimate fluxes from mean wind and temperature as input for dispersion models, it is useful to use turbulent correlation coefficients. These coefficients are a measure of the efficiency of turbulent transfer and are defined as

$$r_{uw} = \frac{\overline{u'w'}}{\sigma_u \sigma_w}, \tag{5.2}$$

$$-r_{wT} = -\frac{\overline{w'\theta_v'}}{\sigma_w \sigma_{\theta_v}}, \tag{5.3}$$

where r_{uw} and $-r_{wT}$ are correlation coefficients for momentum and heat transfer, respectively. Figure 5.7 shows momentum and heat flux correlation coefficients estimated for the lowest and the four higher measurement levels. For strong stratification smaller values of the correlation coefficients for momentum were obtained, but they increase quite steeply while approaching neutral conditions. This was also observed in both an urban (e.g. Wood et al. 2010) and a rural dataset (e.g. Conangla et al. 2008). Additionally, r_{uw} exhibits the same behavior with respect to the stability when analyzed for different wind azimuths. The magnitude of the momentum correlation coefficient is larger for the undistorted sector compared to distorted in the stability range $0 < \zeta < 1$ in the whole measurement layer (not shown). The absolute value of stability-averaged momentum flux correlation coefficient values are between 0.23 and 0.46 at level 1 (Fig. 5.7 (a)) and a similar range was observed for undistorted $(0.22 - 0.51)$ and distorted $(0.25 - 0.45)$ wind sectors. These values are similar to those obtained by Marques Filho et al. (2008). For levels $2-5$, the values of r_{uw} are somewhat smaller compared to level 1 and are in the range $0.14 - 0.34$ (Fig. 5.7 (a)), and they are similar to those obtained for the distorted wind sectors: $0.16 - 0.31$ (not shown), which is in the range of values observed over generally rougher urban surfaces (Wood et al. 2010).

The correlation coefficient for heat exhibits larger values for $\zeta > 0.1$ for levels $2-5$, and it decreases while approaching neutral conditions. The correlation coefficient for heat is between 0.10 and 0.26, which is similar to values reported in other studies

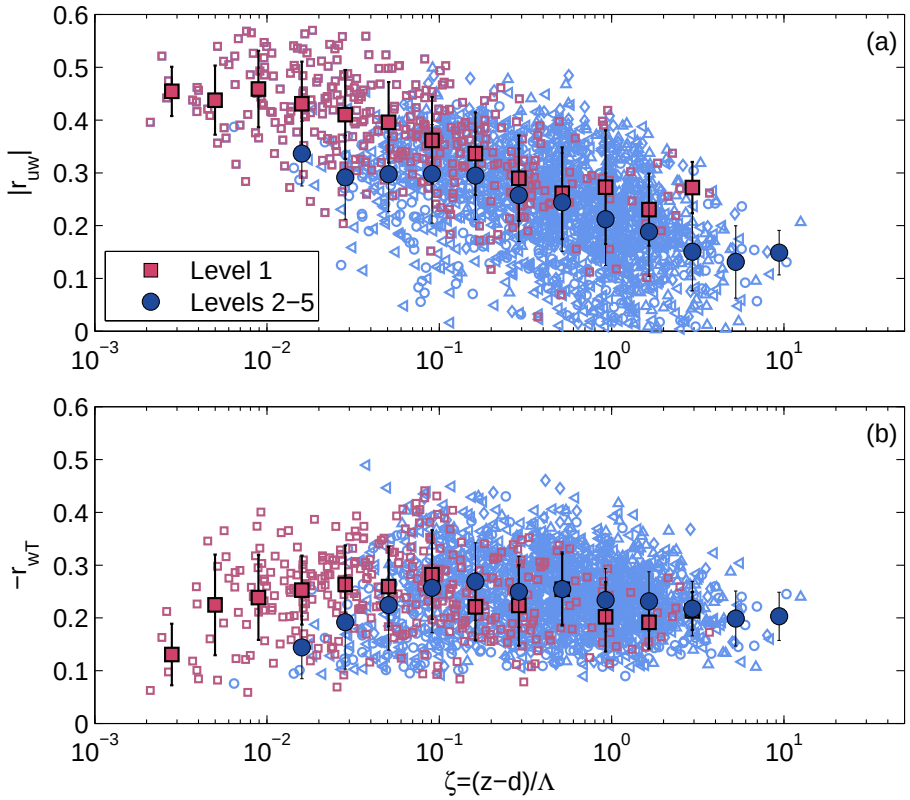

Figure 5.7: Momentum **(a)** and heat flux **(b)** correlation coefficients plotted as a function of stability. Background symbols represent individual data at each level while red squares and blue circles show bin-averages for the first level and for levels $2-5$, respectively. Error bars indicate one standard deviation corresponding to the particular bin.

(e.g. Heinemann 2004; Marques Filho et al. 2008; Wood et al. 2010). Additionally, no discernible dependence on wind direction was found for r_{wT} mostly due to the large scatter of the data (not shown). Mean values of the momentum and heat flux correlation coefficients over the entire measurement layer, and for all stabilities, are equal to 0.26 and 0.24, respectively. Also, no discernible difference in behavior of the momentum and heat flux correlation coefficients was observed between the sub- and supercritical regimes (not shown).

5.4 Flux-gradient similarity

I also investigated the relationship between mean vertical gradients and turbulent fluxes, also known as the flux-gradient relationships. Several interpolation methods were tested in order to determine the mean wind profile, and the second order polynomial fit was found to best fit the observed data. Thus, the vertical gradient of mean wind speed is obtained by fitting a second order polynomial through

the 30-min measured profiles

$$U(z) = p_1[ln(\frac{z-d}{z_0})]^2 + p_2 ln(\frac{z-d}{z_0}) + p_3 \tag{5.4}$$

and by evaluating a derivative with respect to z for each measurement level. The second order polynomial fit is widely used for measurements within the roughness sublayer (e.g. Rotach 1993; Dellwik and Jensen 2005) as well as within the inertial sublayer (e.g. Forrer and Rotach 1997; Grachev et al. 2013). Only about one hundred simultaneous 30-min intervals were available from each measurement level for the profile analysis. Results of the variance and TKE analyses showed different behavior of the first level in comparison with all the others. In order to investigate whether there is a difference in the flux-gradient relationship as well, the data from the first level and levels $2-5$ are presented separately (Fig. 5.8).

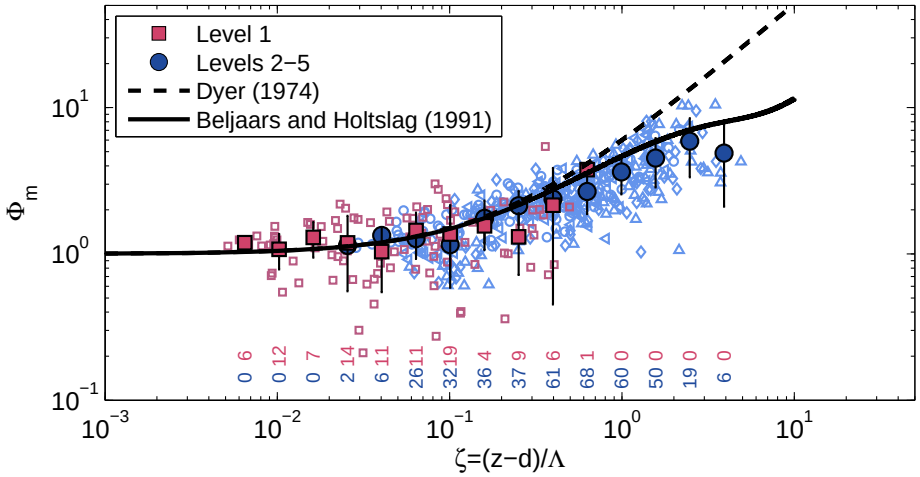

Figure 5.8: Non-dimensional vertical gradient of the wind speed plotted versus the local stability parameter. Individual data points for each level are shown by different markers (as in Fig. 5.1), while data from the lowest level are indicated with red color and from levels $2-5$ in blue color. Dashed line corresponds to the linear relationship of Dyer (1974) (Eq. 2.6) and the solid line is Beljaars and Holtslag (1991) relationship (Eq. 2.7). Bin averages for the lowest and four higher levels are included for easier interpretation of trends. Error bars indicate one standard deviation within each bin. Number of data points in each bin is also shown.

For present dataset no discernible difference of ϕ_m between level 1 and levels 25 can be observed. Almost all data at the first measurement level are within the stability range $z/\Lambda < 5$ and ϕ_m tends to a constant value of 1 when approaching near-neutral conditions. Quite diverse results concerning the value of ϕ_m in the RSL in the near-neutral conditions can be found in the literature. While in some studies of flux-gradient similarity within the forest RSL, m was found to be less than unity in the near-neutral range (e.g. Högström et al. 1989; Mölder et al. 1999; Raupach 1979; Thom et al. 1975), other studies indicate that ϕ_m is close to unity

(e.g. Bosveld 1997; Simpson et al. 1998; Dellwik and Jensen 2005; Nakamura and Mahrt 2001). Bosveld (1997) found that momentum and heat eddy diffusivities differ in magnitude in neutral conditions. This means that, with increasing canopy density, heat exchange remains enhanced in the RSL, whereas momentum exchange approaches surface-layer values. Dellwik and Jensen (2005) observed an increase of ϕ_m in the RSL in neutral conditions over fetch-limited deciduous forest due to the increased wind gradients directly above the canopy top. In previous studies reporting $\phi_m < 1$ and having mostly been conducted over pine forests (which compared to a closed deciduous forest have less biomass in the top of the canopy) the observed wind profile close to the three tops was less steep.

The previous sections have revealed clear differences in the flux-variance relationships between level 1 and levels 25 (i.e. the RSL and the transition layer, respectively) at the present site. In contrast, no significant difference is observed for the flux-gradient relationship. Similar results were reported by Katul et al. (1995) who pointed out that inhomogeneity in the RSL impacts variances but not necessarily fluxes. Following this line, results seem to indicate that surface characteristics at present site are influencing the strength of turbulent mixing and the wind gradient in the same way. This conclusion is additionally corroborated by the results of the analysis for different wind sectors as no dependence on the wind direction was found for the non-dimensional gradient of wind speed (not shown).

According to Fig. 5.8, ϕ_m increases more slowly with increasing stability than predicted by the linear approach (Eq. 2.6, dashed black line) and it appears to closely follow the Beljaars-Holtslag function (Eq. 2.7). The Beljaars-Holtslag formulation reduces the overestimation of the non-dimensional gradients for very stable conditions (Fig. 5.8, black solid line). Similar results were also obtained by other studies. For example, Mahrt (2007) found that ϕ_m increases linearly only up to $\zeta \approx 0.6$, while in the range $0.6 < \zeta < 1.0$ it increases more slowly than the linear prediction. However, according to Grachev et al. (2013) this result brings into question z-less scaling. Assuming that ϕ_m is a linear function of stability, gradients should tend to constant values for $\zeta >> 1$. Thus, the leveling-off of the ϕ_m at strong stabilities is an evidence for the breakdown of z-less stratification. Grachev et al. (2013) hypothesized that the leveling-off of ϕ_m functions for strong stability may be due to including data for which local similarity is not applicable.

Following the approach of Grachev et al. (2013), the prerequisite $Rf \leq Rf_{cr} = 0.25$ was imposed on all individual data at each level. According to Fig. 5.9, data with $Rf \leq 0.25$ almost perfectly follow the linear dependence on stability (according to Eq. 2.6) with the best-fit coefficient $b_m = 3.8$ (thin dashed line in Fig. 5.9). This implies the consistency of the data with the z-less prediction. The behavior of the non-dimensional gradient of wind speed in the supercritical regime in Fig. 5.9

exhibits a large deviation from the linear similarity prediction in the entire stability range. Moreover, supercritical data have a tendency to level-off. This suggests that the Beljaars-Holtslag non-linear expression (Eq. 2.7, Beljaars and Holtslag 1991), as well as results from other studies which exhibited leveling-off of similarity functions (e.g. Forrer and Rotach 1997; Baas et al. 2006; Grachev et al. 2007, 2013), were most likely affected by a large number of small-scale, non-Kolomogorov turbulence data.

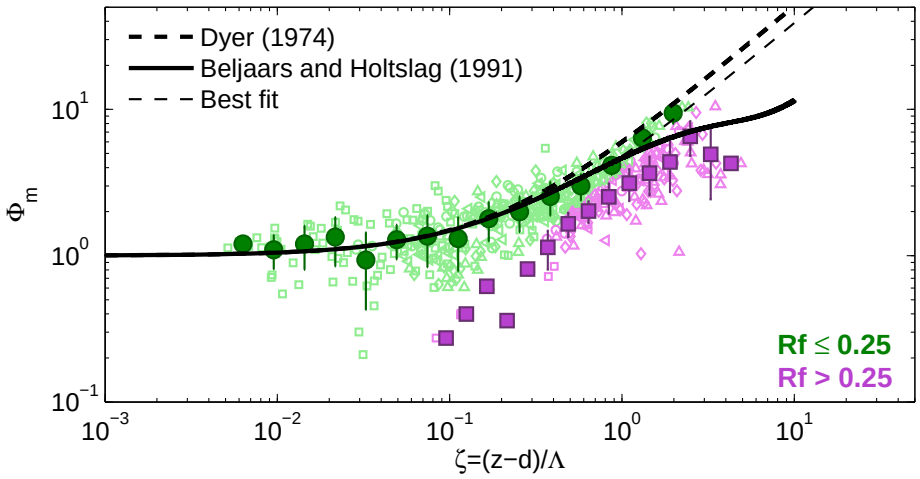

Figure 5.9: The non-dimensional vertical gradient of wind speed plotted versus stability for two different regimes; subcritical (Rf ≤0.25, green) and supercritical (Rf > 0.25, pink). Error bars indicate one standard deviation within each bin. Thick dashed line indicates the linear relationship 2.6 (Dyer 1974); the thin dashed line is the best fit to data for $Rf \leq 0.25$ (in the stability range $0.005 < \zeta < 2.43$), while the bold solid line corresponds to Eq. 2.7 (Beljaars and Holtslag 1991).

Ha et al. (2007) evaluated surface layer similarity theory for different wind regimes in the NBL based on the CASES-99 data. They concluded that although the stability parameter is inversely correlated to the mean wind speed, the speed of the large-scale flow has an independent role on the flux-gradient relationship. For strong and intermediate wind classes, they found that ϕ_m obeyed existing stability functions when z/L is < 1, while for weak mean wind and/or strong stability ($z/L > 1$) similarity theory broke down. Following on their approach, I evaluated the flux-gradient relationship separately for different wind regimes, which were classified based on the mean wind speed at each level similarly as in the study of Ha et al. (2007), and discriminated between subcritical and supercritical regimes. Strong wind regime is defined as $\overline{u}_i \geq \overline{\mathbf{U}} + 0.55\sigma$, intermediate regime is $\overline{\mathbf{U}} - 0.55\sigma \leq \overline{u}_i \leq \overline{\mathbf{U}} + 0.55\sigma$ and weak-wind regime is $\overline{u}_i \leq \overline{\mathbf{U}} - 0.55\sigma$, where $\overline{\mathbf{U}}$ is the mean wind speed averaged over all 30-min intervals at certain level, $\overline{u}_i$ is the mean wind speed of individual 30-min interval and σ is the standard deviation. In the weak wind regime the scatter is the largest, although significant scatter is observed also

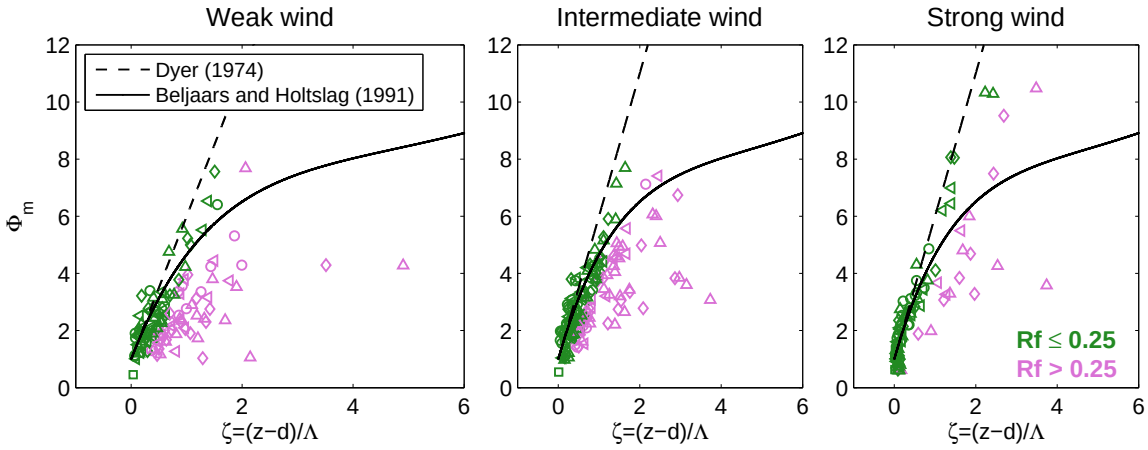

Figure 5.10: Non-dimensional vertical gradient of wind speed for each level plotted versus local stability parameter for weak-, intermediate- and strong wind regimes, respectively. Individual data points for each level are shown with the corresponding symbol. Data points exceeding critical value of $Rf_{cr} = 0.25$ (supercritical regime) are shown in pink. Dashed line indicates the linear relationship of Dyer (1974) (Eq. 2.6) and the solid line corresponds to the relationship 2.7 (Beljaars and Holtslag 1991).

for the intermediate and strong wind. For large ζ most of data points are bellow the Beljaars-Holtslag curve. These correspond to the small-scale turbulence in the supercritical regime (pink symbols on Fig. 5.10). Some near-neutral 30-min intervals occur with weak wind only at the lowest level. The striking difference of the behavior of ϕ_m with stability for different wind classes, which was found in the study of Ha et al. (2007), cannot be observed in present dataset (Fig. 5.10). In the weak wind regime the scatter is largest, although we note substantial scatter even for the intermediate and strong classes, caused by the small scale turbulence, which survived even in the supercritical regime (pink symbols). If we consider only data for $Rf \leq 0.25$, they follow Dyer's linear prediction even for the weak wind regime, indicating that similarity theory holds in this regime for the whole range of stabilities.

5.4.1 Estimating self-correlation

Monin-Obukhov as well as local similarity theory leads to self-correlation, because both predicted variables and the predictors are functions of the same input quantities (Hicks 1978). As an example, prediction of $\sigma_i/u_{*\ell}$ $(i = u, v, w)$ or ϕ_m in terms of the stability parameter ζ contains self-correlation since both $\sigma_i/u_{*\ell}$ or ϕ_m and ζ depend on $u_{*\ell}$. To test the role of self-correlation in present dataset, I followed the approach of Mahrt et al. (2003) as described in Klipp and Mahrt (2004), using 1000 random samples. Random datasets were created by redistributing the values of σ_u, σ_v, σ_w, $u_{*\ell}$, $\overline{w'\theta'_v}$ and dU/dz from the original dataset for each measurement level. I used threshold values $-\overline{w'\theta'_v} > 0.001$ mKs^{-1} and $dU/dz > 0.001$ s^{-1}, as val-

ues less than these are indistinguishable from zero. Random dataset had as many data points as the original one. This process was repeated 1000 times and corresponding 1000 random linear-correlation coefficients between σ_i and ζ and ϕ_m and ζ were calculated. The average of these 1000 random correlation coefficients, $\langle R_{rand} \rangle$, is a measure of self-correlation because random data no longer have any physical meaning. The difference between the squared correlation coefficient of the original dataset R^2_{data} and $\langle R^2_{rand} \rangle$ is proposed as a measure of the actual fraction of variance attributed to the physical process. A very small value of the linear-correlation coefficient (≤ 0.15) indicates no correlation between compared variables. Mahrt (2014) stated that physical interpretation of results becomes ambiguous when the self-correlation is of the same sign as the expected physical correlation. However, this test does not seem to be appropriate for near-neutral and very stable cases (z-less limit), since σ_i/u_* and ϕ_m tend to constant values, resulting in small (or even negative) correlation coefficients (Babić et al. 2016b).

Table 5.3: Self-correlation analysis. R_{data} is a linear correlation coefficient between ϕ_m and ζ for the original data at each level. $\langle R_{rand} \rangle$ is the self-correlation and it is the average of the correlation coefficients for 1000 random datasets. $R^2_{data} - \langle R^2_{rand} \rangle$ is a measure of the true physical variance explained by the linear model as proposed by Klipp and Mahrt (2004). Standard deviations are also indicated. N is the number of 30-min intervals.

Subcritical	N	R_{data}	$\langle R_{rand} \rangle$	$\sigma(R_{rand})$	$R^2_{data} - \langle R^2_{rand} \rangle$	$\sigma(R^2_{data} - R^2_{rand})$
Level 1	93	0.54	0.51	0.14	0.01	0.14
Level 2	83	0.91	0.55	0.11	0.50	0.12
Level 3	78	0.95	0.49	0.11	0.64	0.11
Level 4	60	0.73	0.49	0.13	0.28	0.13
Level 5	52	0.97	0.49	0.14	0.68	0.13
Supercritical						
Level 1	7	0.91	0.68	0.22	0.33	0.25
Level 2	17	0.91	0.51	0.18	0.54	0.18
Level 3	22	0.92	0.55	0.18	0.51	0.19
Level 4	39	0.66	0.43	0.15	0.22	0.13
Level 5	48	0.57	0.41	0.14	0.14	0.12

Since the present data exhibit different behavior for the subcritical and supercritical regimes, the self-correlation analysis was performed separately for each of these regimes. Linear correlation coefficients between ϕ_m and ζ for the original data and random data sets were calculated for each level. Table 5.3 shows the impact of self-correlation on the dimensionless wind shear. Generally, results for both the sub- and supercritical regimes suggest a non-negligible but not decisive impact of self-correlation. There are, however, two exceptions. At the lowest level, the subcritical data mostly reflect the near-neutral range where large scatter of the data is present resulting in a relatively small correlation coefficient of 0.54. Hence the

self-correlation test, which is based on linear correlation, produces small correlations of similar magnitudes for both physical and random data. This in turn results in a very small value of $R^2_{data} - \langle R^2_{rand} \rangle$ which means that results of this test are not very conclusive. At level 5, the correlation coefficient is large in the subcritical regime and reduced in the supercritical due to the increased scatter of the data for $\zeta > 1.5$ in this regime. Consequently, the value of $R^2_{data} - \langle R^2_{rand} \rangle$ is small. For the three middle levels, R_{data} has similar values in both the subcritical and supercritical regime, since in both regimes they exhibit a strong positive fit, i.e. ϕ_m increases with increasing stability with the larger scatter observed at level 4 (Fig. 5.9).

Grachev et al. (2013) proposed a new method which is not influenced by self-correlation and for which z-less scaling should also be valid. This new function represents a combination of universal functions and is thus a universal function itself. This new function, $\phi_m \phi_w^{-1} = \frac{k(z-d)}{\sigma_w} \frac{dU}{dz}$ plotted versus ζ is shown in Fig. 5.11. Grachev et al. (2013) defined this function as a product of Dyer's linear expression for ϕ_m and the inverse of ϕ_w

$$\phi_m \phi_w^{-1} = 0.75(1 + 5\zeta), \tag{5.5}$$

where the value of $\phi_w = 1.33$ corresponded to the median value in the subcritical regime (Fig. 5.11, gray solid line). For present data, the median ϕ_w value for levels $2 - 5$ was also found to be equal to 1.33 in the subcritical regime.

According to Fig. 5.11(a), the increase of the original data with stability is slower than the linear prediction (solid and dashed lines, respectively). Due to the fact that this new similarity function $\phi_m \phi_w^{-1}$ shares no variable with the stability parameter (except the reference height $z - d$), the observed decrease below the linear prediction is not caused by the effects of self-correlation. As seen from Fig. 5.11(b), this deviation from the linear relationship is mainly due to the small scale turbulence in the supercritical regime ($Rf > 0.25$). Additionally, this function is consistent with the z-less scaling when prerequisite $Rf \leq 0.25$ is imposed on the data (Fig. 5.11(b)). As already noted, the RSL shows more pronounced influence on σ_w profile compared to the wind shear profile, thus leading to an overestimation of Eq. 5.5 at level 1 while no systematic deviation can be observed for levels $2 - 5$ (Fig. 5.11). The scatter in the near-neutral range (at level 1) could be partly due to the wind direction inhomogeneities (not shown).

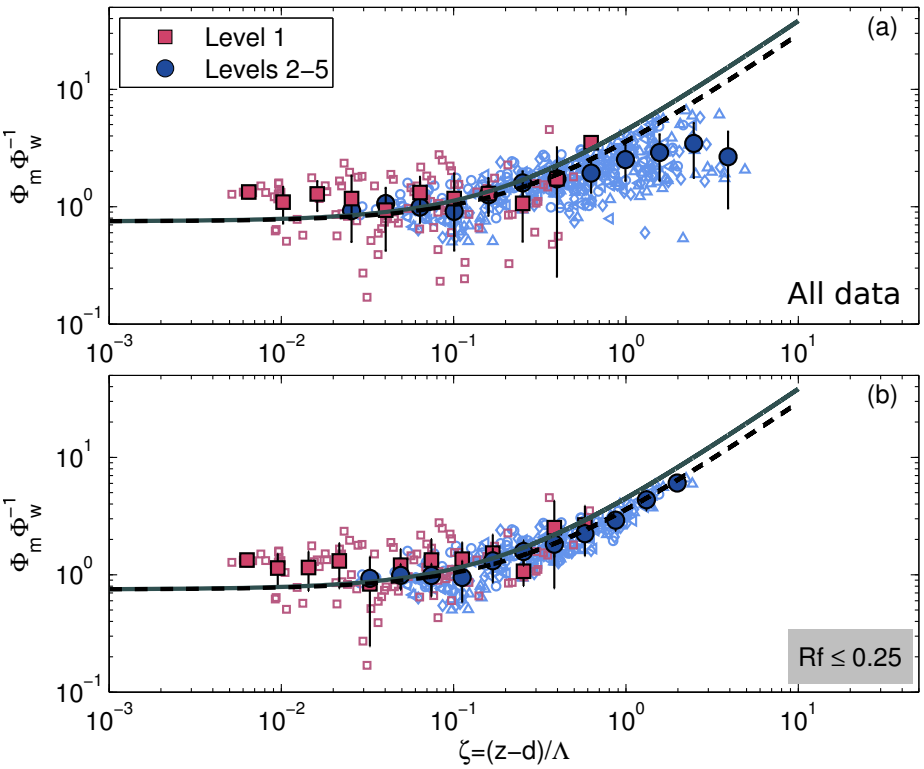

Figure 5.11: **(a)** The bin-averaged non-dimensional function $\phi_m \phi_w^{-1} = \frac{k(z-d)}{\sigma_w} \frac{dU}{dz}$, which is not influenced by self-correlation, plotted versus local stability. Individual data for each level are shown in the corresponding symbol as in Fig. 5.1. Bin averages for the lowest level (red squares) and four higher levels (blue circles) are included for easier interpretation of trends. Error bars indicate one standard deviation within each bin. Gray line corresponds to the experimental fit according to Grachev et al. (2013) ($\phi_m \phi_w^{-1} = 0.75(1+5\zeta)$) and the dashed black line is the best fit to Kutina data ($\phi_m \phi_w^{-1} = 0.75(1+3.8\zeta)$) in the subcritical regime. **(b)** Same as **(a)** but subject to the condition $Rf \leq 0.25$.

Chapter 6

Turbulence spectra, dissipation rate and budget of TKE

In the previous chapter, flux-variance and flux-gradient similarity was investigated within the framework of local similarity scaling. The results indicated that local scaling approach can be successfully applied for measurements over inhomogeneous surfaces. In this chapter, local similarity scaling is applied to investigate characteristics of turbulence spectra. Additionally, the dissipation rate and the budget of TKE within the RSL and transition layer are examined in this chapter.

6.1 Turbulence spectra

Previous results from field experiments, first of which were those of Kaimal et al. (1972), confirmed the applicability of the similarity laws to turbulence spectral densities. In the SL, spectral forms reduced to a set of universal curves that are functions only of ζ. Since most commonly used spectral models were derived over HHF terrain, the applicability of these models to spectra measured over inhomogeneous surface is investigated in this chapter. The influence of the RSL and transition layer on the turbulence spectral characteristics as well as appropriate scaling parameters needed to collapse spectra are considered here. Before presenting the results, the procedure used to calculate spectra and to deduce the dissipation rate of the TKE (ε) is described.

6.1.1 Spectral calculation

For each 30-min interval a linear trend was removed to avoid spurious amplification of lower frequencies. The spectra were calculated for each 30-min block applying a Fast Fourier Transform (FFT)[1] technique using Hamming windows. Each window

[1]Matlab function *pwelch* was used.

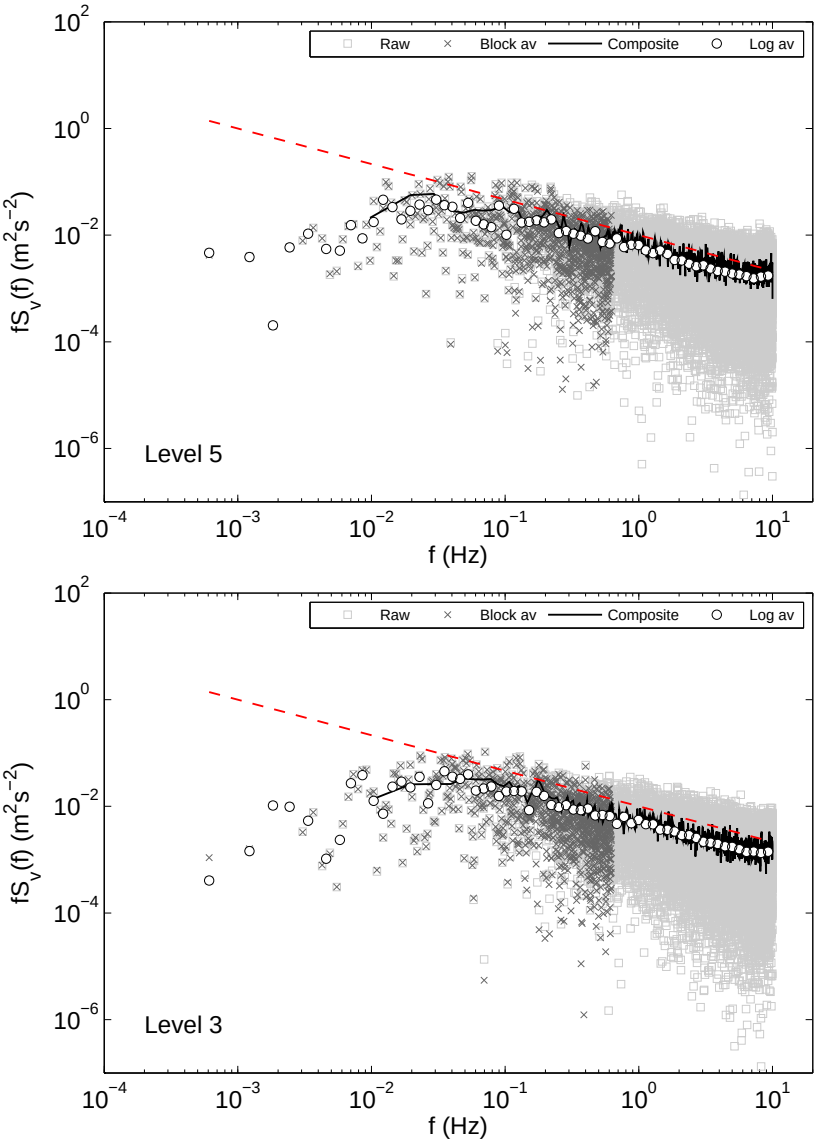

Figure 6.1: An example of the velocity spectra of the lateral wind component for two sonic anemometers (at $z = 40$ and 62 m) for the 30-min night period centered at 1845 LST 6 Feb, 2009. The raw spectra are shown with light gray squares, log averaged spectra are indicated with white circles, dark gray crosses show block-averaged spectra and black solid line represents the composite spectra. The red dashed line denotes the $-2/3$ slope.

contained 2^{15} data points which corresponds to the time period of 27.3 min (raw spectrum). This raw spectrum (light gray squares in Fig. 6.1) is unsatisfactory for the estimation of ε, so a log averaged spectrum was obtained by averaging the raw spectrum within each of 62 frequency bands (white circles in Fig. 6.1). Also, two additional spectra were calculated separately over low and high frequency bands. For the low frequency band, a block-averaged time series was created using a 16-point block-average to the original time series and the spectral estimate was computed after applying a 2048-point Hamming window to the block-averaged series (block-averaged spectrum, dark gray crosses in Fig. 6.1). This block-averaged spectrum

coincides with or is similar to the raw spectrum in the low-frequency range. For spectral estimates in the high frequency band, the original time series was divided into sixteen non-overlapping consecutive blocks. Each block contained 2048 data points. The spectrum was estimated for each block (using a 2048-point Hamming window) and finally 16 spectra were averaged to produce the composite spectrum (black solid line in Fig. 6.1). All these estimates are shown in Fig. 6.1 to illustrate the consistency of different variants of the same spectrum estimated for the v wind component.

6.1.2 Local isotropy

For the evaluation of ε the inertial dissipation technique was used. This method requires the existence of the inertial subrange in the Fourier velocity spectra. In the inertial subrange local isotropy should be present, in principle. The 4/3 ratio of the lateral and vertical to longitudinal velocity spectral densities is a stronger affirmation of local isotropy in the inertial subrange than the $-5/3$ slope. This ratio is shown in Fig. 6.2. Spectral ratios for each measurement level correspond to the median value. We note that the median lateral to longitudinal velocity component spectral density tends to converge towards a 4/3 value, which is expected from the theory, while the median S_w/S_u ratio is considerably less than 4/3. The ratio S_w/S_u smaller than 4/3 is in agreement with results of previous studies over forests (e.g. Liu et al. 2001; Su et al. 2004) or complex terrain (e.g. Roth et al. 2006; Christen et al. 2009; Večenaj et al. 2010, 2011), but it differs from those over smooth surface (Kaimal et al. 1972).

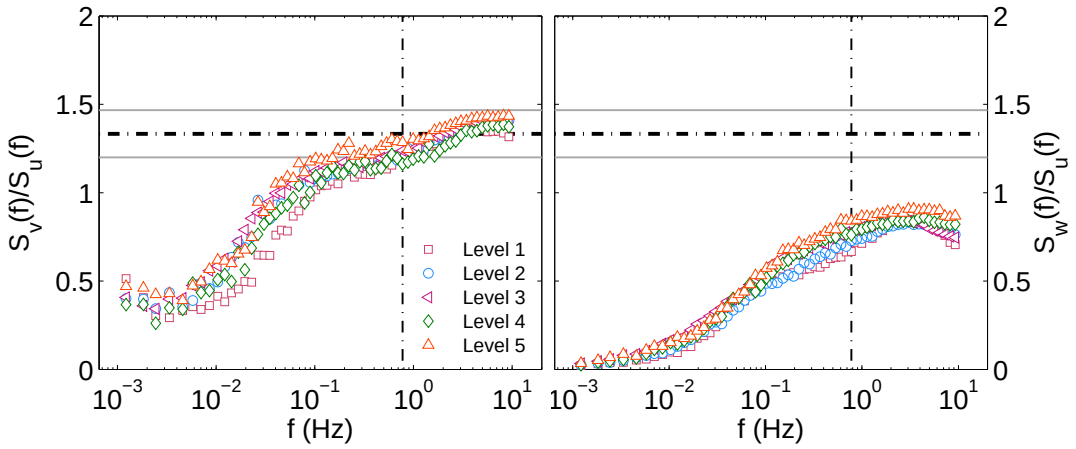

Figure 6.2: Ratio of the v and w to the u velocity spectral density at five measurement levels indicating the approach to the 4/3 ratio (dash-dotted line) in the inertial subrange as required by local isotropy. Gray solid lines indicate ±10 % deviation from 4/3.

Biltoft (2001) discusses a number of possible reasons for the discrepancy between the 4/3 velocity spectra ratio expected from theory and measurements. These include shear and buoyancy induced anisotropy in the inertial subrange which introduce considerable scatter in the lateral to longitudinal ratios of spectra. Another possible cause could be the consequence of the spectral processing methods. This is related to the spectral averaging time which is large compared to the inertial subrange eddy correlation decay time (which is on the order of a second). Chamecki and Dias (2004) tested the applicability of the local isotropy hypothesis to surface-layer measurements. They concluded that currently available sonic anemometers are unable to resolve the full inertial subrange of the velocity spectra. Thus, for most of their runs the isotropic values of S_w/S_u never reached the inertial subrange. On the other hand, the S_v/S_u ratio was much closer to the isotropic 4/3 value and the same was found in the present dataset. Due to the fact that S_w/S_u ratio in the present dataset is also lower than 4/3 (and even lower than 1), the dissipation rate of the TKE is evaluated based only on u and v components.

6.1.3 The dissipation rate of the TKE

Estimation of the TKE dissipation rate

Kolmogorov has shown that the energy spectrum of the velocity components follows the $-5/3$ slope in the inertial subrange. In the frequency domain, if the spectrum of the streamwise velocity component shows the $-5/3$ behavior, ε is evaluated from Eq. 2.25 with the Kolmogorov constant α_u assumed to be 0.53 (e.g. Piper and Lundquist 2004; Večenaj et al. 2011). Taylor's frozen turbulence hypothesis was used to transform from wavenumber to frequency space, therefore the validity of this hypothesis was first tested for each 30-min interval ($\sigma_u/\overline{u} < 0.5$, Willis and Deardorff 1976). The dissipation rate was estimated only for those intervals which satisfied this condition. The retrieval algorithm for the estimation of ε is shown in a flow chart on Fig. 6.3. As a first step, spectral slopes of all three velocity components were calculated. Spectral slopes were calculated in the high frequency domain ($0.776 - 3.042$ Hz) in a similar way as in Grachev et al. (2013). Within this range, six individual overlapping slopes have been computed between 42nd and 48th, 43th and 49th, ... and 47th and 53rd spectral values. Based on the mean of these six values, taken to be the representative slope, ε was estimated for each of the velocity components separately. Due to the fact that the expected 4/3 ratio was not attained for S_w/S_u, estimated values of ε for the vertical component (ε_w) were smaller (underestimated) compared to the ε estimates based on the longitudinal velocity components (which were aligned along $1:1$ line when plotting ε_u vs ε_v). Only those 30-min intervals for which the spectral slope in the inertial subrange corresponded

to the theoretical $-5/3$ ($\pm 10\%$ deviation) slope were taken. In a second step, the ratio S_v/S_u was calculated, where a threshold $\pm 10\%$ deviation from the expected 4/3 value was allowed within the specified high frequency range. Finally, ε was evaluated as the mean value of ε_u and ε_v estimates only for those 30-min intervals which satisfied both criteria. The vertical component spectrum was not used as a criterion because for almost all of runs the ratio S_w/S_u was significantly less than 4/3 ratio predicted by the local isotropy (Fig. 6.2). The number of 30-min intervals available for the spectral analysis was 164, 183, 334, 99 and 203 for levels 1 to 5, respectively.

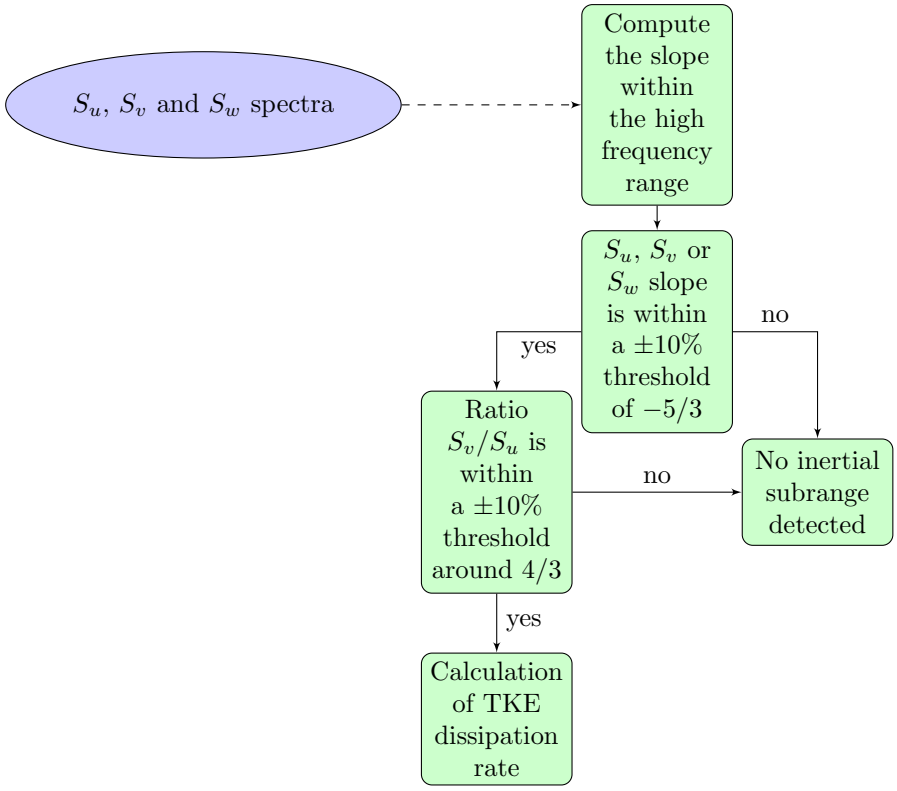

Figure 6.3: Schematic illustration of the retrieval algorithm used for the estimation of the TKE dissipation rate within the inertial subrange.

The non-dimensional dissipation rate of the TKE

The dependence of ϕ_ε on the stability parameter ζ is presented in Fig. 6.4. Gray symbols are values obtained based on the first criterion, the existence of $-5/3$ slope in the high frequency range. Violet symbols are the data points with an additional criterion imposed, indicating only those 30-min runs for which S_v/S_u ratio within the inertial subrange did not deviate more than 10 % from the theoretical 4/3 ratio. The 4/3 ratio between $S_v(f)$ and $S_u(f)$ is a stronger indicator of isotropy than the $-5/3$ Kolmogorov power law, since the $-5/3$ slope in the velocity spectrum can

occur even without the local isotropy (e.g. Champagne 1978; Grachev et al. 2014). With this criterion imposed the scatter is reduced and the data correspond better to the surface layer ϕ_ε functions given by Wyngaard and Coté (1971) (dashed curve) and Kaimal and Finnigan (1994) (solid curve, Fig. 6.4). Although the original data are scattered, the stability dependence is obvious. Figure 6.4 shows a less rapid increase of ϕ_ε close to the canopy top (level 1) than is observed in the stable SL over less rough surfaces. Near-neutral values of ϕ_ε are less than one indicating the RSL influence (Lee 1996). At upper levels, the ϕ_ε near-neutral values are larger than one, probably due to the IBL influence.

The functional form of the non-dimensional dissipation rate of the TKE can be derived on the basis of the dimensionless wind shear function ϕ_m. The relation of ϕ_ε to ϕ_m is obtained through the normalized TKE equation (Eq. 2.45) assuming that the sum of turbulence and pressure transport terms is negligible. In statically stable conditions within the SL ϕ_m usually has a linear form. Therefore, one might expect ϕ_ε to be a linear function of ζ as well (Eq. 2.30, Kaimal and Finnigan 1994), while Wyngaard and Coté (1971) proposed a non-linear relationship (Eq. 2.29). Results presented in Chapter 5 show that ϕ_m is a linear function of ζ only in the subcritical regime, while in general, data showed non-linear dependence on stability (Babić et al. 2016a). Figure 6.4 shows that a linear form of ϕ_ε can not adequately describe present data, and that the non-linear relation of Wyngaard and Coté (1971) would be a better choice. Therefore, the data were tested against the Wyngaard and Coté (1971) relation along with several modifications of this functional form to account the imbalance at neutral stability:

$$\phi_{\epsilon 1} = (1 + a\zeta^{3/5})^{3/2}, \tag{6.1}$$

$$\phi_{\epsilon 2} = b(1 + c\zeta^{3/5})^{3/2}, \tag{6.2}$$

$$\phi_{\epsilon 3} = (d + e\zeta^{3/5})^{3/2}. \tag{6.3}$$

The data were fitted in the stability range $0 < \zeta \leq 2$ since the Wyngaard and Coté (1971) fit was formulated for the same stability range. The best fit coefficient for each level and for each modified function are given in Table 6.1.

Best fit values for the coefficient a at the lowest level are substantially different (i.e. smaller) than the flat terrain reference of Wyngaard and Coté (1971), while upper levels show good correspondence with the values obtained in the surface layer over HHF surface (Table 6.1). Due to an apparent imbalance at neutral stability, the modified functions fitted the data better taking into account the deviation from unity at $\zeta = 0$. Estimated coefficients at neutral stability (i.e. b and d) at the lowest level are much smaller compared to the coefficients at higher levels. In Table

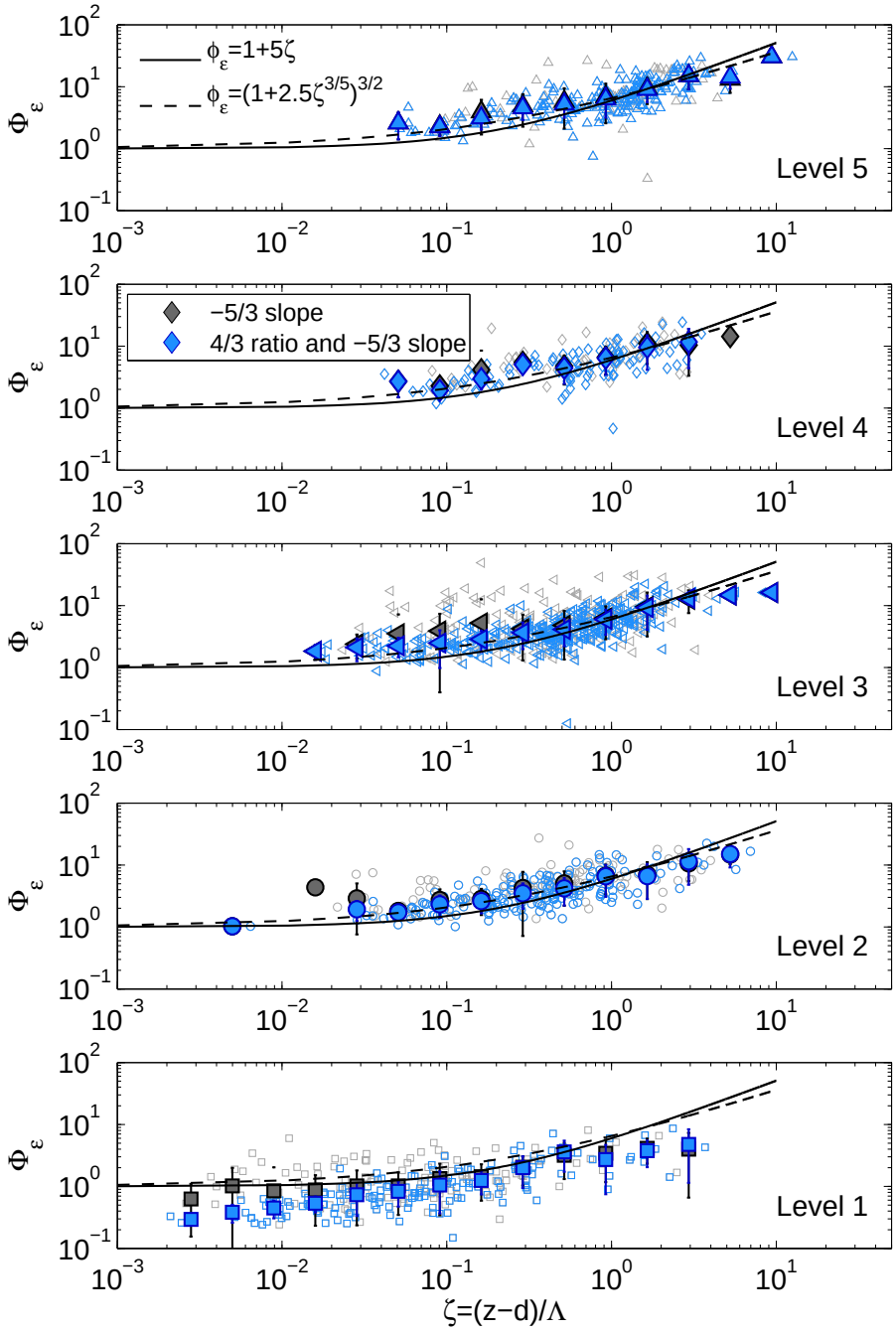

Figure 6.4: Non-dimensional dissipation rate of the TKE plotted versus ζ. Individual data at each level are shown as background symbols. Gray symbols indicate the data for which the estimated slope of best fit straight line was within ± 10 % of the theoretical $-5/3$ slope, while blue symbols denote data points for which additionally a 4/3 ratio (S_v/S_u) was found. Error bars indicate one standard deviation within each bin. The solid curve corresponds to the linear function according to Kaimal and Finnigan (1994) and dashed curve is an empirical fit given by Wyngaard and Coté (1971).

6.1 statistical measures of the best fit forms, namely the root mean square error ($RMSE$) and coefficient of determination (R^2), are given. These indicate that the data correspond better to the modified forms $\phi_{\varepsilon 2}$ and $\phi_{\varepsilon 3}$ since the $RMSE$ were on

Table 6.1: The best fit coefficients for different modifications of Wyngaard and Cote's (1971) function: $\phi_{\epsilon 1} = (1 + a\zeta^{3/5})^{3/2}$, $\phi_{\epsilon 2} = b(1 + c\zeta^{3/5})^{3/2}$ and $\phi_{\epsilon 3} = (d + e\zeta^{3/5})^{3/2}$. The root mean square error ($RMSE$) and coefficient of determination (R^2) of the best fit are also given. Numbers 1, 2 and 3 indicate corresponding ϕ_ε form.

	Level 1	Level 2	Level 3	Level 4	Level 5
a	0.92	2.38	2.42	2.47	2.53
b	0.54	1.40	1.19	1.35	1.85
c	2.40	1.69	2.11	1.90	1.39
d	0.58	1.21	1.19	1.25	1.47
e	1.68	2.09	2.20	2.20	2.06
$RMSE_1$	0.92	2.07	2.34	2.38	2.77
$RMSE_2$	0.83	2.05	2.35	2.37	2.73
$RMSE_3$	0.83	2.06	2.36	2.37	2.73
R_1^2	0.37	0.37	0.42	0.43	0.35
R_2^2	0.50	0.38	0.42	0.43	0.38
R_3^2	0.49	0.38	0.42	0.43	0.37

average smaller than for $\phi_{\varepsilon 1}$, while R^2 values also show that modified forms will fit the data slightly better. Additionally, values of $RMSE$ and R^2 suggest that $\phi_{\varepsilon 2}$ and $\phi_{\varepsilon 3}$ will fit the data equally well and these fits are practically indistinguishable, as seen in Fig. 6.5 for levels $2 - 5$.

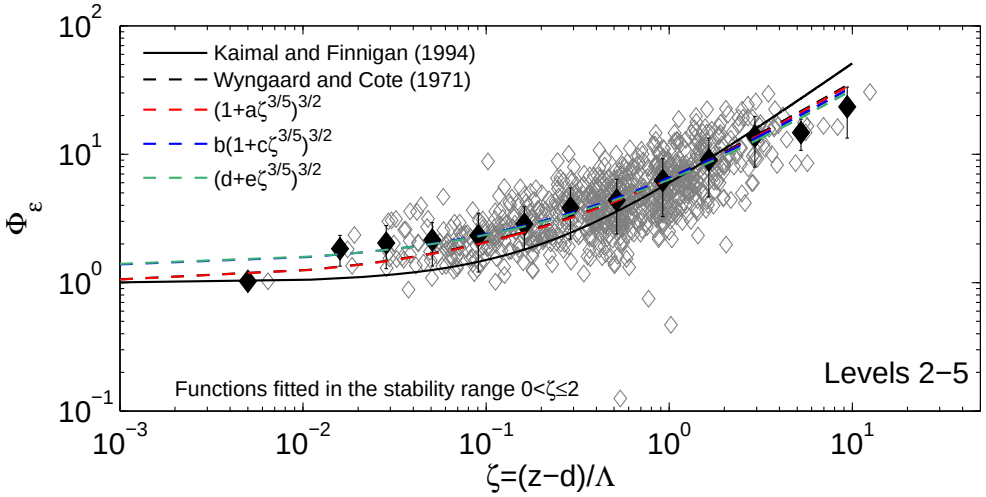

Figure 6.5: Non-dimensional dissipation rate of the TKE plotted versus the stability parameter for levels $2 - 5$. The best fit coefficients obtained by fitting $\phi_{\varepsilon 1}$, $\phi_{\varepsilon 2}$ and $\phi_{\varepsilon 3}$ functions to data from levels $2 - 5$ are: a=2.46, b=1.33, c=1.91, d=1.22 and e=2.21.

Since the non-linear dependence of the ϕ_m function on stability was caused by small-scale turbulence in the supercritical regime ($Rf > 0.25$), characteristics of ϕ_ε in sub- and supercritical regimes were also analyzed (Fig. 6.6). For ϕ_ε the deviation from the linear prediction was not caused by turbulence, which survived

in the supercritical regime, and no systematic difference between these two regimes is observed for ϕ_ε.

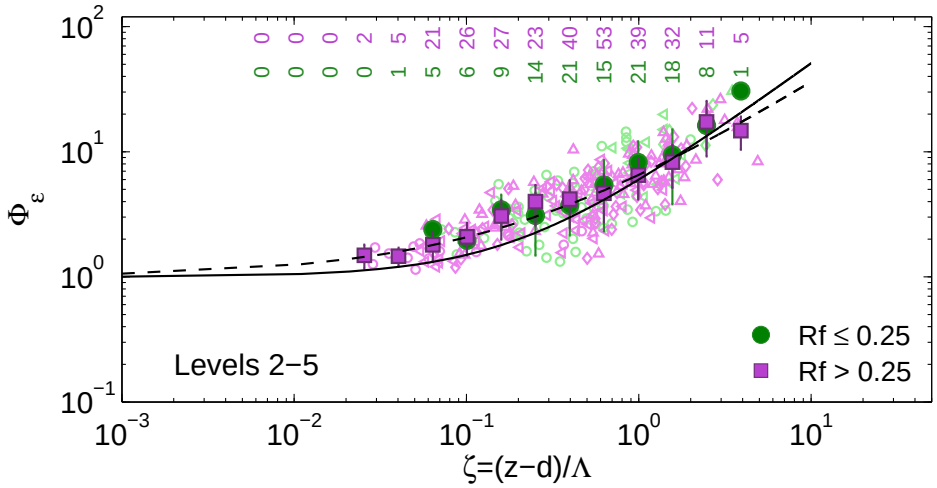

Figure 6.6: Non-dimensional dissipation rate of the TKE plotted versus the stability parameter for levels $2-5$ for subcritical (green) and supercritical (violet) regimes. Solid and dashed curves are the same as in Fig. 6.4. The number of data within each been is also indicated.

When using similarity relations, the self-correlation cannot be avoided (e.g. Hicks 1978; Klipp and Mahrt 2004; Hartogensis and De Bruin 2005) and this also applies to ϕ_ε where its non-linear dependence on stability could be due to self-correlation since the friction velocity is present in both variables (e.g. Fortuniak and Pawlak 2015). The estimate of self-correlation for the ϕ_m function was done in Section 5.4.1 using the approach proposed by Klipp and Mahrt (2004). The results showed that this test is not appropriate for near-neutral and strongly stable cases where the quantities converge to constant values. Besides that, it was shown for the $\phi_m\phi_w^{-1}$ function that self-correlation does not determine the shape of the function. For these reasons the test of self-correlation for ϕ_ε was not preformed. However, Hartogensis and De Bruin (2005) found that self-correlation only affects the scatter of ϕ_ε and not the shape. They have demonstrated that measured ε values determine the shape of ϕ_ε and not the shared u_*^{-3} term on both axes. However, because of the self-correlation errors in u_* affected the scatter in the $\phi_\varepsilon - \zeta$ plots. Errors in kinematic heat flux affected ζ resulting in scatter along the x-axis. Based on this discussion the self-correlation is considered as a source of uncertainty.

6.1.4 Characteristics of velocity spectra

According to Kolmogorov's theory for the inertial subrange, the one-dimensional velocity spectrum, normalized by the squared friction velocity can be expressed in

the form (2.28). Spectral densities of velocity components have been multiplied by f and normalized using only $u_{*\ell}^2$ (Fig. 6.7, left). The median velocity spectra exhibit a well-defined inertial subrange, with a $-2/3$ slope spanning over one decade for horizontal velocity components. The observed slope for vertical spectra is somewhat smaller than the expected $-2/3$ but it is within ± 20 % deviation limits from the theoretical slope (criteria used by e.g. Hartogensis and De Bruin 2005). However, local scaling above a forest using $u_{*\ell}$ and $z-d$ does not work properly (i.e. the curves do not collapse to a single curve) since the first observational level was placed within the RSL causing spectral peaks and the inertial subrange not to coincide at all levels (Fig. 6.7, left). A shift of spectral peaks to higher frequencies is evident as moving from the lowest to higher measurement levels. This shift of spectral maxima is a result of increasing stability with increasing height, where the median stability at level 1 was 0.06, i.e. close to neutral stability, and for levels $2-5$ is equal to 0.37, 0.49, 0.70 and 0.97, respectively. This is in agreement with results reported so far for measurements in the SBL, first of which by Kaimal et al. (1972) who showed the same stability dependence of spectral peaks for Kansas dataset.

Figure 6.7 (right) shows frequency-weighted spectra $fS_i(f)/\sigma_i^2$ $(i = u, v, w)$ plotted against the dimensionless frequency at $z/h_c = 1.1$, 1.8, 2.2, 3.1 and 3.4. When normalized using canopy scaling (i.e. the wind speed at the canopy top $U_{hc} = \langle \overline{u} \rangle_{hc}$ using measurements from the lowest level and the canopy height, h_c) as shown in Fig. 6.7(right), the spectra show a good collapse of spectral peaks as well as of the inertial subrange in the whole measurement layer. At the lowest measurement level the median spectrum of the u component exhibits a slight deviation from the $-2/3$ slope in the inertial subrange (indicated with the solid black line). The $fS_u(f)$ spectral peak is at the normalized frequency of 0.16, v component spectra peak at normalized frequency of 0.26. The vertical component spectra have the peak at $fh_c/U_{hc} = 0.51$. Similar values for u and w velocity components were found by Mammarella et al. (2008) for two deciduous forests, while they did not present results for v spectra. The success of the canopy scaling for spectral densities through the overall vertical measurement layer for the SBL is striking. Namely, the canopy scaling was reported to give a good collapse of spectral peaks and inertial subrange within the RSL (e.g. Raupach et al. 1986; Amiro 1990; Brunet et al. 1994). This is due to the fact that the RSL region is dominated by large coherent eddies which are generated at the canopy top (e.g. Finnigan and Shaw 2000; Shaw et al. 2006). These eddies have length scales proportional to h_c and are advected downwind with a velocity proportional to $\sim 1.8U_{hc}$ (Finnigan 1979). The fact that the canopy scaling works very well even within the transition layer suggests that these coherent eddies, which develop downwind of the forest edge, dominate the turbulence structure up to a significant height. The same was observed by Mammarella et al. (2008) for

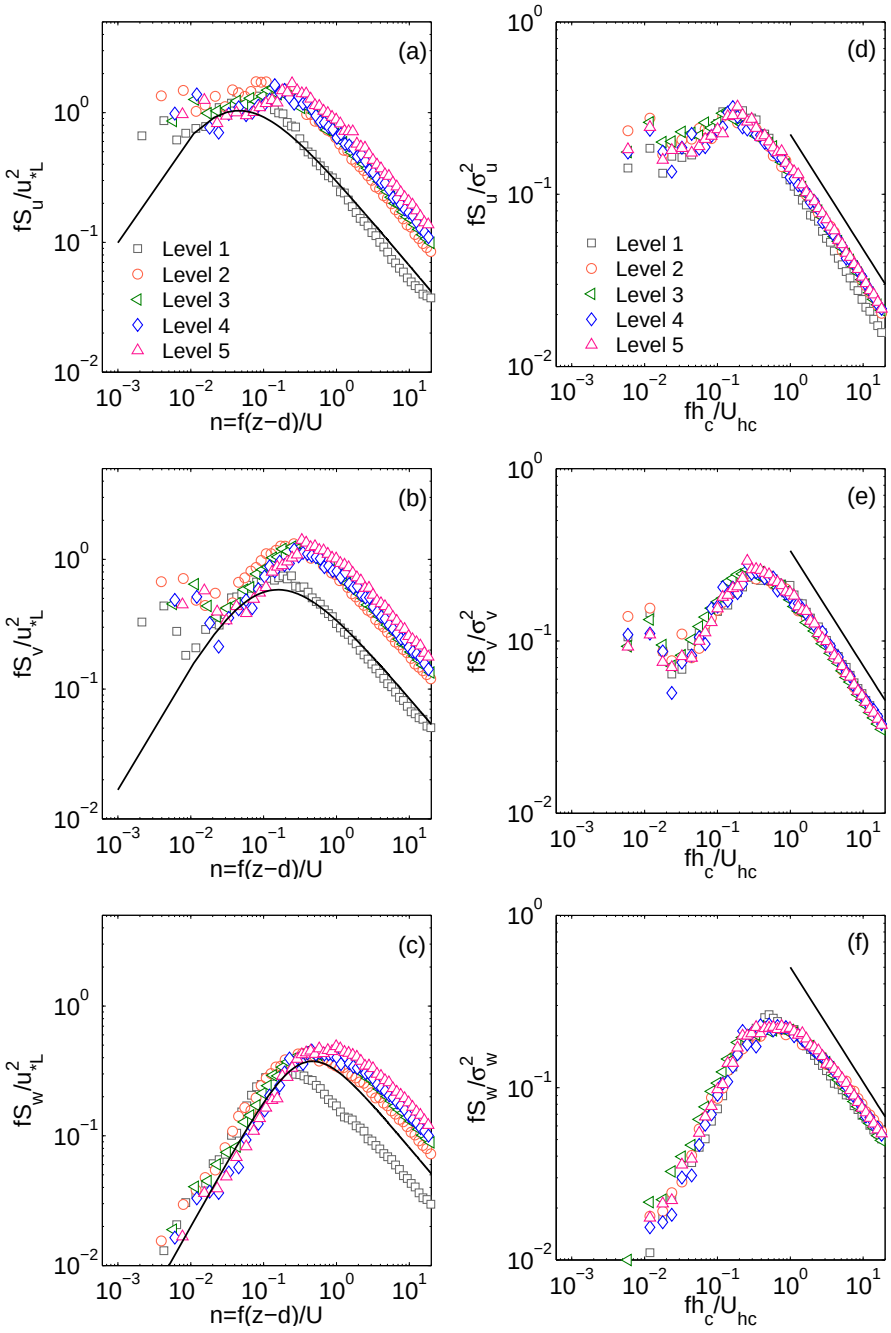

Figure 6.7: Normalized spectra of all three velocity components at all five levels (median of all spectra is shown) plotted versus non-dimensional frequency. *Left:* Frequency weighted spectra divided by the squared friction velocity. Solid black curve denotes Kansas neutral spectra (Eqs. 2.31−2.33). *Right:* Frequency weighted spectra divided by the squared standard deviation and plotted versus frequency normalized with canopy scaling (h_c and U_{hc}). Solid black line indicates $-2/3$ slope.

two different deciduous forest sites. While Mammarella et al. (2008) observed the influence of coherent eddies up to twice the forest hight, for the present dataset this influence is seen up to $3.4h_c$. The main difference from their study, which was

done for statically near-neutral conditions, is that here the success of the canopy scaling is obtained for the SBL, which to my knowledge has not been reported so far. Additionally, spectra examined in more detail showed a good collapse of the individual spectra from all five levels (in total 983 spectra) and not just of the median spectra (not shown).

Since it appears that traditional SL scaling variables are not appropriate for spectral scaling above the forest, frequency weighted spectra normalized by $u_{*\ell}^2$ against non-dimensional frequency fh_c/U_{hc} (Fig. 6.8, left) and normalized by σ_i^2 $(i = u, v, w)$ against non-dimensional frequency n (Fig. 6.8, right) were examined. Figure 6.8 shows a good collapse of spectra $fS_i/u_{*\ell}^2$ at levels $2-5$ when plotted against fh_c/U_{hc}. The spectra $fS_i/u_{*\ell}^2$ plotted against non-dimensional frequency (Fig. 6.8, right) do not show a collapse, thus indicating that the height above the ground and mean wind speed are not appropriate scaling variables for frequency to collapse the spectra. Based on these results, it seems that h_c and U_{hc} are appropriate scaling variables for the frequency. Figure 6.8 (left) shows a good collapse of spectra from levels $2-5$. In the analysis presented so far, it was demonstrated that measurements within the transition layer bear much similarity with the traditional IS, thus this last result suggests that the flow has reached equilibrium in this case. When using local friction velocity and the mean wind speed at the canopy top the stability dependence of spectral peaks at levels $2-5$ is removed. Comparison of Figs. 6.8 (left) and 6.7 (right) shows the different behavior of $\sigma_{u,v,w}/u_*$ within the RSL compared to the transition layer, as was shown in Chapter 5. Because $fS(f)$ plotted against frequency represents distribution of the variance, the velocity component spectra were observed to collapse to a single curve within the entire measurement layer when normalized with the appropriate variance.

Comparison with Kansas spectral models

Now we consider the spectra following the approach of Kaimal et al. (1972) who demonstrated spectral properties of the turbulent flow in the SL over HHF terrain. The spectra normalized by ϕ_ε as well as their behavior with respect to stability is examined. ε, estimated based on the horizontal wind components, is used in ϕ_ε, which is then used to normalize horizontal and vertical wind spectra. The analytical expressions given by Eqs. (2.31)–(2.33) (Kaimal et al. 1972) represent velocity spectra in the neutral limit $(0 < \zeta < 0.1)$ from the stable side and these are commonly used for comparison between different experimental and laboratory data. After normalizing each individual spectra with corresponding values of $u_{*\ell}^2$ and $\phi_\varepsilon^{2/3}$ for the respective run, the spectra from different levels show a good collapse in the inertial subrange for all three components, suggesting a wide credible inertial subrange (Fig. 6.9, left). Including these estimated $\phi_\varepsilon^{2/3}$ values (e.g. Fig.

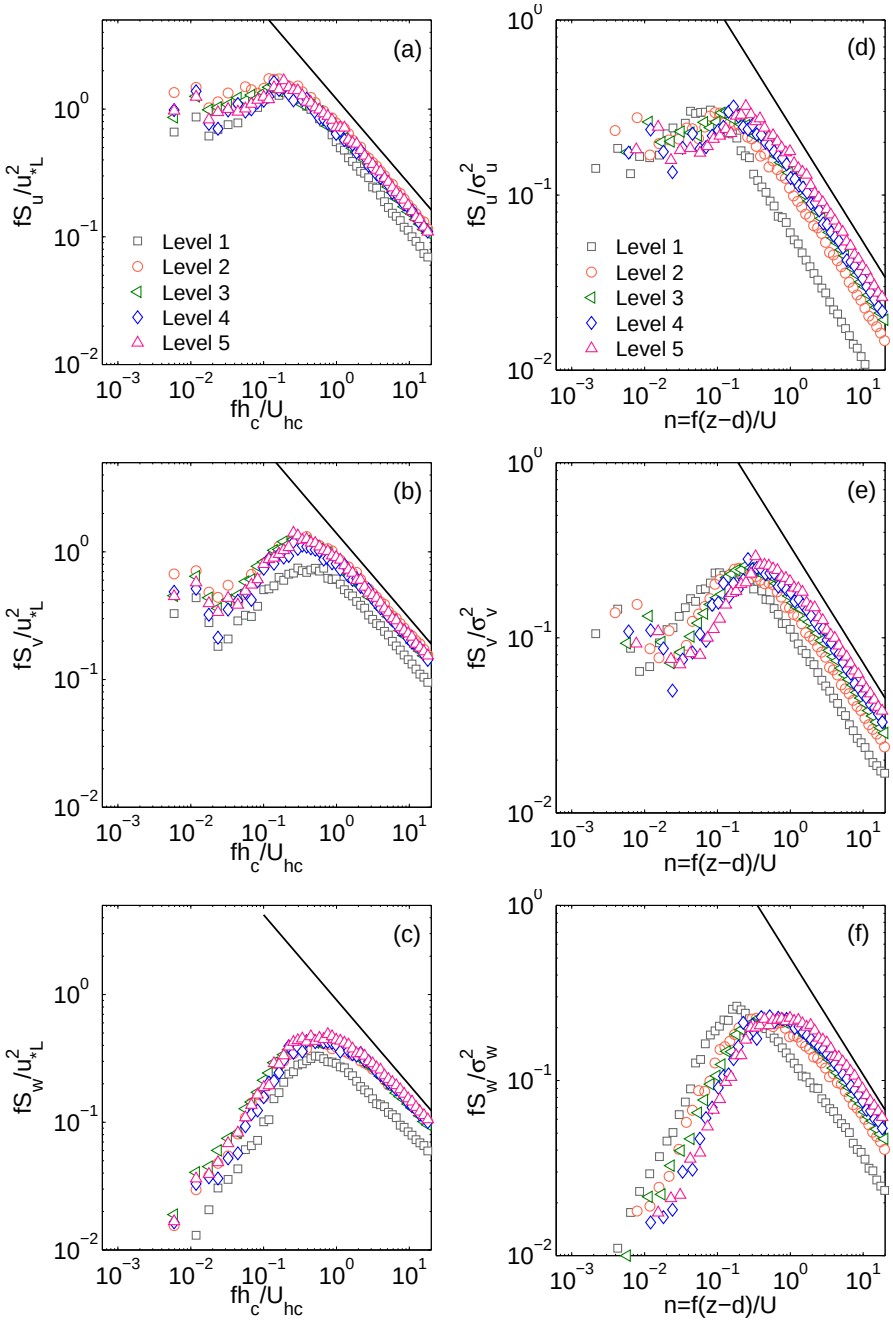

Figure 6.8: Normalized spectra of all three velocity components at all five levels (median of all spectra is plotted) versus frequency normalized with canopy scaling (h_c and U_{hc}). *Left:* Frequency weighted spectra divided by squared friction velocity. Solid black line denotes $-2/3$ slope. *Right:* Frequency weighted spectra divided by squared standard deviation and plotted versus non-dimensional frequency.

6.4) in the normalization of the velocity spectra in Fig. 6.9 (left), the dependence on the stability parameter compared to Fig. 6.7 (left) is removed in the inertial subrange and the spectra collapse to a single curve. At the lowest level, horizontal velocity spectra have larger peaks which are slightly shifted towards higher frequen-

cies compared to Kansas neutral spectra (Kaimal et al. 1972, Eqs. 2.31–2.33). At higher levels median spectral peaks are shifted to higher frequencies. This shift towards higher frequencies with increasing observational height is a consequence of larger static stability with increasing level (e.g. the median ζ is equal to 0.06, 0.37, 0.49, 0.70 and 0.97 for levels 1 to 5, respectively). The vertical velocity spectra show reduced magnitudes in the inertial subrange compared to the Kansas neutral spectra. The observed shift of the w spectra from the best fit curve for the HHF terrain is due to the normalization with ϕ_ε which was determined from ε_u and ε_v. Namely, ε estimates from u and v components were larger than those of ε_w, thus causing the reduced spectral values when used in the normalization of the vertical spectra. Besides that, the spectral peak of S_w at first level is shifted towards lower frequencies implying larger eddies compared to those for the flat terrain conditions.

Table 6.2: Number of 30-min runs (N) used in calculation of the median spectra and median value of the stability parameter (ζ_m) within each stability class (SC).

		Level 1		Levels $2-5$	
SC	Stability range	N	ζ_m	N	ζ_m
s1	$0 < \zeta \leq 0.05$	75	0.02	30	0.04
s2	$0.05 < \zeta \leq 0.15$	42	0.08	107	0.10
s3	$0.15 < \zeta \leq 0.35$	24	0.26	132	0.23
s4	$0.35 < \zeta \leq 0.65$	10	0.47	197	0.49
s5	$0.65 < \zeta \leq 1$	5	0.95	124	0.85
s6	$1 < \zeta \leq 1.5$	2	1.30	114	1.22
s7	$\zeta \geq 1.5$	6	2.05	115	2.06

Since level 1 is different than levels $2-5$, the stability dependence of velocity spectra is thus considered separately. The spectra from different levels within the transition layer are expected to collapse for a certain stability. The velocity components spectra, normalized by $u_{*\ell}^2$ and $\phi_\varepsilon^{2/3}$ are evaluated for 7 stability categories and the median spectra for each category are plotted in Fig. 6.9, right. The stability dependence of the spectra is shown for level 1 and levels $2-5$ separately. The number of cases and the median stability parameter for each category are listed in Table 6.2. These normalized spectra show that $-2/3$ slope is followed quite closely for a wide range of frequencies in the inertial subrange for horizontal velocity components. For the vertical component, the inertial subrange is observed to be much narrower, with smaller slope which deviates $\pm 20\%$ from the theoretical $-2/3$ slope. The smaller spectral roll-off in the inertial subrange was also observed in some studies over urban surfaces (e.g. Christen et al. 2009). Roth et al. (2006) attributed this to the extra physical processes, such as a wake production mechanism, which controls the conversion of the mean flow to turbulent energy. This produces additional eddies of different scales, which is related to and depends on the nature of

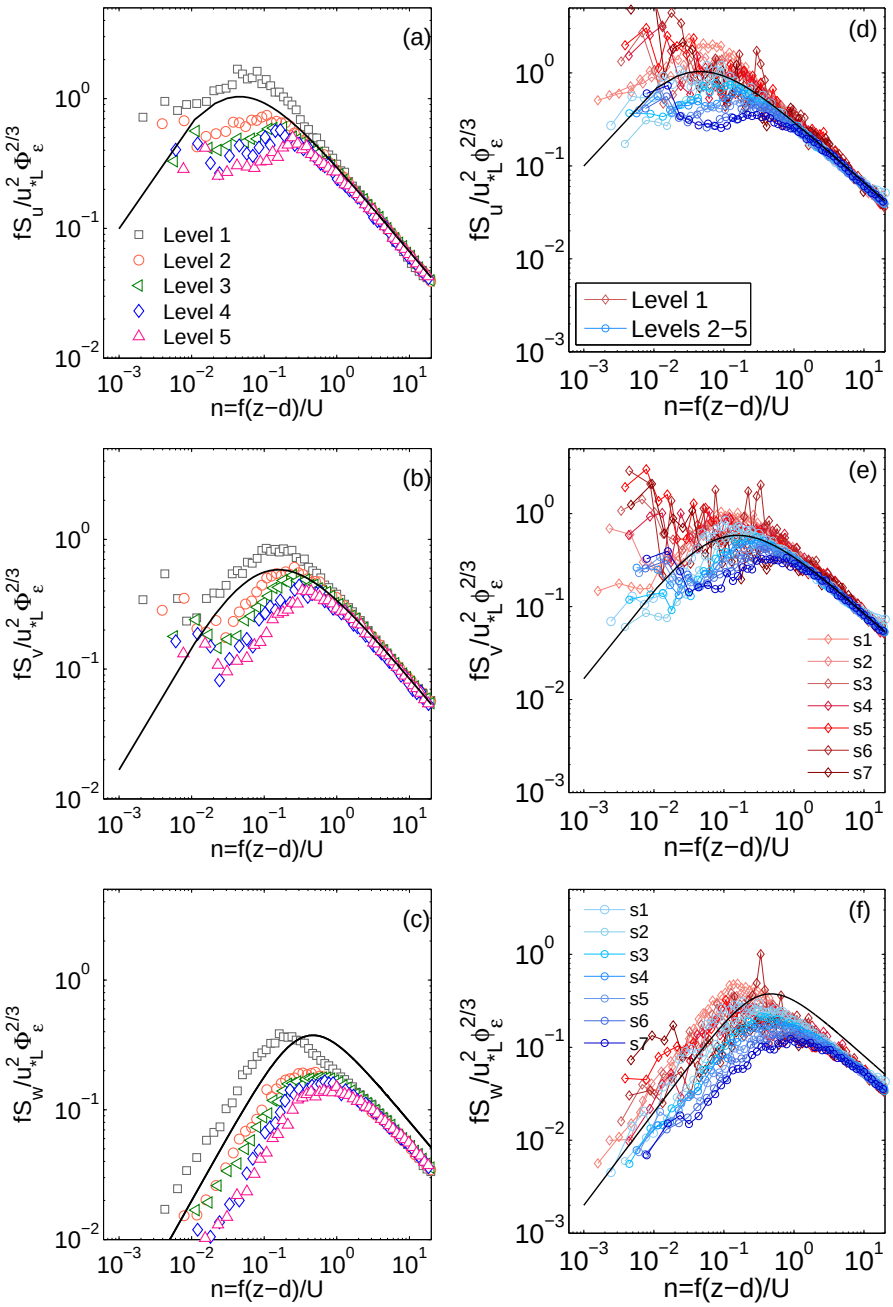

Figure 6.9: *Left:* Frequency weighted spectra of u, v and w divided by friction velocity and ϕ_ε (median of all spectra is plotted) for all five levels plotted versus non-dimensional frequency. *Right:* Normalized spectra for seven different stability categories (indicated as $s_1, s_2, \ldots, s_7$) defined as in Table. 6.2 plotted versus non-dimensional frequency. Red colors indicate median spectra at level 1, while blue colors indicate spectra from levels $2-5$ (darker colors denote stronger stability). Black solid curves correspond to neutral Kansas spectra (Kaimal et al. 1972).

the surface morphology. All velocity components show clear separation according to ζ, i.e. with increasing stability the intensity of the spectral peak is reduced and shifted to higher frequencies. We note that static stability has an important effect

on turbulence spectral structure and also on frequencies of spectral peaks (Fig. 6.9, right). The near-neutral (s1 class) median spectra of horizontal velocity components at levels $2-5$ show a good collapse and agreement in magnitude and the position of the spectral peak with the Kansas neutral spectra, while the same was not found for level 1.

The vertical velocity spectral magnitudes for most of the stability categories at level 1 and levels $2-5$ are about factor of two smaller compared to the Kansas neutral spectra. We assume this is due to the ϕ_ε function used for the normalization of the vertical spectra which was determined based on the horizontal ε estimates. Note that, S_w/S_u was found to be close to 0.85 and not 4/3 as required by strict local isotropy (Fig. 6.2), which means that S_w is smaller than what it should be compared to values for ideal surfaces. Therefore, for each individual spectrum ε_w was estimated, and consequently ϕ_{ε_w}, from the vertical spectra in the high-frequency range where the spectra exhibited $-5/3$ ($\pm$ 10 %) slope (Fig. 6.10). Corresponding individual ϕ_{ε_w} values were used for normalization of the vertical spectra (Fig 6.11). ε_w was estimated using Eq. 2.25 assuming the theoretically expected $\alpha_w = 4/3\alpha_u$.

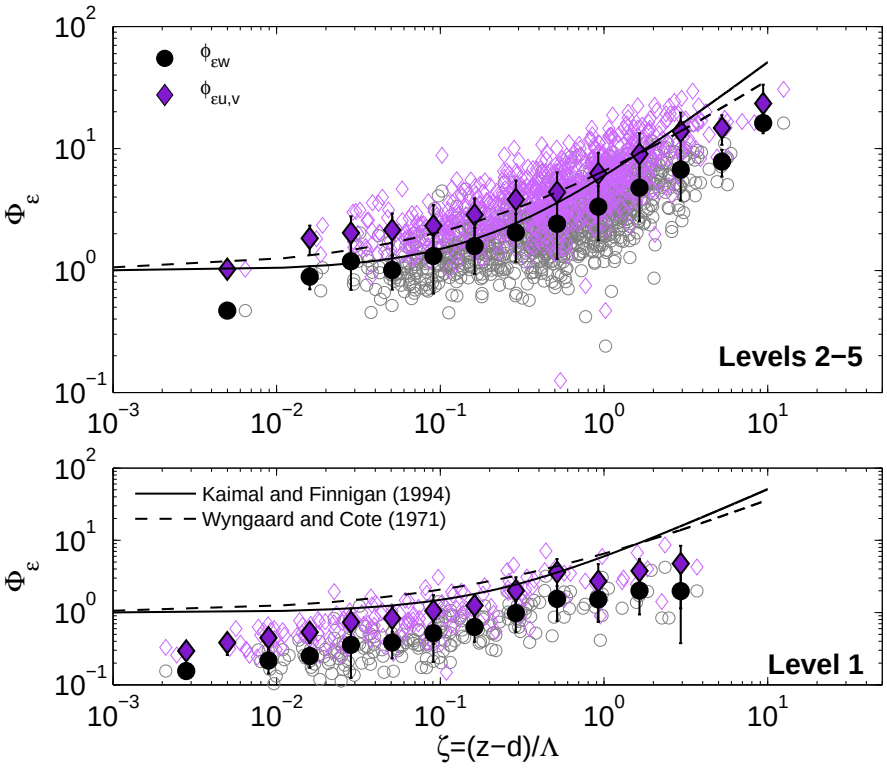

Figure 6.10: Different estimates of ϕ_ε plotted versus the stability parameter. Solid and dashed curves are the same as in Fig. 6.4.

Although for ideal HHF terrain the estimate of ε might not be very sensitive if estimated based on only u or all three wind components as was observed by Grachev et al. (2014), this was not the case for this heterogeneous site. As seen from Fig.

6.10, values of ϕ_{ε_w} are substantially lower compared to $\phi_{\varepsilon_{u,v}}$, but the two curves have similar shapes. The reduced spectral power in the vertical component (compared to horizontal components) is reflected in a smaller dissipation rate, meaning that ε is not isotropic. The lack of local isotropy in the vertical direction was observed in other studies over complex forest sites (e.g. Liu et al. 2001; Su et al. 2004), however, it has not been reported that this will have an influence on different estimates of ε for different velocity components. Consequently, when using ϕ_{ε_w} the overall form and the magnitude of scaled spectral densities are equal to the Kansas curves (Fig. 6.11). Therefore, due to the anisotropy of the flow at this complex site, the ε obtained from vertical velocity spectra can be used to normalize the spectra and good correspondence with the Kansas spectral model will be obtained in this case. This corresponds to Wyngaard's statement that local isotropy only, in fact, can be obtained in a truly homogeneous flow field (Wyngaard 2010), which generally is not the case in the vertical, but certainly less so over an inhomogeneous forest canopy. The fact that a good correspondence with Kaimal's spectral model can be obtained even for inhomogeneous surface has significant importance since the analytical forms of the spectral model are often used in practical applications, such as spectral dispersion models, or the flux corrections (Moore 1986). More importantly, this correspondence is obtained at a price that ε is different for horizontal and vertical components. This has implications on the corresponding budgets of the variances as well as for the TKE since in the TKE closure a conservation equation for ε assumes that it is the same in all three directions.

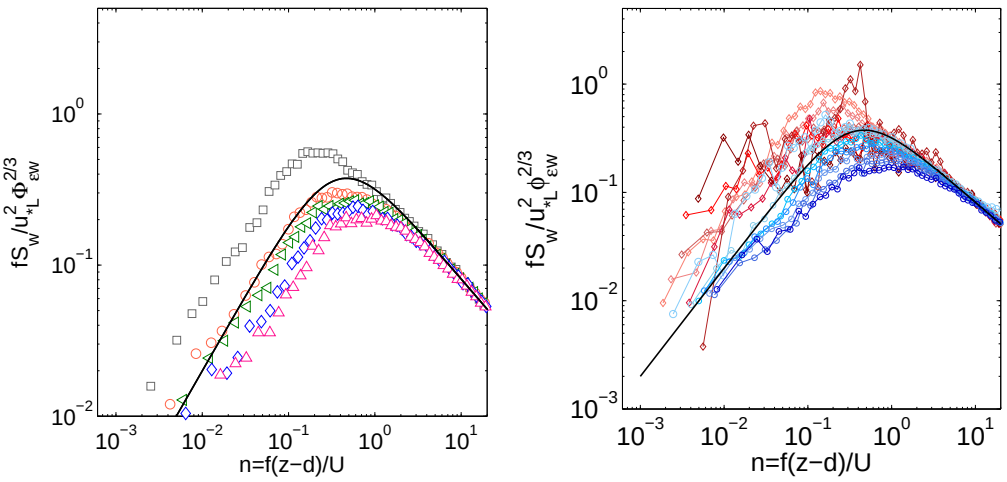

Figure 6.11: Vertical velocity spectra normalized by ϕ_{ε_w} for all five levels (*left*) and for seven different stability categories as defined in Table. 6.2 (*right*) (median of all spectra is plotted) plotted versus non-dimensional frequency. All the symbols are the same as in Fig. 6.9.

Analytical spectral models given by Eqs. (2.34) and (2.35) were tested in the

entire frequency range for the near-neutral data ($0 < \zeta \leq 0.05$), and the "blunt model" is found to be more appropriate for each wind component. This model is fitted to data in the layer above the RSL and the best fit coefficients are obtained by the least-squares method:

$$\frac{fS_u(f)}{u_{*\ell}^2} = \frac{105n}{(1+35n)^{5/3}}, \tag{6.4}$$

$$\frac{fS_v(f)}{u_{*\ell}^2} = \frac{21n}{(1+10.6n)^{5/3}}, \tag{6.5}$$

$$\frac{fS_w(f)}{u_{*\ell}^2} = \frac{6.5n}{(1+5.2n)^{5/3}}. \tag{6.6}$$

The obtained best-fit coefficient values for levels $2-5$ are in good agreement with Kansas values (Eqs. 2.31– 2.33) obtained within SL over HHF terrain. For the most stable classes the influence of sub-meso motions becomes evident in the spectra at lower frequencies where spectra have different slope (Fig. 6.9).

As a scaling approach for the SBL spectra, a model proposed by Olesen et al. (1984) can be used. This model is based on the assumption that the non-dimensional frequency at the maximum of the spectral curve is a function of ζ; thus, all spectral maxima should coincide if spectral density is plotted as a function of n/ϕ_m. Their model for the stable SL spectra is represented with Eqs. (2.41) – (2.43). In order to normalize spectra with ϕ_m and ϕ_ε, Olesen et al. (1984) used parameterizations proposed by Businger et al. (1971) for ϕ_m and Kaimal et al. (1972) for ϕ_ε. Contrary to this, the individual values of ϕ_m and ϕ_ε estimated for the present dataset were used and discussed above instead of parameterizations. This approach can also be extended to the local scaling regime by using local values of the u_* and ζ (Forrer 1999). Figures 6.12 and 6.13 show spectral curves (individual and median) of all three velocity components from each of five measurement levels. Considering the above findings regarding the vertical velocity spectra, here ϕ_{ε_w} is used to normalize w-component spectra.

The individual spectra show the actual scatter of the data and the median spectra are compared to the Olesen model for HHF terrain (dashed black lines in Figs. 6.12 and 6.13). Quite good agreement with Olesen model can be observed for all three velocity components. It is found that, as predicted by the Olesen's model, the spectral curves from five different levels on a tower (Figs. 6.12 and 6.13) and for different stability classes (Fig. 6.14) closely collapse to one curve. Fitting this model to the data at levels $2-5$ the following expressions (parameterizations) were

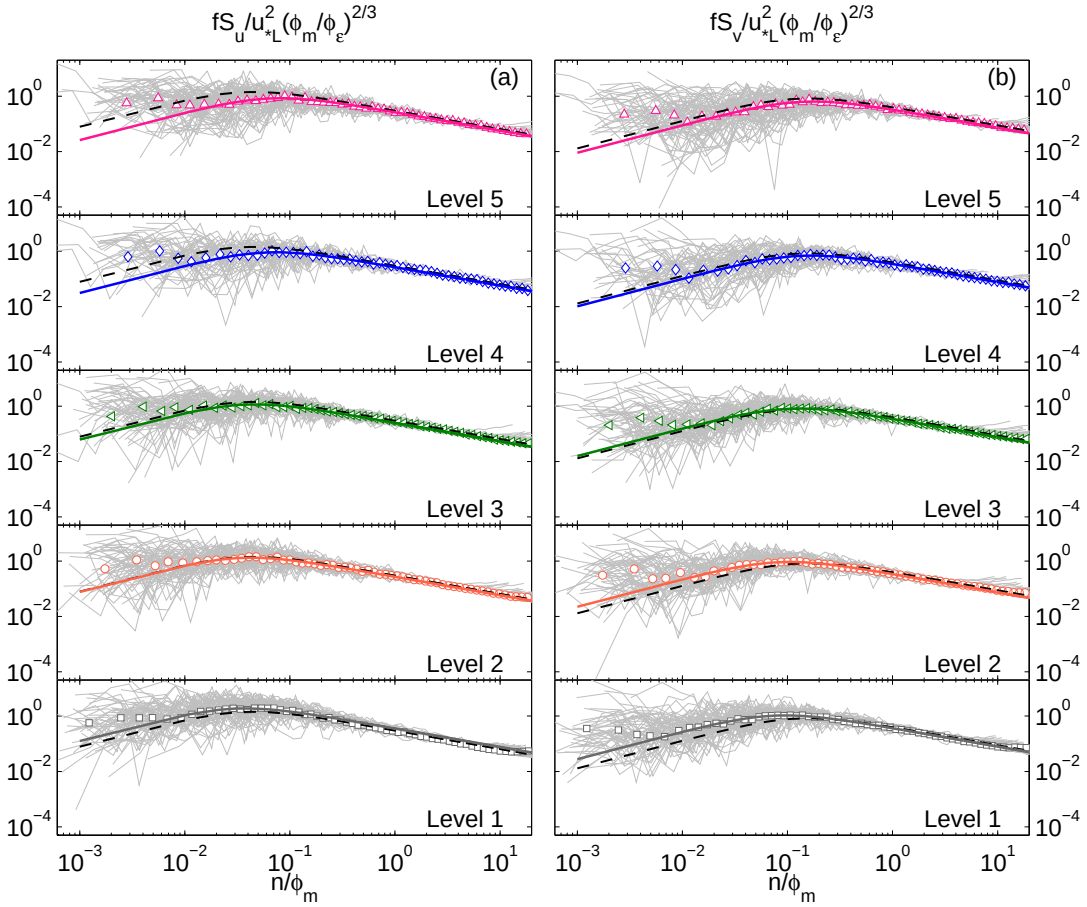

Figure 6.12: Normalized spectra of longitudinal (**a**) and lateral (**b**) velocity component for each measurement level. Gray lines show individual spectra and colored symbols indicate the median spectrum. The dashed black line corresponds to Eqs. (2.41) and (2.42) and solid colored lines indicate the best fit for each level.

obtained:

$$\frac{fS_u(f)}{u_{*\ell}^2} = \frac{49n/\phi_m}{1+190\,(n/\phi_m)^{5/3}}\left(\frac{\phi_\varepsilon}{\phi_m}\right)^{2/3}, \tag{6.7}$$

$$\frac{fS_v(f)}{u_{*\ell}^2} = \frac{14n/\phi_m}{1+42\,(n/\phi_m)^{5/3}}\left(\frac{\phi_\varepsilon}{\phi_m}\right)^{2/3}, \tag{6.8}$$

$$\frac{fS_w(f)}{u_{*\ell}^2} = \frac{4.6n/\phi_m}{1+14.5\,(n/\phi_m)^{5/3}}\left(\frac{\phi_\varepsilon}{\phi_m}\right)^{2/3}. \tag{6.9}$$

Results indicate that this model can be successfully applied for the velocity spectra in the SBL even over inhomogeneous surfaces. As expected, this model is more appropriate for the representation of the spectra in the SBL over inhomogeneous surface than Kaimal's (neutral) model. However, in order to apply Olesen model it is necessary to know dimensionless functions of the wind shear and TKE dissipation rate. We note that for horizontal velocity components there is a good correspondence

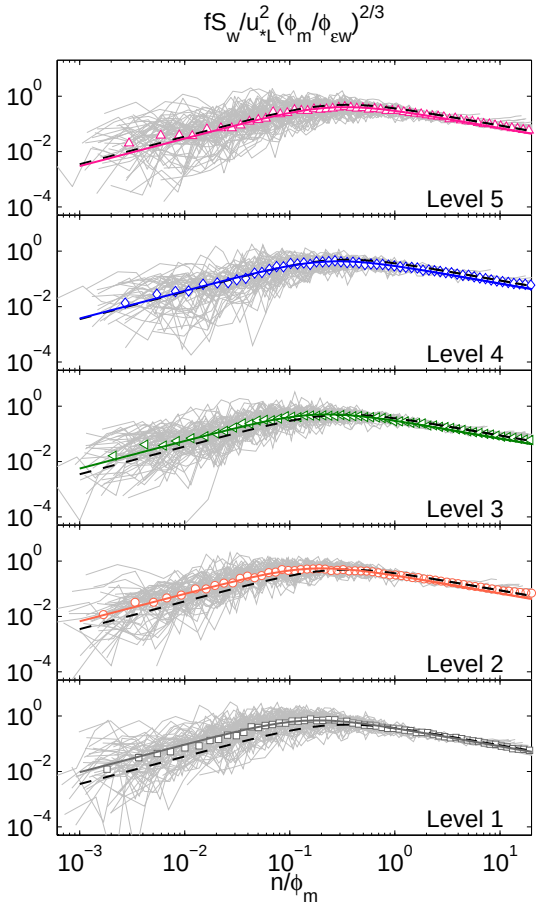

Figure 6.13: The same as Fig. 6.12 but for the vertical velocity component.

between spectra for different stability classes (Fig. 6.14) in the high-frequency range ($\sim n/\phi_m = 0.5 - 20$), but in the low-frequency part the correspondence vanishes and the same was also observed for the Kansas model spectra. Additionally, median spectra exhibit a gap at low frequencies and this is most obvious for the upper four levels. The existence of such a gap for SBL has been observed by many different authors (Olesen et al. 1984, and references therein). This gap separates the turbulent part of the spectrum and the low-frequency part where a steep increase in spectral energy is observed. This characteristic is usually attributed to the wave activity, primarily gravity waves, in the SBL.

Overall, for the present stable night-time spectral results from a forested site with highly inhomogeneous fetch conditions different scaling approaches were considered. The traditional SL scaling was tested against the canopy scaling, which is generally valid for the RSL. The results suggest that canopy variables h_c and U_{hc} are good for normalizing the frequency. When frequency weighted velocity spectral densities are normalized with local values of corresponding σ_i^2 $(i = u, v, w)$, the spectra collapse to a single curve within the whole measurement layer. If frequency

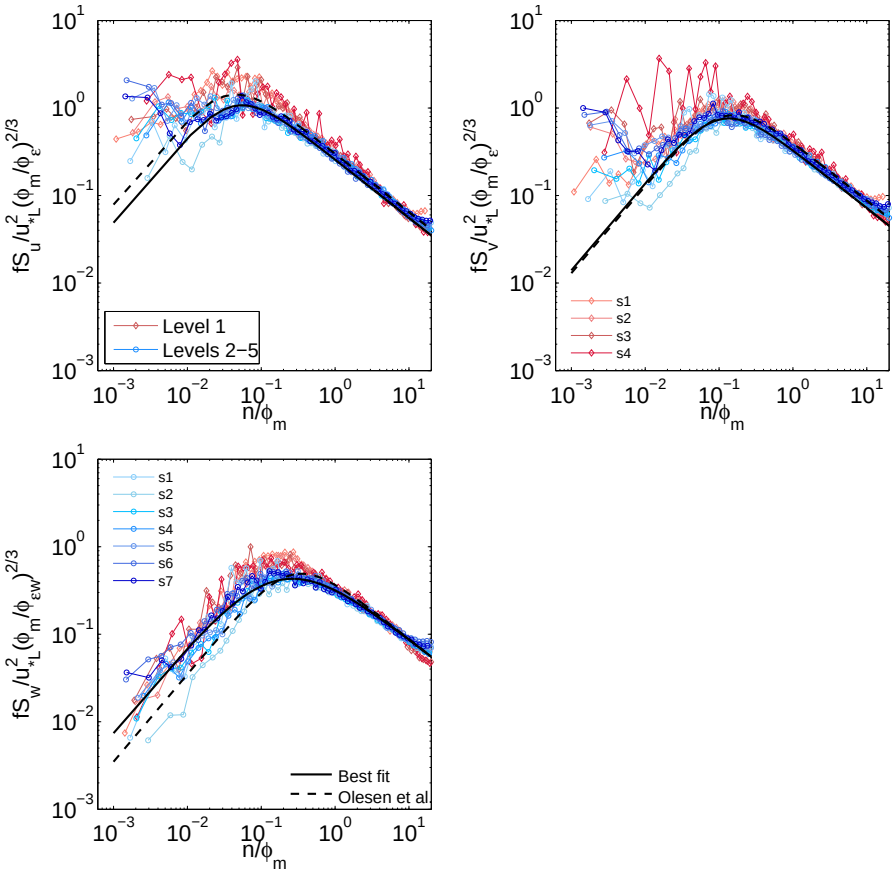

Figure 6.14: Normalized spectra of all three velocity components for different stability classes at level 1 (red colors) and levels $2-5$ (blue) as indicated in Table 6.2. Dashed black line corresponds to Eqs. 2.41 – 2.43 and solid line indicates the best fit to the data for levels $2-5$ (Eqs. 6.7 – 6.9).

weighted spectral densities are normalized with $u_{*\ell}^2$, a clear difference between RSL and transition layer can be observed. The fact that canopy scaling can be successfully applied even within the transition layer suggests that large coherent eddies, which are generated at the canopy top, are dominating the turbulence structure up to a hight which is more than three times the h_c. For the present complex site local isotropy was not found. Namely, the reduced spectral power in the vertical velocity component was consequently reflected in smaller values of the ε estimated from the vertical component spectra (ε_w) compared to the estimates from horizontal components ($\varepsilon_{u,v}$). These different estimates of ε had a direct influence on the applicability of spectral models, which are valid for HHF terrain, to the present dataset. Using ϕ_{ε_w} to normalize vertical spectra the overall form and magnitude of scaled spectral densities were found equal to the Kansas curves. Therefore, a good correspondence with the Kansas spectral models was observed for measurements in the transition layer when different estimates of ϕ_ε were used. The same was true for spectral models of Olesen et al. (1984), which were found appropriate to represent the spectra in

the SBL over inhomogeneous surface.

6.2 The dimensionless TKE budget

So far it has been shown that local similarity scaling can be successfully applied for different dimensionless stability functions in the SBL over inhomogeneous surface. In this section the focus is on evaluating the dimensionless budget of TKE (Eq. 2.45). The dimensionless TKE budget terms were calculated from 30-min averaged data using local values at measurement height z. Non-dimensional wind shear and dissipation rate of the TKE were calculated as explained in Sections 5.4 and 6.1.3, respectively. The non-dimensional turbulent transport term (ϕ_t) was calculated on four mid-levels between adjacent tower levels using finite difference method. This method was found to be more effective than the profile fitting by polynomials (using second and third order polynomials), since the vertical flux of the TKE ($\overline{w'e}$) showed considerable variability with height. Therefore, in order to close the TKE budget ϕ_m and ϕ_ε were also calculated at the four mid-levels using average values between the adjacent levels. The pressure transport and advection terms were considered to be a residual term[2], which was calculated as

$$R = -\phi_m + \zeta + \phi_t + \phi_\varepsilon. \tag{6.10}$$

This term includes not only the sum of the pressure transport and advection terms, but also accumulates errors when calculating the terms on the right-hand side of Eq. (2.45). Despite these shortcomings, the residual approach has been widely used to investigate the pressure transport in the BL (under the assumption of horizontal homogeneity and stationarity of the flow, e.g. Högström 1990; Li et al. 2008; Duarte et al. 2015; Nilsson et al. 2015). For the budget analysis only those simultaneous (at all levels at the same time) 30-min intervals for which the inertial subrange was detected were used. This resulted in a reduced dataset compared to results presented so far, with final set of 63, 65, 68, 51 and 67 data points at levels 1 to 5, respectively.

6.2.1 The dimensionless shear production

The stability dependence of the dimensionless wind shear is discussed in detail in Section 5.4, where the validity of the z-less scaling was examined using the approach of Grachev et al. (2013) who distinguished between subcritical ($Rf \leq 0.25$) and supercritical ($Rf > 0.25$) turbulence regimes. They have defined the subcritical regime for data having $Rf < 0.25$ and it was associated with the existence of a well-defined inertial subrange, i.e. spectral densities of velocity components and sonic

[2]The storage term is assumed to be zero by the stationarity test.

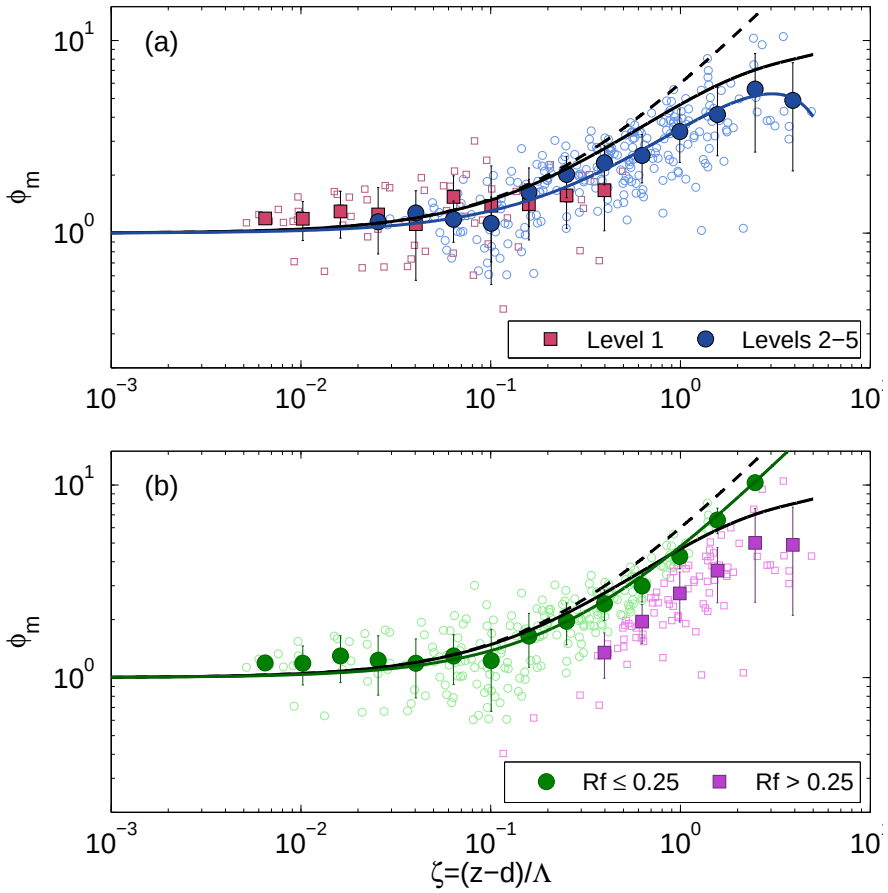

Figure 6.15: **(a)** The data used in the TKE budget analysis ("Kolmogorov turbulence") from the first (red) and four upper levels (blue). The dashed line indicates the linear relation of Dyer (1974, Eq. 2.6) and the solid black line shows the relationship proposed by Beljaars and Holtslag (1991, Eq. 2.7). The blue line indicates the best fit of Eq. (2.7) for levels $2-5$ with the best fit coefficients obtained using the least squares method: $a = -2.28$, $b = 0.455$, $c = 10.87$ and $d = 0.12$. **(b)** The data from panel **(a)** divided into sub- and supercritical regimes. The green line indicates the best fit from Section 5.4: $\phi_m = 1 + 3.8\zeta$.

temperature had a well-defined $-5/3$ slope within the high-frequency band. Therefore, they associated this regime with "Kolmogorov turbulence". The supercritical regime was defined for data with $Rf > 0.25$, for which a collapse of the inertial subrange was observed. Some small scale turbulence survived in this regime, which they named as "non-Kolmogorov turbulence" (due to the absence of well defined $-5/3$ slope), which also decayed rapidly with increasing stability. Grachev et al. (2013) argued that the violation of the z-less scaling was mainly associated with the "non-Kolmogorov turbulence" in the supercritical regime.

In Chapter 5 their critical value of $Rf = 0.25$ was used and the ϕ_m function in the subcritical regime followed a linear dependence on ζ, indicating adherence to the z-less limit. While the data presented in Section 5.4 were not tested for the existence

of the well defined $-5/3$ slope of velocity spectral densities in the high-frequency range, in this section only those data for which a well-defined inertial subrange was found are considered, i.e. only "Kolomogorov turbulence" data.

Figure 6.15(a) shows dimensionless shear production for data with a well-defined inertial subrange (used in the TKE budget analysis). It was observed that these data have values of Rf below and above 0.25. The data corresponding to $Rf \leq 0.25$ (green) and $Rf > 0.25$ (violet) are indicated in Fig. 6.15(b). We note that many periods with "Kolmogorov turbulence" (well-defined inertial subrange) were observed for $Rf > 0.25$. This is in contrast with findings over ideal homogeneous and flat surfaces by Grachev et al. (2013). The present data associated with "Kolmogorov turbulence" show smaller values compared to the linear prediction and a better correspondence with the relation of Beljaars and Holtslag (1991). This, of course, suggests a breakdown of the z-less regime. The same was observed by Duarte et al. (2015) and they concluded that the presence of "Kolmogorov turbulence" is not a sufficient criterion to guarantee the validity of z-less concept. Additionally, they hypothesized that an injection of non-local TKE via pressure transport was the main reason for the observed breakdown of the z-less scaling. Högström (1990) related this to the concept of 'inactive' turbulence, a concept introduced by Townsend (1961) and further elaborated by Bradshaw (1967), which consists of large-scale fluctuations that lead to increased mixing. Therefore, the decrease of ϕ_m below the linear z-less prediction could be caused by the increased mixing due to the injection of 'inactive' turbulence via pressure transport which may lead to a decrease in the wind speed gradient.

6.2.2 The dimensionless turbulent dissipation

In Section 6.1.4 it was shown that ϕ_ε has different values if estimated only from horizontal components and from the vertical one. Estimates of ϕ_ε based on u and v components were larger compared to ϕ_{ε_w}. Therefore, the mean ϕ_ε (ϕ_{ε_m}) was calculated for each layer (Fig. 6.16). The mean estimate of ϕ_ε will give a better correspondence to respective stability functions valid for HHF terrain, at least in the transition layer. At the lowest measurement level, due to the RSL influence, ϕ_{ε_m} function in neutral regime has lower values than one and in the transition layer close to one, thus a modified version of Eq. (2.29) was fitted to the data (Table 6.3) in order to account for the deviation from unity.

Since values of ϕ_m at level 1 under neutral conditions obtained by the least squares fitting are close to one ($\phi_m(\zeta = 0) = 1.1$) and $\phi_\varepsilon(\zeta = 0) = 0.31$, this indicates local imbalance of TKE in the RSL under neutral conditions, which is not unexpected. Note that $\phi_m(\zeta = 0)$ obtained in this way is not exactly unity due to

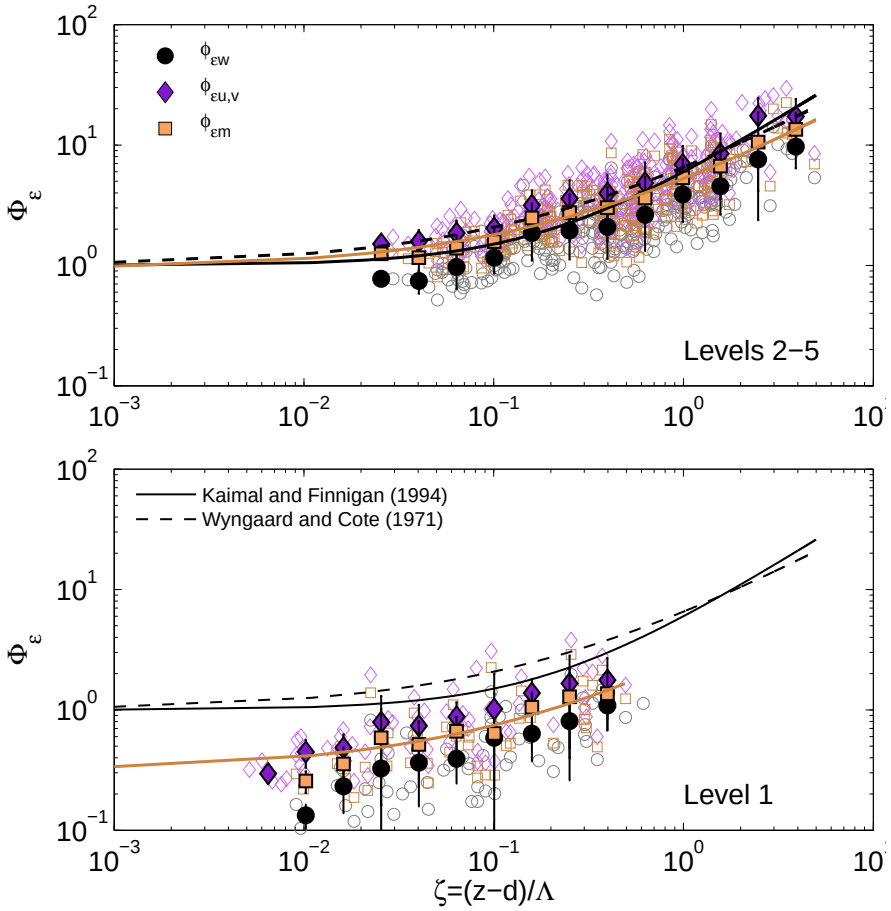

Figure 6.16: Non-dimensional dissipation rate of the TKE plotted versus the stability parameter. Solid and dashed curves are the same as in Fig. 6.4.

larger uncertainty when fitting the wind profile within the RSL by using second order polynomial, which resulted with substantial scatter. Nevertheless, the above result suggests that under neutral conditions, approximately 30 % of the shear generated TKE is locally dissipated. The remaining TKE will be transported to higher layer by turbulent and pressure fluctuations and advection. A slightly different result is obtained if the actual (not fitted) data for $\zeta < 0.05$ are used where the mean values for ϕ_m and ϕ_ε are 1.21 and 0.47, respectively. If the stability range up to $\zeta = 0.1$ (often used as upper limit of neutral stability) is considered, then mean values of ϕ_m and ϕ_ε are equal to 1.31 and 0.56, respectively.

Unfortunately, a very small number of data corresponding to near-neutral conditions ($\zeta < 0.05$) was observed for levels $2-5$ (only five individual data at level 2). Thus, it was difficult to investigate the local balance of TKE under neutral conditions. The best fit curves shown in Figs. 6.15 and 6.16, however, indicate the convergence of ϕ_m and ϕ_{ε_m} to 1 and 0.94 when approaching to neutral limit, respectively. This implies a locally imbalanced TKE under neutral conditions even within the transition layer.

6.2.3 The dimensionless turbulent transport

Due to the substantial variation of the vertical flux of TKE with height (Fig. 6.17), it was not possible to fit the profile of $\overline{w'e}$ by using the different polynomial fitting methods. Thus, the non-dimensional turbulent transport term

$$\phi_t = \frac{k(z-d)}{u_{*\ell}^3}\frac{\partial(\overline{w'e})}{\partial z} \tag{6.11}$$

was calculated at four mid-layer heights ($z = 26, 36, 47.5$ and 58.5 m), using finite difference method and the average $u_{*\ell}$ between the adjacent levels.

Estimated values of ϕ_t show considerable scatter in the layer $2-5$ (Fig. 6.18). Although the scatter was larger for layer $2-5$ than for layer $1-2$, bin median values still showed a quite good correspondence between upper levels for a wide range of stabilities (not shown), indicating that the local scaling approach is also suitable for estimating turbulent transport. Under neutral conditions turbulent transport is often assumed to be zero (e.g. Wyngaard and Coté 1972; Högström 1996). However, for the mid-level at 26 m, estimated values of ϕ_t are mainly positive, with the best fit curve (Eq. 2.47) converging towards 0.30 in neutral limit (Table 6.3). The influence of the RSL is obvious at this mid-level, causing higher values of ϕ_t compared to layer $2-5$. Högström (1996) attributed positive values of the turbulent transport to the aerodynamic properties of the surface, i.e. surface of widely varying roughness elements of considerable height will cause a non-zero turbulent transport.

Table 6.3: The best fit functions for dimensionless budget terms fitted to data at level 1 and levels $2-5$.

Level	ϕ_m	ϕ_{ε_m}	ϕ_t
Level 1	$\phi_m = 1.11 + 2.44\zeta$	$\phi_{\varepsilon_m} = 0.31(1 + 3.1\zeta^{3/5})^{3/2}$	$\phi_t = 0.30 + 0.66\zeta$
Levels 2-5	$*$	$\phi_{\varepsilon_m} = 0.94(1 + 2.2\zeta^{3/5})^{3/2}$	$\phi_t = 0.23 - 0.33\zeta$

$* \ \phi_m = 1 + a\zeta + b\zeta e^{-d\zeta} - bd\zeta(\zeta - \frac{c}{d})e^{-d\zeta}$, with $a = -2.28$, $b = 0.46$, $c = 10.87$ and $d = 0.12$.

For the three upper mid-levels within the transition layer, ϕ_t exhibits large scatter with more negative values compared to first mid-level, while bin medians indicate on average small positive values in the stability range $0 < \zeta < 1$. For the strongly stable regime mostly negative values and large deviation from zero line are obtained. These large deviations as well as the large scatter obtained, could be the result of the finite difference method used to calculate the gradients, introducing errors in the estimates of ϕ_t (e.g. Duarte et al. 2015), especially during more stable conditions where turbulence is weak and intermittent (e.g. Mahrt 1998; Mauritsen et al. 2007; Baklanov et al. 2011).

Additionally, following Li et al. (2008) the expression (2.47) was fitted to the

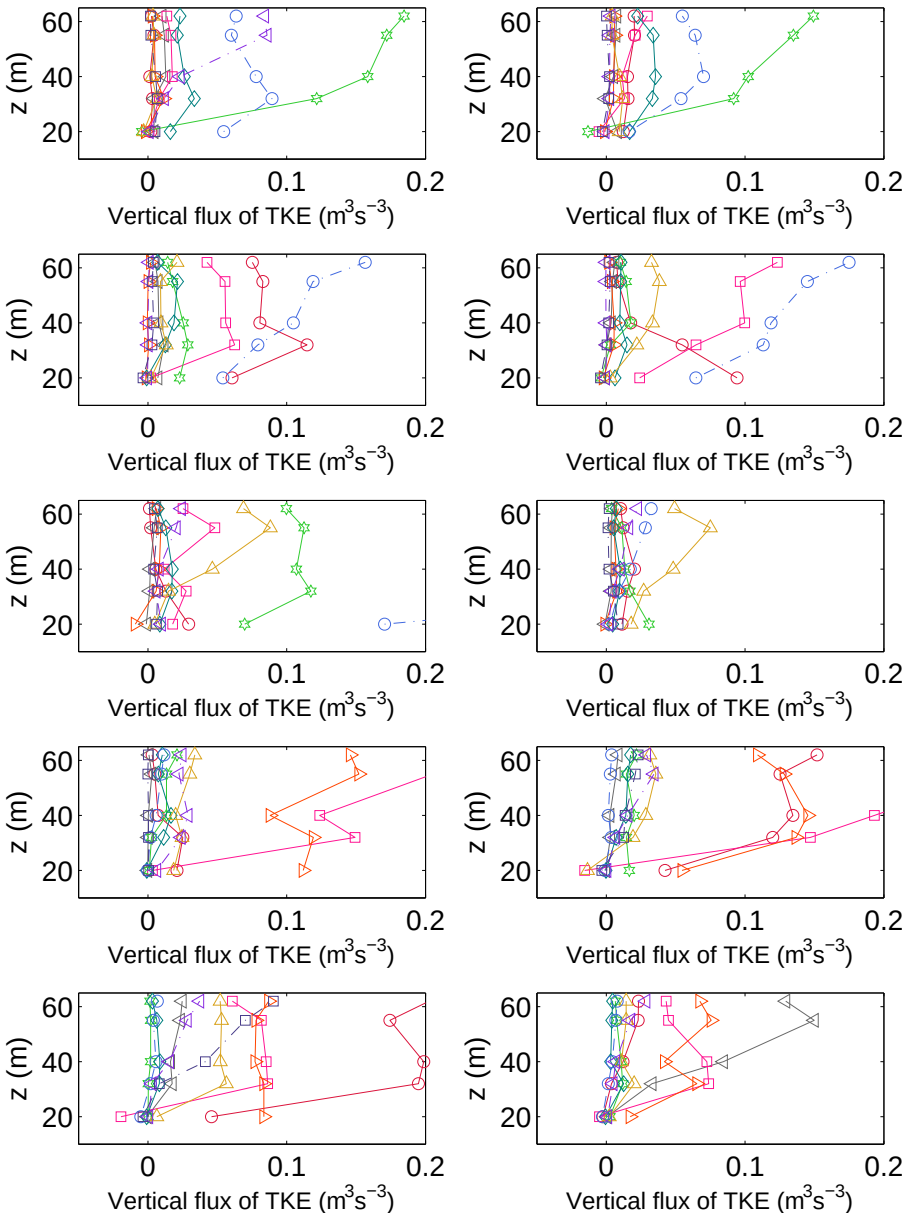

Figure 6.17: Vertical profiles of the vertical flux of TKE used for the calculation of the dimensionless turbulent transport term in the TKE budget. Each sub-panel shows 10 individual profiles (100 in total), which are presented with different color, showing considerable variation with height.

data at the first mid-level and from upper levels up to $\zeta = 2$ (Fig. 6.18 and Table 6.3). We note that these functions represent the data at weakly and moderately stable conditions quite well, while in strongly stable limit the data deviate from this linear relationship.

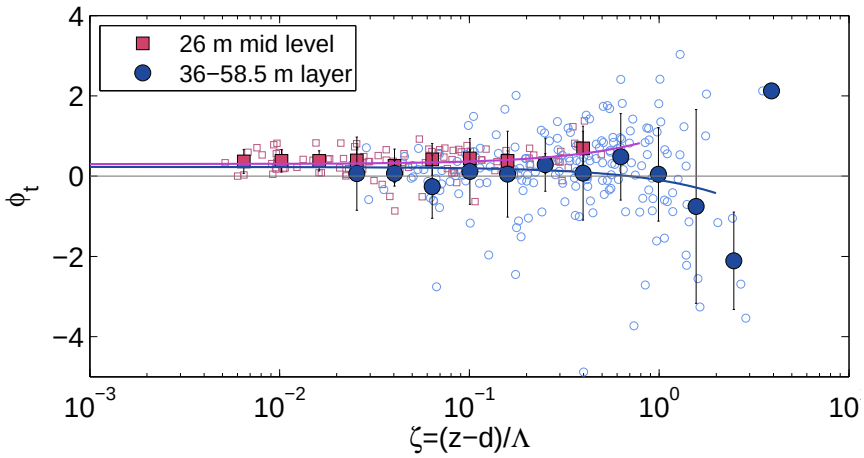

Figure 6.18: Estimates of the dimensionless turbulent transport as a function of ζ shown for z=26 m (red) and in the layer 36 − 58.5 m (blue) separately. Error bars indicate one standard deviation within the bin. Violet and blue solid curves indicate the best least squares fitting for data points up to $\zeta = 2$ for the lower and upper layer, respectively.

6.2.4 Budget of TKE

Figure 6.19 shows estimated dimensionless terms of TKE budget (Eq. 6.10) within the RSL and the transition layer separately. The residual term accounts for the pressure transport term and the advection as well as all other terms which can not be estimated, such as, horizontal derivatives. In the transition layer, as expected for the SBL, the dominant terms are the mechanical production and dissipation of TKE (Fig. 6.19). The residual term has comparable magnitudes, but it represents the sum of all other terms which could not have been estimated. Li et al. (2008) have defined the dimensionless local imbalance function $\phi_{LI} = -\phi_m + \zeta + \phi_\varepsilon$. The total local losses of TKE, i.e. $\zeta + \phi_\varepsilon$, exceed the local shear production, resulting in a positive ϕ_{LI}, which indicates a gain of TKE in the layer. This local imbalance of TKE over all stabilities has been reported in many different studies (e.g. Högström 1990; Frenzen and Vogel 2001; Li et al. 2008; Duarte et al. 2015). Li et al. (2008) have argued that non-local dynamics is the main mechanism responsible for the observed imbalance. Högström (1990) used an inactive turbulence theory to explain the observed gain of energy in the SL, which is associated mostly with the excess of dissipation. Assuming HHF terrain and neglecting the advection of TKE, this energy gain is then attributed to the pressure transport term (Högström 1990; Duarte et al. 2015).

Of course, all these considerations are based on the assumption that we only look at the vertical gradients (boundary layer approximation) and neglect the terms with horizontal derivatives. However, at this heterogeneous forested site, which involves adaptation to the transition after the forest edge, horizontal gradients might have

non-negligible magnitudes. For example, Yang et al. (2006) used LES to investigate momentum and TKE budgets across a forest edge. They have found that the most important processes at the forest edge are production due to the convergence (or divergence) of the mean flow, streamwise advection, pressure diffusion and enhanced dissipation by canopy drag.

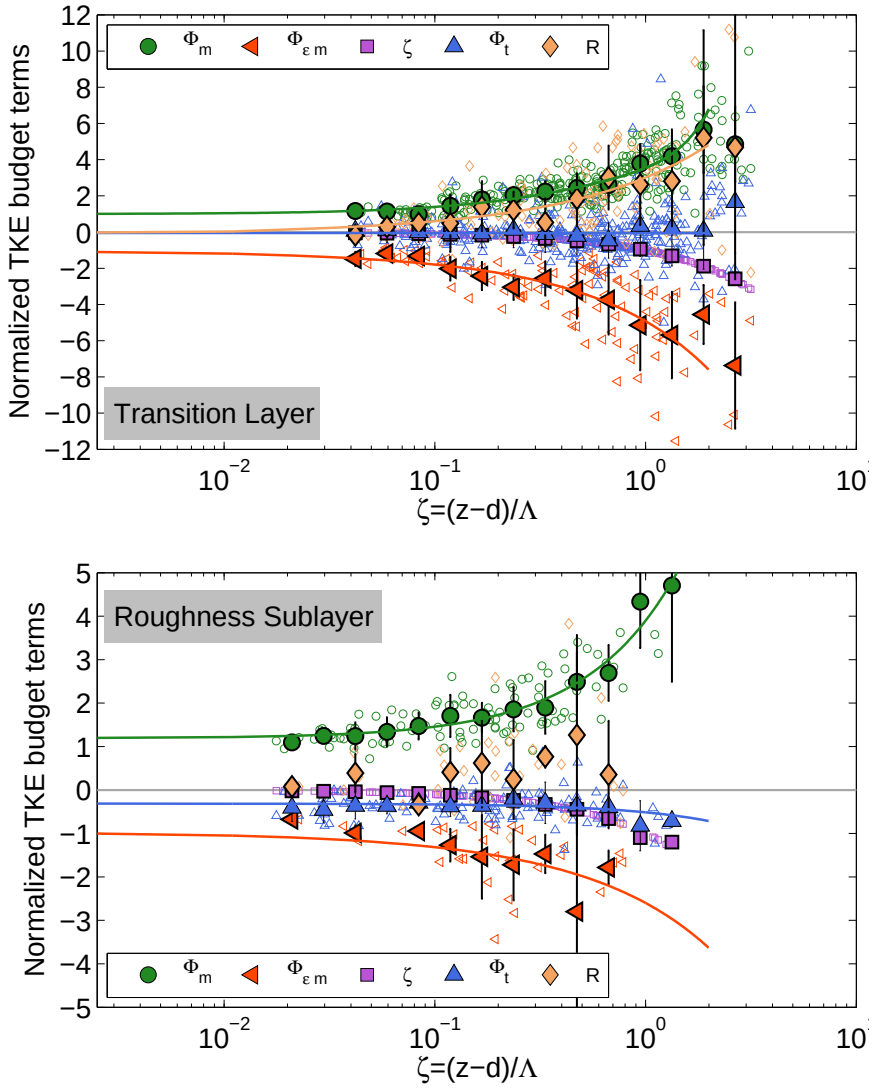

Figure 6.19: Normalized TKE budget terms shown separately for measurements within the RSL (*lower panel*) and transition layer (*upper panel*). Individual data are shown as background symbols while bin medians are shown as filled symbols. Error bars indicate one standard deviation within each bin. The green, orange, blue and yellow curves represent the best fits of ϕ_m, ϕ_ε, ϕ_t and residual term, respectively (Table 6.3).

Within the RSL, the shear production is larger than buoyant destruction and dissipation of TKE, resulting in a negative ϕ_{LI} and indicating the loss of energy in this layer in the stability range up to $\zeta = 0.1$. The pronounced imbalance between TKE production and dissipation within the RSL under neutral conditions is con-

sidered to be mainly due to the contribution of TKE turbulent transport above a vegetated surface (Mammarella et al. 2008, and Fig. 6.19). Figure 6.19 shows that estimated values of ϕ_t are significant within this layer. The negative ϕ_{LI} is balanced with the positive ϕ_t resulting with approximately zero R term in the neutral range. These results are in agreement with findings of other studies above canopies (e.g. Raupach et al. 1986; Brunet et al. 1994), where turbulent transport in the RSL close to the canopy top was found to be a sink of TKE. Mammarella et al. (2008) and Yang et al. (2006) have investigated vertical profiles of TKE budget terms and found that values of ϕ_t are decreasing with height and the same was observed in present dataset (Fig. 6.18). Therefore, the contribution of the turbulent transport to the residual term is reduced in the transition layer compared to the RSL. For higher stability, the residual term has a positive sign and becomes a gain of TKE in the RSL.

The residual term shows more systematic behavior within the transition layer compared to the RSL. Li et al. (2008) argued that a less systematic behavior of the residual term, i.e. energy gain/loss suggests more dominant mean advection term. These considerations and present results would imply that the advection term has more pronounced influence on the RSL than the upper levels. Additionally, the advection term should have larger influence on the residual term under strongly stable conditions (Li et al. 2008). However, these are only hypothetical considerations since it is not possible to actually estimate the advection term based on the available data. Moreover, due to horizontally inhomogeneous site characteristic and uncertainty in the estimated vertical TKE transport, it is impossible to quantify the magnitude of the pressure transport term nor any of the terms including horizontal derivatives which might have non-negligible values at this complex site. Nevertheless, as evident from the residual term, the pressure transport will most likely act as a gain of TKE within the transition layer for the entire range of stabilities (Fig. 6.19). In the literature different results are reported regarding the pressure transport contribution to the TKE budget. For example, in the neutral limit, Högström (1990) and Duarte et al. (2015) obtained positive values for the pressure term, while Li et al. (2008) and Nilsson et al. (2015) found negative values of -0.25 and -0.19, respectively. Additionally, Li et al. (2008) found pressure transport to be small for $0 < \zeta < 0.6$ and to become a loss of TKE for larger stabilities. In these studies it was assumed that the residual term represents mostly pressure transport and the same assumption can not be made for the present site.

Finally, the best fit functions for each of the dimensionless budget terms with the newly obtained coefficients are presented in Fig. 6.19. For all functions the best fit coefficients were found only for the data up to $\zeta = 2$, due to the higher uncertainty at higher stability. A linear function was used to obtain the best fit for

the ϕ_m function within the RSL and yielded $\phi_m = 1.19 + 2.71\zeta$, while non-linear behavior of this function is observed in the transitions layer and the experimental relationship proposed by Beljaars and Holtslag (1991) was fitted to the data. The best fit coefficients obtained are $a = 24.9$, $b = 31.79$, $c = -1.65$ and $d = 0.28$. A slightly modified version of the formulation proposed by Wyngaard et al. (1971) $\phi_\varepsilon = a(1+b\zeta^{3/5})^{3/2}$, which accounts for the deviation from unity in the neutral limit, was used to present the dimensionless dissipation in both, the RSL and transition layer. For the RSL the best fit function is $\phi_{\varepsilon_m} = 0.96(1 + 0.95\zeta^{3/5})^{3/2}$, while $\phi_{\varepsilon_m} = 1.0(1 + 0.9\zeta^{3/5})^{3/2}$ is the best fit for the data within the transition layer. Since the residual term showed systematic behavior only within the transition layer, the best fit function is obtained only for this layer. Based on the above results, the residual term in the neutral limit must equal to -0.05 in order to close the budget in this simple model. The non-linear expression $R = (-0.05 + 5.2\zeta)^{0.67}$ was found to best represent this term.

Chapter 7

Conclusions

7.1 Summary and Conclusions

Multi-level measurements of atmospheric turbulence carried out over a heterogeneous surface in the continental part of Croatia have been used to study turbulence characteristics in the wintertime nocturnal boundary layer. The overall goal was to contribute to the field of the boundary layer meteorology by describing how heterogeneous and complex surface characteristics alter turbulence properties compared to better known results for flat and homogeneous terrain. Measurements that were obtained from five levels in the layer between 20 and 62 m above the ground and $2 - 44$ m above the local canopy height, provided valuable insight in the turbulence characteristics within tens of meters above the ground level. This study focused on evaluating the applicability of local similarity scaling approach, in terms of flux-variance and flux-gradient similarity, properties of turbulence spectra and applicability of existing spectral models, and local balance of turbulent kinetic energy (TKE) over spatially inhomogeneous surface characteristics.

Due to specific local terrain characteristics and distinctive features of the stable boundary layer (SBL), special attention was given to data quality control and post-processing options. These included determination of appropriate turbulence averaging time scale for defining turbulence fluctuations, testing the stationarity of the data and invoking an uncertainty test. Observations were conducted inside (the lowest observational level) and above the roughness sublayer (RSL).

After removing highly uncertain data points (uncertainty threshold > 50 %), when assessing scaling under inhomogeneous fetch conditions in the SBL, flux-variance similarity relationships were found to behave differently than the flux-gradient relationships. Concerning the normalized standard deviations, it was found that vertical velocity shows a tendency to "ideal" behavior, that is, it follows z-less scaling when approaching large stability. The longitudinal and transversal com-

ponents show dependence on static stability, with the latter exhibiting a more pronounced linear increase with increasing stability. Consequently, scaled TKE was found to have a linear dependence on the stability parameter in the range $0.05 \leq \zeta \leq 10$ for levels above the RSL. However, local scaling was found to be valid for all three variables, which is astonishing given the complex and spatially inhomogeneous surface characteristics. For neutral conditions, due to the RSL influence, values of all three non-dimensional velocity variances were found to be smaller at the lowest measurement level, while these were larger at higher levels in comparison with values obtained for HHF terrain. The ratio of the observed dimensionless standard deviation of the vertical wind component and corresponding values of commonly used similarity formulas over horizontally homogeneous and flat (HHF) terrain showed considerable variation with wind direction, indicating the influence of surface roughness changes and orography. Therefore, I separately analyzed velocity variances for different wind directions corresponding to undistorted ($\phi_w/\phi_{w(HHF)} \approx 1$) and distorted ($\phi_w/\phi_{w(HHF)} \neq 1$) sectors, respectively. Differences between these sectors at the lowest level were found only in the near-neutral regime with larger magnitudes for the distorted sectors. At upper levels, dimensionless longitudinal and vertical wind variances also showed higher values for these wind directions. However, this did not influence results regarding the relationship with stability. For non-dimensional velocity variances, and consequently, non-dimensional TKE and the momentum and heat flux correlation coefficients, no discernible difference between sub- and supercritical regimes was observed.

Results for the non-dimensional wind shear appear to be less sensitive to inhomogeneous site characteristics. Despite the largely inhomogeneous surface characteristics at the measuring site, flux-gradient relationship (ϕ_m) showed a similar distinction between sub- and supercritical regimes as found under ideal (HHF) conditions (Grachev et al. 2013). These results support the classical Businger-Dyer linear expression for the non-dimensional profile of wind speed, with slightly different best-fit coefficient, even over inhomogeneous terrain but only after removing data which correspond to the flux Richardson number $Rf > 0.25$. Hence, our data follow local z-less scaling for the ϕ_m function when the condition $Rf \leq 0.25$ is imposed. Similar to HHF conditions, supercritical ($Rf > 0.25$) data show a leveling off for ϕ_m at higher stability thus, seemingly supporting the non-linear relationship of Beljaars and Holtslag (1991). Therefore, it is concluded that the non-dimensional wind shear over a largely heterogeneous vegetated surface is only weakly, if at all, affected by the surface inhomogeneity. Thus, when interested in only subcritical, fully turbulent conditions, the classical linear formulation for ϕ_m is appropriate. Correspondingly, if all turbulence states (regardless of sub- or supercritical) are of interest, the Beljaars-Holtslag formulation is to be preferred. Finally, it was in-

vestigated whether the wind magnitude has an impact on the distinction between turbulence characteristics in sub- and supercritical regimes. The ϕ_m dependence on stability did not show different behavior for different wind regimes, indicating that the stability parameter is sufficient predictor for flux-gradient relationship.

Further investigations focused on the influence of heterogeneous terrain on turbulence spectral characteristics as well as dissipation rates of TKE (ε). Surface layer (SL) scaling using local values of u_* and $z-d$ was not valid above the rough vegetation canopy. Instead, the canopy scaling (using the mean wind speed from the first measurement level and the canopy height) was shown to be successful through the entire measurement layer. Additionally, wind variances were found to be relevant for collapsing the spectra from all five levels to a single curve. Estimated values of the non-dimensional TKE dissipation rate (ϕ_ε) at the lowest measurement level indicated clear influence of roughness elements, while ϕ_ε dependence on stability at higher levels can be approximated with the modified functional form proposed by Wyngaard et al. (1971) in order to account for the deviation from unity (local balance) in neutral conditions. The vertical velocity spectra were observed to be smaller than horizontal spectra and consequently ε determined only from vertical spectra were smaller in comparison with ε estimates from horizontal components. Therefore, it was necessary to normalize vertical spectra with ϕ_{ε_w} to obtain good correspondence with the Kansas spectral model. The same was observed when the model of Olesen et al. (1984) was applied. This, in fact, demonstrates that true local isotropy is not found at this complex surface site. As pointed out by Wyngaard (2010) local isotropy can only be found in a truly homogeneous flow field, which is not found in the vertical direction and even less over inhomogeneous canopies, such as forest or urban. The spectral model of Olesen et al. (1984) was for the first time applied to data over heterogeneous plant canopy and was found to be successful. Influence of sub-meso motions was evident in the spectra of horizontal velocity components at lower frequencies due to the fact that only a linear trend was removed from each 30-min run and no filtering of the data was performed. Based on the results of MFD analysis, sub-meso motions have time scales above 100 s, which is also evident in the spectra.

The dimensionless wind shear function associated with "Kolmogorov turbulence" (existence of a well-defined inertial subrange with $-5/3$ slopes) was found to depart from linear prediction. Many of individual data corresponding to "Kolmogorov turbulence" were observed in the supercritical regime ($Rf > 0.25$) indicating survival of turbulence above the inhomogeneous surface at higher Rf in comparison to a homogeneous one. This suggest that the stability (Rf) is a stronger determinant of the ϕ_m behavior than the inertial subrange behavior is. The nonlocal dynamical processes are possibly the reason for the observed breakdown of the

z-less regime in the strongly stable conditions above heterogeneous surface.

The local equilibrium between the production and destruction of TKE was found to be violated indicating that the transport terms and advection are important, with the vertical TKE transport being more pronounced within the RSL than the transition layer. In the transition layer, the total local losses of TKE exceeded the local shear production, resulting in positive residual term corresponding to gain of TKE in this layer. Within the RSL, the shear production was larger than buoyant destruction and dissipation of TKE, thus the residual term corresponds to a loss of energy in this layer in the stability range up to $\zeta = 0.1$. For higher stabilities the residual term changed sign and became a gain of TKE in the RSL.

7.2 Outlook

Results of this dissertation have demonstrated that classical ABL theories, which were originally developed for HHF terrain, can be applied even over very heterogeneous surfaces when the local scaling approach is used, however, the corresponding non-dimensional functions do not exhibit the same parameter values as over HHF terrain. Moreover, these results have also emphasized the need for the further development of theory, measurements and high-resolution numerical simulations to deal with non-equilibrium effects. In particular, thoughtful field campaigns should focus on the attempts to measure and analyze local and non-local effects above inhomogeneous surfaces, such as fetch limited forests. In future studies of SBL over inhomogeneous terrain long term measurements and high-quality datasets would be desirable in order to include data covering a wide range of stabilities (from near-neutral to strongly stable). In future work, research should focus on additional factors influencing turbulence characteristics such as:

- Influence of coherent structures on turbulent fluxes. This should include analysis of their occurrence, duration, frequency, vertical extent, contribution to turbulent fluxes, etc.

- Analysis of classes of (sub)mesoscale structures in the SBL and their role in determining turbulence structure as well as their interaction with turbulence.

- Testing the local isotropy hypothesis for heterogeneous and complex terrain. Detailed analysis of its implications on the TKE budget equation.

- Quantifying the effect of non-local dynamics, i.e. the pressure transport term in the TKE budget. Since the currently available sensor technology does not allow for direct and accurate calculation of this term, long term measurement

and numerical modeling studies are needed to help advance the understanding of pressure transport term.

Sažetak na hrvatskom jeziku

Poglavlje 1: Uvod

Atmosferski granični sloj (eng. *atmospheric boundary layer (ABL)*) je onaj dio atmosfere u kojem su tok mase, energije i impulsa pod direktnim utjecajem zemljine površine. Tema ovog doktorskog istraživanja je stabilni granični sloj (eng. *stable boundary layer (SBL)*). SBL se razvija netom nakon zalaska sunca zbog radijacijskog ohlađivanja slojeva blizu zemljine površine. Struktura noćnog graničnog sloja je primarno određena atmosferskom statičkom stabilnošću i procesima koji određuju mehaničku produkciju turbulencije, poput smicanja vjetra uzrokovanog trenjem, sinoptičkim strujanjem ili termalnim cirkulacijama ili pak niskim mlaznim strujama. SBL iznad kopna obično se klasificira prema jačini termalne stratifikacije te varira od slabo do vrlo stabilnog režima. Naš napredak u shvaćanju SBL-a je spor zbog mnogih različitih forsiranja koja se odvijaju na različitim vremenskim i prostornim skalama.To pridonosi kompleksnosti i postavlja izazove u proučavanju SBL-a.

I najmanja nehomogenost podloge može značajno utjecati na noćni granični sloj te dovesti do turbulencije pri većem Richardonovom broju u odnosu na homogenu podlogu. Budući da su kopnene podloge na Zemlji uglavnom nejednolike, interes za strujanje i karakteristike turbulencije iznad kompleksnih površina se povećao zadnjih desetljeća. Poznavanje karakteristika turbulencije je osobito važno za parametrizaciju procesa izmjene između površine i atmosfere u atmosferskim modelima disperzije polutanata, numeričkim modelima za prognozu vremena ili regionalnim klimatskim modelima. U tim modelima se za modeliranje karakteristika strujanja i disperzije koristi teorija sličnosti. Znanstvena zajednica ulaže značajan napor u ispitivanje primjenjivosti teorije sličnosti za različite uvjete. Većina eksperimentalnih studija se temelji na mjerenjima pri čemu su instrumenti postavljeni na tornjeve, a rezultati studija su ponekad međusobno nekonzistentni. Nekonzistentnost se uglavnom odnosi na studije u izrazito kompleksnom (npr. planinskom) terenu te studije turbulencije male skale, koja se javlja u jako stabilnim uvjetima kada sila uzgona ograničava vertikalna gibanja. U takvim slučajevima se gubi ovisnost o visini z i za njih vrijedi poseban režim skaliranja (eng. *z-less*). U ovoj disertaciji ispitujem primjenjivost lokalnog skaliranja u stabilnom graničnom sloju

iznad nehomogene podloge.

Poglavlje 2: Teorijska pozadina

Teorija sličnosti je jedna od osnovnih teorija u proučavanju graničnog sloja. Osnovna pretpostavka teorije sličnosti je da se struktura ABL-a može opisati pomoću karakterističnih parametara. Temelji se na organiziranju varijabli u bezdimenzionalne grupe. Ta procedura dimenzionalne analize proizilazi iz Buckingamovog π teorema. U okviru tog teorema biramo ključne varijable koje će činiti bezdimenzionalne grupe. Ispravan izbor bezdimenzionalnih grupa omogućava formiranje empiričkih relacija među njima. Te relacije bi trebale biti univerzalne, tj. trebale bi vrijediti svugdje u svakom trenutku za određenu situaciju. Razvoj teorije sličnosti se sastoji od četiri ključna koraka, a to su: (1) odabir relevantnih, tj. ključnih varijabli; (2) organizacija varijabli u bezdimenzionalne grupe; (3) određivanje vrijednosti tih bezdimenzionalnih grupa (varijabli) iz eksperimentalnih podataka; te (4) određivanje empirijske relacije koja opisuje vezu između ovih bezdimenzionalnih grupa. Znači, ta procedura rezultira empirijskom jednadžbom ili skupom krivulja koje imaju isti oblik, tj. izgledaju slično. Otuda naziv teorija sličnosti. Holtslag i Nieuwstadt (1986) su dali pregled režima skaliranja u SBL-u, gdje je svaki od režima karakteriziran različitim parametrima skaliranja. Turbulencija u prizemnom sloju se može opisati Monin-Obukhovljevom teorijom sličnosti (Obukhov, 1946; Monin i Obukhov, 1954) koristeći prizemne vrijednosti tokova impulsa i topline, te visinu z za parametre skaliranja. U tom sloju relevantan parametar skaliranja je Obukhovljeva duljina, L. Taj sloj se još naziva i sloj konstantnih tokova. Iznad prizemnog sloja se primjenjuje lokalno skaliranje (ili lokalna teorija sličnosti). To je režim kojeg je predložio Nieuwstadt (1984) i on predstavlja ekstenziju MOST-a u sloj iznad prizemnog, a razlika je u tome da se sve varijable računaju iz lokalnih vrijednosti tokova na mjerenoj visini z. U ovom režimu osnovni parametar je lokalna Obukhovljeva duljina, Λ. z/Λ je lokalni parametar stabilnosti i za njegove velike vrijednosti gubi se ovisnot o visini z jer stabilna stratifikacija ograničava vertikalna gibanja, te je stoga skala turbulencije jako mala. Taj granični slučaj se zove "*z-less*" stratifikacija, a znači da varijable ne ovise o visni. Nieuwstadt (1984) je našao da *z-less* uvjet vrijedi za vrijednosti parametra stabilnosti veće od jedan.

Poglavlje 3: Podaci i metode

Podaci analizirani u ovom radu su prikupljeni na 62 m visokom tornju u blizini kutinske Petrokemije. Toranj je smješten unutar male šume oraha. Podaci su mjereni ultrazvučnim anemometrima frekvencije uzorkovanja od 20 Hz na 5 visina

iznad približno 18 m visokih stabala oraha. Analizirani podaci dgovaraju zimskim mjesecima (od prosinca do veljače) i noćnim situacijama (1800 –0600 LST). Stabla oraha zauzimaju površinu od približno 120 m x 480 m. Nehomogenost podloge se odražava u miješanom utjecaju šume, agrikulturnih i industrijskih površina koje se nalaze u blizini mjernog mjesta. Osim varijablnim elementima hrapavosti, nehomogenost podloge je karakterizirana i varijabilnom orografijom dalje od tornja.

Kao rezultat specifičnih svojstava tog mjernog mjesta očekujemo da će se formirati različi vertikalni slojevi koji onda utječu na karakteristike turbulencije. Do formiranja vertikalnih slojeva moe doi kada strujanje zraka nailazi na naglu promjenu u karakteristikama podloge iznad koje struji. Iznad nove podloge dolazi do formiranja unutarnjeg graničnog sloja (eng. *internal boundary layer (IBL)*) čija visina raste s udaljenošću. Samo najnižih 10% ovog sloja je u ravnoteži s novom podlogom i naziva se unutarnji ravnotežni sloj (IEL), dok je strujanje iznad IBL u ravnoteži s podlogom koja se nalazi na navjetrinskoj strani. Ukoliko je nova podloga jako hrapava, kao sto je slučaj kod nas, onda se niži dio unutarnjeg ravnotežnog sloja naziva podsloj hrapavosti (eng. *roughness sublayer (RSL)*). Unutar RSL-a, strujanje je pod utjecajem raspodjele i strukture elemenata hrapavosti. Iznad IEL-a, napetost i tokovi se smanjuju s visinom zbog utjecaja podloge koja se nalazi na navjetrinskoj strani i ovaj sloj se naziva prijelazni sloj. Kako bih rezltate analize mogla tumačiti u okviru podsloja u kojem se nalazi mjerni nivo, procijenila sam da se najniži mjerni nivo najvjerojatni nalazi unutar podsloja hrapavosti, dok su viši nivoi unutar tzv. prijelaznog sloja. Prema tome će utjecaj podsloja hrapavosti biti očigledan u slučaju da se podaci mjereni na prvom nivou razlikuju značajno od mjerenja na višim nivoima.

Kako bih osigurala skup visoko kvalitetnih podataka na temelju kojeg će se raditi analiza, provela sam opsežnu i strogu kontrolu kvalitete podataka. Ona je u prvom koraku uključivala podjelu sirovih 20-Hz podataka u 30-min blokove podataka te su svi 30-min intervali s više od 1% nedostajućih podataka eliminirani iz daljnje analize. Isto je napravljeno ukoliko je broj podataka s nerealnim stršećim vrijednostima (eng. *spike*) bio veći od 1%. Priprema podataka za anlizu je uključivala i rotaciju koordinatnog sustava u smjeru srednjeg vjetra, pri čemu je napravljena prilagodba na ravninu (eng. *planar fit*). Za određivanje prikladnog intervala usrednjavanja korištene su četiri različite metode: Fourierova spektralna analiza, metoda kumulativnog kospektra (eng. *ogive*), višerezolucijska dekompozicija toka i valićna analiza. Rezultati primjene ovih metoda su prikazani u sljedećem poglavlju. Budući da je stacionarnost vremenskih nizova osnovna pretpostavka teorije sličnosti, proveden je test stacionarnosti prema Foken i Wichura (1996) kako bi detektirali nestacionarne 30-min intervale, koji su potom isključeni iz daljnje analize. Za intervale koji su proglašeni stacionarnima nadalje je napravljena procjena statističke neodređenosti,

odnosno pogreške uzorkovanja.

Poglavlje 4: Ispitivanje prikladnih vremenskih skala usrednjavanja u stabilnom graničnom sloju

Kontinuirani vremenski nizovi, koje bilježe ultrasonični anemometri, sadrže u sebi atmosferska gibanja na svim skalama te stoga obuhvaćaju nekoliko redova veličina. Da bi se mogla primijeniti metoda kovarijance vrtloga potrebno je razdvojiti trenutni signal na srednji dio i fluktuacije. U analizi turbulencije razlikujemo dvije osnovne skale usrednjavanja. Prva skala usrednjavanja τ (za usrednjavanje u vremenu) definira turbulenciju, odnosno, razdvaja turbulentna gibanja od onih na većoj skali. Druga skala usrednjavanja T jest Reynoldsova skala, a koja se koristi za određivanje statističkih momenata prvog, drugog i viših redova. Reynoldsova skala mora biti dovoljno duga kako bi se osigurala konvergencija statističkih momenata. Implicitna pretpostavka, koja omogućava razdvajanje strujanja u srednji i perturbirani dio, jest da postoji mezoskalni spektralni procjep. Prva od primijenjenih metoda za određivanje prikladnih turbulentnih vremenskih skala usrednjavanja je Fourierova spektralna analiza. Slika 4.1 prikazuje srednji spektar snage pomnožen s frekvencijom f za sve tri komponente brzine vjetra na svih pet mjernih visina u log-linearnom prikazu. Kad koristimo ovaj tip prikaza površina ispod spektralne krivulje je proporcionalna varijanci, odnosno, energiji (npr. Stull, 1988). Premda su individualni spektri dosta raspršeni (nije prikazano), srednji spektri za u i v komponentu brzine vjetra pokazuju postojanje spektralnog procjepa. Ovaj procjep je čak izraženiji za lateralnu komponentu strujanja u odnosu na longitudinalnu, budući da sadrži manje energije na većim skalama. Energijski procjep prisutan u srednjim spektrima horizontalnih komponenti brzine vjetra se nalazi na skalama koje odgovaraju periodima između 400 i 100 s.

Druga metoda za određivanje prikladnog intervala usrednjavanja koristi kumulativni ili klizni integral kospektra da bi se odredila frekvencija nakon koje više nema doprinosa kovarijanci (Oncley i sur., 1996; Foken i sur., 2006). Prikazi ovih spektara (*ogive*) održavaju kumulativni doprinos vrtloga rastućih perioda ukupnoj kovarijanci. Ako kumulativni spektar dosegne asimptotsku vrijednost pri nekoj frekvenciji f_c onda to upućuje na to da za frekvencije $f > f_c$ nema doprinosa toku (Moncrieff i sur., 2006). Vremenska skala usrednjavanja je tada jednaka $1/f_c$. Prema tome, ova skala usrednjavanja odgovara Reynoldsovoj skali. Srednji sirovi i izglađeni kospektar kinematičkog toka topline te odgovarajući kumulativni integrali kospektra za svih pet visina su prikazani na slici 4.2. Rezultati ove metode upućuju na to da je vremenski period od 30 min prikladan za usrednjavanje turbulentnih tokova te da

nema značajnijeg doprinosa tokovima iznad ovog perioda.

Višerezolucijska dekompozicija toka (eng. *multiresolution flux decomposition (MR)*, Howell i Mahrt (1997); Vickers i Mahrt (2003)) razdvaja varijancu i/ili kovarijancu fizikalnih veličina lokalno, odnosno, slično kao i klizni spektar uzima u obzir evoluciju promatrane varijable u vremenu ili prostoru. Stoga je prednost te metode u odnosu na Fourierovu spektralnu analizu u tome što je lokacija maksimuma u (ko)spektrima u toj metodi određena skalom duljine fluktuacija. Stoga nije potrebno imati periodičnost u podacima, dok u Fourierovoj analizi položaj maksimuma ovisi o periodičnosti. Slika 4.3 prikazuje kako je ukupni tok topline raspodijeljen među različitim skalama gibanja tako što su prikazani individualni 30-min MR kospektri te srednji kospektar za svaki mjerni nivo. Uočava se da pojedinačni kospektri značajno međusobno variraju. Premda većina kospektara upućuje na tok topline usmjeren prema tlu, postoje i periodi s uzlaznim tokom topline. Kako se povećava skala usrednjavanja MR kospektri pokazuju nepravilne varijacije što upućuje na utjecaj submezoskalnih gibanja na tok topline. Na svakoj od visina prisutan je negativni maksimum u kospektrima, nakon čega slijedi smanjenje magnitude toka i konvegencija ka konstantnoj vrijednosti ili promjena predznaka toka. Prema Vickersu i Mahrtu (2006), odgovarajuća turbulentna skala usrednjavanja je zadnja skala (gledajući uzastopno od malih prema velikim skalama) za koju MR kospektar ne mijenja predznak. Prema tome, na temelju rezultata za srednji MR kospektar odgovarajuća skala usrednjavanja bi trebala biti manja od 200 s.

Na temelju dobivenih rezultata u ovoj disertaciji je korištena vremenska skala od 100 s da bi se definirale turbulentne fluktuacije. Na ovaj način je umanjen mogući utjecaj submezoskalnih gibanja za jako stabilno stratificirane situacije. Vremenska skala od 100 s je korištena pri primjeni visoko-propusnog filtiranja originalnih vremenskih nizova komponenti brzine vjetra i sonične temperature. Budući da usrednjavanje preko dužih vremenskih perioda smanjuje tzv. slučajne pogreške (eng. *random errors*) u slučajevima kada vlada relativno stacionarna turbulencija, turbulentne varijance i kovarijance su određene korištenjem perioda od 30 min.

Valična analiza se razlikuje od drugih kvantitativnih analitičkih alata koji se uobičajeno koriste u analizi turbulentnih mjerenja (npr. Fourierova analiza) prevenstveno po tome što je to lokalna transformacija te se odvija za mnogo različitih skala (Salmond, 2005). Ovo omogućava dobivanje informacija o vremenskim lokacijama različitih značajki (koje su karakterizirane različitim frekvencijama) unutar skupa podataka. Na ovaj način valična analiza "zumira" određenu značajku signala i proučava je lokalno na razini detaljnosti koja odgovara skali te značajke. Valična analiza je primijenjena kako bismo dobili uvid u karakteristike turbulencije kao što su sporadičnost i vremenska varijabilnost dominantnih skala gibanja. Ti rezultati su prikazani na primjeru jedne cijele noći (slika 5.2).

Poglavlje 5: Lokalna teorija sličnosti iznad nehomogene podloge

Slika 5.2 prikazuje utjecaj nehomogene podloge koji se očituje u omjeru bezdimenzionalne varijance vertikalne komponente vjetra i odgovarajućih vrijednosti koje se koriste u relacijama teorije sličnosti za homogenu i ravnu podlogu, a koje su dane relacijom $\phi_w = 1.25(1 + 0.2\zeta)$ (Kaimal i Finnigan, 1994). Varijacije normirane vertikalne varijance vjetra sa smjerom vjetra odražavaju utjecaj nehomogene podloge. Da su i mjerenja iz Kutine iznad homogene i ravne podloge unutar prizemnog sloja, njihov omjer bi bio približno jednak jedinici. Umjesto toga, vidimo da je za većinu smjerova vjetra ovaj omjer manji od jedan za mjerenja na visini od 20 m, osim za vjetar iz smjerova 200–220 i 300–340 stupnjeva što odgovara podlozi velike hrapavosti ili pak dugog privjetrišta (eng. *fetch*). Za mjerenja na višim nivoima omjer je veći od jedan za vjetar iz smjerova 55–80, 170–230 i 300–360 stupnjeva dok je približno jednak jedan za smjerove označene sivom bojom. Stoga su odvojeno analizirane varijace komponenti vjetra za različite smjerove vjetra koji odgovaraju poremećenom i neporemećenom sektoru. Dakle, ukoliko je omjer ovih dviju funkcija sličnosti približno jednak jedinici, definirani su neporemećeni smjerovi vjetra (20–55, 85–175 i 235–295 stupnjeva), koji su označeni sivom bojom, dok se strujanje iz drugih smjerova vjetra smatra poremećenim.

Na slici 5.3 je prikazan rezultat analize za varijance svih triju komponenti vjetra na najnižem nivou i na visinama 2–5 odvojeno te je prikazana ovisnot o stabilnosti za poremećene i neporemećene sektore. Normirane varijance sve tri komponente vjetra na prvom mjerenom nivou manje ovise o smjeru vjetra u odnosu na više visine. To upućuje na lokalni utjecaj podsloja hrapavosti na mjerenja na toj visini, koji posljedično određuje statističke vrijednosti turbulencije. Vidimo da su vrijednosti veće za poremećeni sektor, te da je raspršenje veće na visinama 2–5. Puna krivulja označava funkciju sličnosti koja vrijedi u slučaju ravne i homogene podloge. Uočavamo da se mjerenja za neporemećene smjerove u sloju od 32–62 m mogu dobro opisati ovom funkcijom u rasponu stabilnosti do $\zeta = 1$. U jako stabilnom režimu kada je $\zeta > 1$, normirane varijance ne pokazuju linearnu ovisnost o stabilnosti već teže ka konstantnim vrijednostima, te ovo sugerira da bi *z-less* skaliranje trebalo vrijediti u jako stabilnoj situaciji. Ovo također ukazuje na to da je lokalno skaliranje prikladno i za izrazito nehomogenu podlogu, te da je lokalna Obukhovljeva duljina relevantna skala duljine.

Uzmemo li sumu varijanci komponenti vjetra, dobit ćemo TKE. Proučavat ćemo njenu ovisnost o paramteru stabilnosti ζ (slika 5.6). Procjena TKE je iznimno važna za atmosfersko numeričko modeliranje budući da se turbulentno miješanje

često parametrizira koristeći TKE. Vidimo da postoji linearna ovisnost normirane TKE o parametru stabilnosti za nivoe 2–5 (narančasta krivulja) dok su koeficijenti prilagodbe naravno drukčiji od onih za horizontalno homogenu podlogu prikazanu crnom crtkanom krivuljom. Najniži mjerni nivo je pod utjecajem elemenata hrapavosti te se ne može opisati prikazanom linearnom relacijom. To znači da u podsloju hrapavosti teorija sličnosti ne vrijedi. Osim toga, zbog utjecaja stabala u podsloju hrapavosti bezdimenzionalna TKE ima niže vrijednosti od vrijednosti za horizontalno homogenu i ravnu podlogu.

Jedna od važnijih funkcija u proučavanju graničnog sloja je funkcija sličnosti za bezdimenzionalni gradijent brzine vjetra koju označavamo s ϕ_m. Budući da su rezultati za varijance vjetra i normiranu TKE pokazali drukčije ponašanje na prvom mjernom nivou od nivoa 2–5, rezultati za ϕ_m su također prikazani zasebno za prvi i više nivoe (slika 5.8). Vidimo da su gotovo svi podaci na prvom nivou unutar područja stabilnosti od 0 do 0.5 (što odgovara slabo stabilnom sloju). Za ϕ_m ne uočavamo jasne razlike između prvog i viših mjernih nivoa što upućuje na to da karakteristike podloge utječu na jačinu turbulentnog miješanja i na gradijent brzine vjetra na podjednak način. Ovaj zaključak je dodatno potvrđen analizom za različite sektore vjetra, te je uočeno da ne postoji ovisnost o smjeru vjetra. Rezultati pokazuju sporiji rast ϕ_m funkcije s porastom stabilnosti nego što je predviđeno linearnom relacijom i naši podaci približno odgovaraju nelinearnoj relaciji koju su predložili Beljaars i Holtslag (1991). Linearna relacija koju je predlozio Dyer (1974) i nelinearna relacija prema Beljaarsu i Holtslagu se najčešće koriste za parametrizaciju u numeričkim modelima. Rezultati za ϕ_m upućuje na smanjenje bezimenzionalog gradijenta brzine vjetra za jako stabilno stratificirani sloj. Sličan rezultat je dobiven i u drugim studijama, međutim, ovaj rezultat dovodi u pitanje primjenjivost *z-less* skaliranja u jako stabilnom režimu. Ako je ϕ_m linearna funkcija parametra stabilnosti, onda gradijent brzine vjetra treba težiti ka konstantnoj vrijednosti za $\zeta \gg 1$. Stoga ovo odstupanje od linearnosti upućuje na neadekvatnost *z-less* skaliranja.

Grachev i sur. (2013) su klasificirali tradicionalni SBL u dva režima: podkritični i superkritični. Podjela je napravljena na temelju fluks Richardsonovog broja (Rf) koji predstavlja dinamičku mjeru stabilnosti strujanja i njegova kritična vrijednost u njihovom radu iznosi 0.25. U podkritičnom režimu turbulencija je kontinuirana, te teorija sličnosti vrijedi. Nadkritični režim je povezan sa sporadičnom turbulencijom male skale i to je tzv. ne-Kolmogorovljeva turbulencija. Slika 5.4 prikazuje ovisnost Rf o parametru stabilnosti. Dyerova parametrizacija, prikazana crnom krivuljom, predviđa asimptotsko približavanje k Rf=0.20, ali to značajno podcijenjuje vrijednosti Rf za jaku stabilnost, gdje one rastu iznad 0.25. Raspon stabilnosti u analiziranim podacima ide od 0 do 5, te je gotovo 50 % podataka na najviša dva nivoa imalo vrijednosti Rf-a veće od 0.25. Stoga vidimo da su najviši nivoi, koji

imaju i najveće stabilnosti, karakterizirani turbulencijom male skale.

Stoga je primijenjena klasifikacija kao u radu Gracheva i sur. (2013) koji su podijelili tradicionalni SBL u dva režima: subkritični i superkritični. Slijedeći nihov pristup, podaci sa svakog mjernog nivoa su podijeljeni u dva režima. Vidimo da u subkritičnom režimu, prikazanom zelenom bojom, ϕ_m sad slijedi linearnu ovisnost o parametru stabilnosti i koeficijent najbolje prilagodbe iznosi 3.8 (slika 5.9). To znači da *z-less* skaliranje vrijedi. Vidimo da bezdimenzionalni gradijent brzine vjetra u superkritičnom režimu pokazuje jako odstupanje od linearnosti u cijelom rasponu stabilnosti. Ovaj rezultat upućuje na to da je nelinearni izraz prema Beljaarsu i Holtslagu kao i rezultati drugih studija, koji pokazuju smanjene vrijednosti za jako stabilnu stratifikaciju, najvjerojatnije bio utjecan velikim brojem podataka koji su karakterizirani turbulencijom male skale i sporadinom turbulencijom.

Ha i sur. (2007) su ispitivali primjenjivost teorije sličnosti u prizemnom sloju za različite režime strujanja vjetra. Došli su do zaključka da premda je parametar stabilnosti inverzno koreliran sa srednjom brzinom vjetra, brzina strujanja na velikoj skali ima neovisan utjecaj na funkciju sličnosti ϕ_m. Pronašli su da za jaki i umjereni režim strujanja, teorija sličnosti vrijedi ukoliko je $\zeta << 1$, dok za slabi vjetar i jaku stratifikaciju ne vrijedi, odnosno, ϕ_m funkcija se ne može opisati postojećim funkcijama stabilnosti. Po uzoru na njihov pristup, ispitano je ponašanje ϕ_m funkcije za ova tri režima, s tim da je napravljena podjela i prema iznosu Rf (slika 5.10). Za kutinske podatke se ne uočava izrazita razlika u ponašanju ovog parametra za različite režime, a koju su ustanovili Ha i sur. (2007). Primjećujemo da je raspršenje najveće u slabom režimu strujanja, premda se znatno raspršenje vidi i za druga dva režima. Vidimo da raspršenje u svim režimima uzrokuje turbulencija male skale koja je preživjela u superkritičnom režimu. Ako pak gledamo samo podatke u podkritičnom režimu, oni imaju linearnu ovisnost te čak slijede Dyerovu krivulju. To znači da teorija sličnosti vrijedi čak i u slučaju slabog vjetra za čitav raspon stabilnosti.

I za kraj ćemo još vidjeti kakva je ovisnost funkcije ϕ_m/ϕ_w o parametru stabilnosti (slika 5.11). Ova nova funkcija predstavlja kombinaciju univerzalnih funkcija sličnosti, pa je stoga i sama funkcija sličnosti. Prednost u odnosu na prikazane funkcije sličnosti je da ona nije pod utjecajem samokorelacije. Do samokorelacije dolazi kada obje veličine dijele zajedničku varijablu. Kod proučavanja funkcija sličnosti brzina trenja je zajednička veličina. Vidimo da je rast ove funkcije s porastom stabilnosti sporiji nego što to predviđa linearna ovisnost, a budući da ova funkcija nema zajedničku varijablu s parametrom stabilnosti, onda možemo zaključiti da odstupanje od linearnosti nije uzrokovano samokorelacijom. Na slici 5.11(b) su prikazani samo podaci koji odgovaraju podkritičnom režimu, te je i ovdje odstupanje od linearnosti uzrokovano turbulencijom na maloj skali u superkritičnom

režimu. Kao što je već istaknuto, i ovdje se jasno uočava da podsloj hrapavosti značajnije utječe na funkciju sličnosti za varijance vjetra u odnosu na gradijent brzine vjetra, te stoga dovodi do precjenjivanja na prvom nivou, dok se na višim nivoima ne uočava nikakvo sustavno odstupanje.

Poglavlje 6: Turbulentni spektri, stopa disipacije i jednadžba ravnoteže turbulentne kinetičke energije

Spektri triju komponenti brzine vjetra su određeni primjenom brze Fourierove transformacije (FFT) na svaki od 30-min intervala kojem je prethodno uklonjen linearni trend. Stopa dissipacije TKE se određuje iz spektara primjenom inercijske disipacijske metode (eng. *inertial dissipation technique*). Ova metoda zahtijeva postojanje inercijalnog potpodručja u Fourierovim spektrima komponenti brzine vjetra. U inercijalnom potpodručju bi barem približno trebala vrijediti lokalna izotropija (eng. *local isotropy*). Lokalna izotropija zahtijeva da je omjer spektara lateralne i vertikalne komponente brzine vjetra u odnosu na longitudinalnu u inercijalnom području jednak 4/3, te da u ovom području spektri imaju $-5/3$ nagib. Prvi uvjet je jači iskaz postojanja lokalne izotropije u inercijalnom potpodručju.

Slika 6.2 prikazuje omjere S_v/S_u i S_w/S_u (prikazan je medijan svih spektara) za svaki od mjernih nivoa. Kao što se i očekuje prema teoriji, S_v/S_u pokazuje tenednciju konvergencije prema vrijednosti 4/3, dok je medijan omjera spektara S_w/S_u značajno manji od 4/3. Sličan rezultat za S_w/S_u je pronađen i u mnogim drugim studijama iznad šuma (Liu i sur., 2001; Su i sur., 2004) ili drugih kompleksnih površina (Roth i sur., 2006; Christen i sur., 2009; Večenaj i sur., 2011). Biltoft (2001) i Chamecki i Dias (2004) su dali razna objašnjenja za primjećeno odstupanje od lokalne izotropije.

Algoritam prema kojem je određena stopa disipacije TKE je prikazan na slici 6.3. Grachev i sur. (2014) su istaknuli da je 4/3 omjer između spektara horizontalnih komponenti brzine vjetra jači uvjet postojanja lokalne izotropije nego $-5/3$ nagib u spektrima, budući da se ovaj nagib može naći i kad ne postoji lokalna izotropija te je stoga ovaj uvjet korišten kod određivanja bezdimenzionalne funkcije sličnosti za disipaciju TKE (ϕ_ε). Slika 6.4 prikazuje ovisnost ϕ_ε o stabilnosti, te uočavamo sporiji porast ϕ_ε blizu vrha stabala (prvi nivo) u odnosu na rezultate dobivne u prizemnom sloju iznad manje hrapavih podloga. U graničnom slučaju neutralne stabilnosti vrijednosti $\phi_\varepsilon < 1$, što upućuje ne utjecaj podsloja hrapavosti, dok su na višim nivoima $\phi_\varepsilon > 1$ vjerojatno zbog utjecaja unutranjeg graničnog sloja. Nelinearna relacija koju su predložili Wyngaard i sur. (1971) bolje opisuje ovisnost ϕ_ε o stabilnosti, stoga je njihova funkija zajedno s nekoliko modifikacija prilagođena našim podacima te su

koeficijenti najbolje prilagodbe prikazani u Tablici 6.1, a krivulje za nivoe $2-5$ su prikazane na slici 6.5.

Nakon što je određena stopa disipacije TKE možemo proučavati karakteristike turbulentnih spektara. Prvo prikazujemo gustoću spektralne energije komponenti brzine vjetra pomnoženu s f i normiranu koristeći lokalne vrijednosti brzine trenja $u_{*\ell}^2$ (slika 6.7, lijevo). Uočavamo da lokalno skaliranje koristeći vrijednosti $u_{*\ell}$ i $z-d$ iznad šume nije prikladno budući da je prvi mjerni nivo očigledno unutral podsloja hrapavosti te spektralni maksimumi i inercijalno podpodručje ne koincidiraju na svim nivoima. Međutim, ako spektre normiramo koristeći brzinu vjetra mjerenu na prvom mjerenom nivou (blizu vrha elemenata hrapavosti) $U_{hc} = \langle \overline{u} \rangle_{hc}$ i visinu elemenata hrapavosti h_c, spektri pokazuju kolabiranje spektralnih maksimuma i inercijalnog podpodručja kroz cijeli sloj mjerenja (slika 6.7, desno). Podsloj hrapavosti je pod utjecajem velikih koherentnih vrtloga koji nastaju na vrhu elemenata hrapavosti (npr. Finnigan i Shaw, 2000; Shaw i sur., 2006). Ti veliki vrtlozi imaju skale duljine koje su proporcionalne h_c. Činjenica da se ovaj tip skaliranja može primijeniti i za mjerenja unutar prijelaznog sloja upućuje na to da ti veliki koherentni vrtlozi utječu na strukturu turbulencije do znatne visine.

U idućem koraku je testirana primjenjivost spektralnih modela izvedenih za horizontalno homogen i ravan teren. Kao prvi model testiran je onaj koji su predložili Kaimal i sur. (1972), a koji prikazuje svojstva turbulentnih spektara u prizemnom sloju. Spektri komponenti brzine vjetra su normirani koristeći lokalne vrijednosti brzine trenja i bezdimenzionalne funkcije sličnosti disipacije TKE (slika 6.9). Vrijednosti ϕ_ε određene na temelju horizontalnih komponenti brzine vjetra su korištene i za normiranje spektra vertikalne komponente. Norimirani spekri komponenti brzine vjetra su prikazani i za sedam različitih kategorija stabilnosti (tablica 6.2) te je prikazan median svih spektara za pojedinu kategoriju. Ovisnost spektara o stabilnosti je prikazana odvojeno za mjerenja na prvom nivou i mjerenja s viših nivoa. Ovi normirani spektri pokazuju da za horizontalne komponente brzine postoji $-2/3$ nagib za veliki raspon frekvencija unutar inercijalnog potpodručja. Također, sve komponente strujanja pokazuju jasno razdvajanje u ovisnosti o parametru stabilnosti: s povećanjem stabilnosti smanjuje se intenzitet spektralnog maksimuma te je on pomaknut k višim frekvencijama. Primjećeno je da spektri vertikalne komponente brzine imaju manje vrijednosti u inercijalnom potpodručju u odnosu na neutralne spektre mjerene u Kansasu. Magnitude vertikalnih spektara su za većinu kategorija stabilnosti za mjerenja na nivou 1 i nivoima $2-5$ za faktor 2 manje u odnosu na vrijednosti dobivene iznad HHF. Pokazalo se da je ovo uzrokovano korištenjem ϕ_ε funkcije koja je određena na temelju horizontalnih komponenti brzine, a čije su vrijednosti veće nego kad ϕ_ε procijenimo koristeći samo vertikalne spektre (ϕ_{ε_w}, slika 6.11). Zaista, ako koristimo ϕ_{ε_w} u normiranju vertikalnih spektara dobije se dobro

slaganje ne samo u obliku već i u magnitudi sa spektrima koje su predložili Kaimal i sur. (1972).

Za modeliranje spektara u SBL-u se može koristiti i model koji su predložili Olesen i sur. (1984) i prikazan je jednadžbama (2.41) – (2.43). Ovaj model se temelji na pretpostavci da je bezdimenzionalna frekvencija koja odgovara maksimumu spektralne energije funkcija parametra stabilnosti te bi stoga svi spektralni maksimumi trebali koincidirati ako se spektar energije prikaže kao funcija n/ϕ_m. Primjenjujući ovaj model na naše podatke nađeno je da spektralne krivulje s različitih mjernih nivoa te za različite klase stabilnosti približno koncidiraju. Relacije najbolje prilagodbe ovog modela na kutinske podatke su dane izrazima (6.7)–(6.9). Rezultati upućuju na to da se ovaj model može uspješno primijeniti i za spektre brzine u SBL-u iznad nehomogene podloge. Čini se da je ovaj model prikladniji za spektre u SBL-u iznad nehomogene podloge od Kaimalovog (neutralnog) modela, međutim, da bi se ovaj model mogao primijeniti potrebno je poznavati bezdimenzionalne funkcije za smicanje brzine vjetra i disipaciju TKE.

Za kraj su procijenjeni članovi u jednadžbi ravnoteže TKE. Slika 6.19 prikazuje procijenjene bezdimenzionalne članove unutar podsloja hrapavosti i prijelaznog sloja. Za svaki od članova prikazane su i empirijske relacije. Kao što i očekujemo u SBL-u, dominantni članovi su mehanička produkcija i disipacija TKE. Rezidualni član ima slične vrijednosti (uglavnom unutar prijelaznog sloja), ali on predstavlja sumu tri člana: turbulentnog transporta, transoprta tlakom i advekciju. Li i sur. (2008) su definirali bezimenzionalnu funkciju lokalne neravnoteže $\phi_{LI} = -\phi_m + \zeta + \phi_\varepsilon$, koja u ovom slučaju odgovara rezidualnom članu. U prijalaznom sloju lokalni gubici TKE, $\zeta + \phi_\varepsilon$, su veći od lokalne produkcije smicanjem, što rezultira pozitivnim rezidualnim članom koji upućuje na dobitak TKE u ovom sloju. Ova lokalna neravnoteža TKE za cijeli raspon stabilnosti je uočena i u mnogim drugim studijama (npr. Högström, 1990; Frenzen i Vogel, 2001; Li i sur., 2008; Duarte i sur., 2015). Li i sur. (2008) su predložili nelokalne dinamičke procese kao glavni mehanizam koji uzrokuje tu neravnotežu, dok je Högström (1990) predložio teoriju neaktivne turbulencije kako bi objasnio dobitak TKE u prozemnom sloju, a koji je uglavnom povezan s viškom disipacije. U uvjetima kada je podloga iznad koje se mjeri horizontalno homogena i ravna, gdje se advekcija TKE može zanemariti, ovaj dobitak TKE se često pripisuje članu prijenosa tlakom (Högström, 1990; Duarte i sur., 2015). Unutar posloja hrapavosti, produkcija TKE smicanjem je veća nego destrukcija uzgonom i disipacijom TKE, što upućuje na gubitak energije u ovom sloju za raspon stabilnosti do $\zeta = 0.1$. Za veće stabilnosti rezidualni član mijenja predznak i postaje dobitak TKE u ovom sloju. Turbulentni transport TKE se smatra glavnim uzrokom naglašene neravnoteže između produkcije i disipacije TKE u podsloju hrapavosti u neutralnim uvjetima iznad vegetacijom prekrivenih podloga (Mammarella i sur.,

2008).

Zaključak

Rezultati pokazuju da se lokalna teorija sličnosti može primijeniti i za područja s izrazito nehomogenom podlogom, ali odgovarajuće bezdimenzionalne funkcije imaju drugačije vrijednosti u odnosu na one pronađene za horizontalno homogene podloge. Pronađeno je da funkcije sličnosti za gradijent vjetra i varijance komponenti brzine vjetra imaju drugačiji odziv zbog nehomogenosti podloge. Utjecaj podsloja hrapavosti je jači nego utjecaj nehomogene podloge, dok je ovaj utjecaj najslabiji za gradijent brzine vjetra. Osim toga, funkcija sličnosti za gradijente vjetra pokazuje sličnu podjelu turbulencije u pod- i nadkritičnom režimu kao što je opaženo i iznad idealnih homogenih podloga. Za subkritični režim, ali i za sve opažene uvjete, podaci dosta dobro slijede odgovarajuće funkcije dane u literaturi. U subkritičnom režimu bezdimenzionalno smicanje vjetra pokazuje linearnu ovisnost o parametru stabilnosti, što upućuje na to da su odstupanja od linearnosti uglavnom uzrokovana turbulencijom na maloj skali, a ne nehomogenošću podloge.

Daljnja istraživanja su se fokusirala na utjecaj nehomogene podloge na spektralne karakteristike turbulencije te stopu disipacije TKE (ε) i jednadžbu ravnoteže TKE. Pronađeno je da lokalno skaliranje za spektre koristeći u_* i $z - d$ ne vrijedi iznad hrapave podloge karakterizirane visokom vegetacijom. Umjesto toga, turbulentni spektri snage komponenti brzine normirani odgovarajućim varijancama, te koristeći brzinu vjetra mjerenu blizu vrha elemenata hrapavosti i njihovu visinu, tzv. canopy skaliranje (skaliranje pokrova), dovodi do koincidiranja spektara sa svih visina te se oni mogu prikazati kao jedna krivulja. Činjenica da (canopy) skaliranje pokrova u prijelaznom sloju daje bolje rezultate od tradicionalnog skaliranja koje vrijedi u prizemnom sloju, upućuje na to da veliki koherentni vrtlozi, koji se stvaraju na vrhovima stabala, dominiraju turbulentnom strukturom sve do značajne visine koja je i tri puta veća od visine stabala.

Na prvom mjernom nivou bezdimenzionalna funkcija za disipaciju TKE (ϕ_ε) je pod značajnim utjecajem elemenata hrapavosti, dok se na višim mjernim nivoima njena ovisnost o stabilnosti može opisati modificiranim oblikom funkcije koju su predložili Wyngaard i sur. (1971). Ovaj modificirani oblik se koristi kako bi se uzelo u obzir odstupanje od lokalne ravnoteže u statički neutralnim uvjetima.

Hipoteza o lokalnoj izotropiji nije zadovoljena za ovo kompleksno mjerno mjesto. Zbog smanjene spektralne snage za vertikalnu komponentu brzine vjetra u odnosu na horizontalne komponente brzine, vrijednosti stope disipacije TKE određene na temelju mjerenja vertikalne brzine su značajno manje u odnosu na vrijednosti određene iz horizontalnih komponenti. Pokazalo se da ovaj rezultat ima značajne

posljedice na odgovarajuće jednadžbe za budžete varijanci brzine i TKE, te za uspješnu primjenu i dobro slaganje s naširoko primjenjivanim spektralnim modelima na temelju mjerenja u Kansasu, SAD. Stoga je bilo potrebno normirati spektre vertikalne komponente brzine koristeći ϕ_{ε_w} da bismo dobili dobro slaganje spektara u obliku i magnitudi s Kaimalovim spektrima. Isto je uočeno i kod primjene Olesenovog spektralnog modela. Ovo upućuje na to da se lokalna izotropija može pronaći jedino u istinski homogenom strujanju (Wyngaard, 2010), a to uglavnom ne vrijedi za strujanja u vertikalnom smjeru, a još manje za strujanje iznad nehomogene površine poput šuma ili u urbanom graničnom sloju. Spektralni model koji su predložili Olesen i sur. (1984) po prvi put je primijenjen na mjerenja iznad nehomogene podloge i pokazao se uspješnim.

Lokalna ravnoteža između produkcije i destrukcije TKE je narušena, a to upućuje na činjenicu da je doprinos članova transporta i advekcije u jednadžbi ravnoteže TKE važan. U prijelaznom sloju ukupni gubitak TKE je veći od produkcije TKE smicanjem zbog čega je rezidualni član pozitivan i predstavlja dobitak TKE u ovom sloju. Unutar podsloja hrapavosti, u rasponu stabilnosti do $\zeta = 0.1$ produkcija je veća od uzgonske destrukcije i disipacije TKE te rezidualni član predstavlja gubitak energije. Za veće stabilnosti rezidualni član mijenja znak i postaje dobitak TKE u tom sloju. Nelokalni dinamički procesi se smatraju glavnim razlozima neravnoteže TKE u prijelaznom sloju kao i za narušavanje $z - less$ režima u statički jako stabilnim uvjetima. Turbulentni transport TKE iznad površina pokrivenih visokom vegetacijom se smatra odgovornim za neravnotežu u podsloju hrapavosti u neutralnim uvjetima.

Bibliography

Acevedo, O. C., O. L. L. Moraes, R. da Silva, V. Anabor, D. P. Bittencourt, H. R. Zimmermann, R. O. Magnago, and G. A. Degrazia, 2008: Surface-to-atmosphere exchange in a river valley environment. *J Appl Meteorol Climatol*, **46 (8)**, 1169–1181.

Agrawal, S. K., 1997: *Fluid Mechanics and Machinery*. McGraw-Hill, New Delhi, 669 pp.

Amiro, B., 1990: Drag coefficients and turbulence spectra within three boreal forest canopies. *Boundary-Layer Meteorol*, **52**, 227–246.

Anderson, D., S. Verma, and R. Clement, 1986: Turbulence spectra of CO2, water vapour, temperature and velocity over a deciduous forest. *Agric For Meteorol*, **38**, 81–99.

Andreas, E. L., R. J. Hill, J. R. Gosz, D. I. Moore, W. D. Otto, and A. D. Sarma, 1998: Statistics of surface-layer turbulence over terrain with metre-scale heterogeneity. *Boundary-Layer Meteorol*, **86 (3)**, 379–408, doi:10.1023/A:1000609131683.

Antonia, R. A., and M. R. Raupach, 1993: Spectral scaling in a high Reynolds number laboratory boundary layer. *Boundary-Layer Meteorol*, **65**, 289–306.

Aubinet, M., T. Vesala, and D. Papale, 2012: *Eddy Covariance: A Practical Guide to Measurement and Data Analysis*. Springer, 438 pp.

Baas, P., J. G. Steeneveld, H. J. B. van de Wiel, and M. A. A. Holtslag, 2006: Exploring self-correlation in flux-gradient relationships for stably stratified conditions. *J Atmos Sci*, **63 (11)**, 3045–3054, doi:10.1175/JAS3778.1.

Babić, K., Z. B. Klaić, and Ž. Večenaj, 2012: Determining a turbulence averaging time scale by Fourier analysis for the nocturnal boundary layer. *Geofizika*, **29 (1)**, 35–51.

Babić, K., M. W. Rotach, and Z. B. Klaić, 2016a: Evaluation of local similarity theory in the wintertime nocturnal boundary layer over heterogeneous surface. *Agric For Meteorol*, **128**, 164–179, doi:10.1016/j.agrformet.2016.07.002.

Babić, N., Ž. Večenaj, and S. F. J. De Wekker, 2016b: Flux-variance similarity in complex terrain and its sensitivity to different methods to treat non-stationarity. *Boundary-Layer Meteorol*, **159**, 123145, doi:10.1007/s10546-015-0110-0.

Baklanov, A. A., and Coauthors, 2011: The nature, theory, and modeling of atmospheric planetary boundary layers. *Bull Amer Meteorol Soc*, **92 (2)**, 123–128, doi:10.1175/2010BAMS2797.1.

Baldocchi, D., and T. Meyers, 1988: A spectral and lag-correction analysis of turbulence in a deciduous forest canopy. *Boundary-Layer Meteorol*, **45**, 31–58.

Banta, R., Y. Pichugina, and W. Brewer, 2006: Turbulent velocity-variance profiles in the stable boundary layer generated by a nocturnal low-level jet. *J Atmos Sci*, **63**, 2700–2719.

Barthlott, C., P. Drobinski, C. Fesquet, T. Dubos, and C. Pietras, 2007: Long-term study of coherent structures in the atmospheric surface layer. *Boundary-Layer Meteorol*, **125**, 1–24, doi:10.1007/s10546-007-9190-9.

Basu, S., F. Porté-Agel, E. Foufoula-Georgiou, J. Vinuesa, and M. Pahlow, 2006: Revisiting the local scaling hypothesis in stably stratified atmospheric boundary-layer turbulence: an integration of field and laboratory measurements with large-eddy simulations. *Boundary-Layer Meteorol*, **119 (3)**, 473–500, doi:10.1007/s10546-005-9036-2.

Beljaars, A. C., and M. A. A. Holtslag, 1991: Flux parameterization over land surfaces for atmospheric models. *J Appl Meteor*, **30**, 327–341, doi:10.1175/1520-0450(1991)030⟨0327:FPOLSF⟩2.0.CO;2.

Biltoft, C., 2001: Some thoughts on local isotropy and the 4/3 lateral to longitudinal velocity spectrum ratio. *Boundary-Layer Meteorol*, **100**, 393–404.

Bosveld, F., 1997: Derivation of fluxes from profiles over a moderately homogeneous forest. *Boundary-Layer Meteorol*, **84 (3)**, 289–327, doi:10.1023/A:1000453629876.

Bou-Zeid, E., C. Meneveau, and M. B. Parlange, 2004: Large-eddy simulation of neutral atmospheric boundary layer flow over heterogeneous surfaces: Blending height and effective surface roughness. *Water Resour Res*, **40**, W02 505, doi:10.1029/2003WR002475.

Bou-Zeid, E., M. B. Parlange, and C. Meneveau, 2007: On the parameterization of surface roughness at regional scales. *J Atmos Sci*, **64**, 216–227, doi:10.1175/JAS3826.1.

Bradshaw, P., 1967: inactive motion and pressure fluctuations in turbulent boundary layers. *J fluid Mech*, **30 (2)**, 241–258, doi:10.1017/S0022112067001417.

Brunet, Y., J. Finnigan, and M. Raupach, 1994: A wind tunel study of air flow in waving wheat: single point velocity statistics. *Boundary-layer Meteorol*, **70**, 95–132.

Businger, J., J. Wyngaard, Y. Izumi, and E. Bradley, 1971: Flux-profile relationships in the atmospheric surface layer. *J Atmos Sci*, **28**, 181–189, doi:10.1175/1520-0469(1971)028⟨0181:FPRITA⟩2.0.CO;2.

Chamecki, M., and N. Dias, 2004: The local isotropy hypothesis and the turbulent kinetic energy dissipation rate in the atmospheric surface layer. *Q J R Meteorol Soc*, **130**, 2733–2752, doi:10.1256/qj.03.155.

Champagne, F. H., 1978: The finescale structure of the turbulent velocity field. *J Fluid Mech*, **86**, 67–108.

Cheng, H., and I. Castro, 2002: Near-wall flow developments after a step change in surface roughness. *Boundary-Layer Meteorol*, **105 (3)**, 411–432, doi:10.1023/A:1020355306788.

Cheng, Y., and W. Brutsaert, 2005: Flux-profile relationships for wind speed and temperature in the stable atmospheric boundary layer. *Boundary-Layer Meteorol*, **114 (3)**, 519–538, doi:10.1007/s10546-004-1425-4.

Cheng, Y., M. B. Parlange, and W. Brutsaert, 2005: Pathology of Monin-Obukhov similarity in the stable boundary layer. *J Geophys Res*, **110**, D06 101, doi:10.1029/2004JD004923.

Christen, A., M. W. Rotach, and R. Vogt, 2009: The budget of turbulent kinetic energy in the urban roughness sublayer. *Boundary-Layer Meteorol*, **131 (2)**, 193–222, doi:10.1007/s10546-009-9359-5.

Conangla, L., J. Cuxart, and M. R. Soler, 2008: Characterisation of the nocturnal boundary layer at a site in Northern Spain. *Boundary-Layer Meteorol*, **128 (2)**, 255–276, doi:10.1007/s10546-008-9280-3.

Cuxart, J., M. Jimenez, and D. Martinez, 2007: Nocturnal mesobeta basin and katabatic flows on a midlatitude island. *Mon Wea Rev*, **135 (3)**, 918–932.

Cuxart, J., G. Morales, E. Terradellas, and C. Yagüe, 2002: Study of coherent structures and estimation of the pressure transport terms for the nocturnal stable boundary layer. *Boundary-Layer Meteorol*, **105 (2)**, 305–328.

Daubechies, I., 1992: *Ten Lectures on Wavelets*. Society for Industrial and Applied Mathematics, 357 pp.

de Franceschi, M., D. Zardi, M. Tagliazucca, and F. Tampieri, 2009: Analysis of second-order moments in surface layer turbulence in an Alpine valley. *Q J R Meteorol Soc*, **135**, 1750–1765, doi:10.1002/qj.506.

Dellwik, E., and O. N. Jensen, 2005: Flux-profile relationships over a fetch limited beech forest. *Boundary-Layer Meteorol*, **115 (2)**, 179–204, doi:10.1007/s10546-004-3808-y.

Derbyshire, H., 1995: Stable boundary layers: Observations, models and variability part I: Modelling and measurements. *Boundary-Layer Meteorol*, **74 (1-2)**, 19–54, doi:10.1007/BF00715709.

Desjardins, R., J. Macpherson, P. Schuepp, and F. Karanja, 1989: An evaluation of aircraft flux measurements of CO2, water wapor and sensible heat. *Boundary-Layer Meteorol*, **47**, 55–59.

Duarte, H. F., M. Y. Leclerc, G. Zhang, D. Durden, R. Kurzeja, M. Parker, and D. Werth, 2015: Impact of nocturnal low-level jets on near-surface turbulence kinetic energy. *Boundary-Layer Meteorol*, **156**, 349–370, doi:10.1007/s10546-015-0030-z.

Dwyer, M. J., E. G. Patton, and R. H. Shaw, 1997: Turbulent kinetic energy budgets from a large-eddy simulation of airflow above and within a forest canopy. *Boundary-Layer Meteorol*, **84**, 23–43.

Dyer, A. J., 1974: A review of flux-profile relationships. *Boundary-Layer Meteorol*, **7 (3)**, 363–372, doi:10.1007/BF00240838.

Enger, L., and D. Koračin, 1995: Simulations of dispersion in complex terrain using a higher-order closure model. *Atmospheric Environment*, **29 (18)**, 2449 – 2465.

Farge, M., 1992: Wavelet transforms and their applications to turbulence. *Ann Rev Fluid Mech*, **24**, 395–457, doi:10.1146/annurev.fluid.24.1.395.

Finnigan, J., 1979: Turbulence in waveing wheat. I. mean statistics and honami. doi: 10.1007/BF02350511.

Finnigan, J., 2000: Turbulence in plant canopies. *Annu Rev Fluid Mech*, **32**, 519–571, doi:10.1146/annurev.fluid.32.1.519.

Finnigan, J., and R. Shaw, 2000: A wind-tunnel study of airflow in waveing wheat: an EOF analysis of the structure of the large-eddy motion. *Boundary-Layer Meteorol*, **96**, 211–255, doi:10.1023/A:1002618621171.

Foken, T., 2008: *Micrometeorology*. Springer-Verlag Berlin Heidelberg, 320 pp.

Foken, T., and B. Wichura, 1996: Tools for quality assessment of surface-based flux measurements. *Agric For Meteorol*, **78 (1-2)**, 83–105, doi:10.1016/0168-1923(95)02248-1.

Foken, T., F. Wimmer, M. Mauder, C. Thomas, and C. Liebethal, 2006: Some aspects of the energy balance closure problem. *Atmos Chem Phys*, **6**, 4395–4402.

Forrer, J., 1999: The structure and turbulence characteristics of the stable boundary layer over the Greenland ice sheet. Dissertation, ETHZ, Switzerland, 132 pp.

Forrer, J., and M. W. Rotach, 1997: On the turbulence structure in the stable boundary layer over the Greenland ice sheet. *Boundary-Layer Meteorol*, **85 (1)**, 111–136, doi: 10.1023/A:1000466827210.

Fortuniak, K., and W. Pawlak, 2015: Selected spectral characteristics of turbulence over an urbanized area in the centre of Łódź, Poland. *Boundary-Layer Meteorol*, **145**, 137–156, doi:10.1007/s10546-014-9966-7.

Fortuniak, K., W. Pawlak, and M. Siedlecki, 2013: Integral turbulence statistics over a central european city centre. *Boundary-Layer Meteorol*, **146**, 257–276, doi:10.1007/s10546-012-9762-1.

Frenzen, P., and C. Vogel, 2001: Further studies of atmospheric turbulence in layer near the surface: scaling the TKE budget above the roughness sublayer. *Boundary-Layer Meteorol*, **99**, 173–206.

Fritts, D., C. Nappo, D. Riggin, B. Balsley, W. Eichinger, and R. Newsom, 2003: Analysis of ducted motions in the stable boundary layer during CASES-99. *J Atmos Sci*, **60**, 2450–2472.

Garratt, J., 1972: Studies of turbulence in the surface layer over water (Lough Neagh). Part II. Production and dissipation of velocity and temperature fluctuations. *Quart J Roy Meteorol Soc*, **98**, 642–657, doi:10.1002/qj.49709841712.

Grachev, A. A., L. E. Andeas, W. C. Fairall, S. P. Guest, and P. O. G. Persson, 2007: SHEBA flux-profile relationships in the stable atmospheric boundary layer. *Boundary-Layer Meteorol*, **124**, 315–333, doi:10.1007/s10546-007-9177-6.

Grachev, A. A., L. E. Andeas, W. C. Fairall, S. P. Guest, and P. O. G. Persson, 2013: The critical Richardson number and limits of applicability of local similarity theory in the stable boundary layer. *Boundary-Layer Meteorol*, **147**, 51–82, doi:10.1007/s10546-012-9771-0.

Grachev, A. A., L. E. Andeas, W. C. Fairall, S. P. Guest, and P. O. G. Persson, 2014: Similarity theory based on the Dougherty-Ozmidov length scale. *Q J R Meteorol Soc*, **141**, 1845–1856, doi:10.1002/qj.2488.

Grachev, A. A., W. C. Fairall, P. O. G. Persson, L. E. Andeas, and S. P. Guest, 2005: Stable boundary-layer scaling regimes: The Sheba data. *Boundary-Layer Meteorol*, **116**, 201–235, doi:10.1007/s10546-004-2729-0.

Güttler, I., Č. Branković, T. A. O'Brien, E. Coppola, B. Grisogono, and F. Giorgi, 2014: Sensitivity of the regional climate model RegCM4.2 to planetary boundary layer parameterisation. *Climate Dyn*, **43 (7)**, 1753–1772, doi:10.1007/s00382-013-2003-6.

Ha, K.-J., Y.-K. Hyun, H.-M. Oh, K.-E. Kim, and L. Mahrt, 2007: Evaluation of boundary layer similarity theory for stable conditions in CASES-99. *Mon Weath Rev*, **135**, 3474–3483, doi:10.1175/MWR3488.1.

Harman, I., and J. Finnigan, 2007: A simple unified theory for flow in the canopy and roughness sublayer. *Boundary-Layer Meteorol*, **123**, 339–363, doi:10.1007/s10546-006-9145-6.

Hartogensis, O. K., and R. H. A. De Bruin, 2005: Monin–Obukhov similarity functions of the structure parameter of temperature and turbulent kinetic energy dissipation rate in the stable boundary layer. *Boundary-Layer Meteorol*, **116 (2)**, 253–276, doi:10.1007/s10546-004-2817-1.

Heinemann, G., 2004: Local similarity properties of the continuously turbulent stable boundary layer over Greenland. *Boundary-Layer Meteorol*, **112 (2)**, 283–305, doi:10.1023/B:BOUN.0000027908.19080.b7.

Hicks, B., 1978: Some limitations of dimensional analysis and power laws. *Boundary-Layer Meteorol*, **14 (4)**, 567–569, doi:10.1007/BF00121895.

Högström, U., 1988: Non-dimensional wind and temperature profiles in the atmospheric surface layer: A re-evaluation. *Boundary-Layer Meteorol*, **42**, 55–78, doi:10.1007/BF00119875.

Högström, U., 1990: Analysis of turbulence structure in the surface layer with a modified similarity formulation for near neutral conditions. *J Atmos Sci*, **47**, 1949–1972.

Högström, U., 1996: Review of some basic characteristics of the atmospheric surface layer. *Boundary-Layer Meteorol*, **78**, 215–246.

Högström, U., H. Bergström, A. Smedman, S. Halldin, and A. Lindroth, 1989: Turbulent exchange above a pine forest I: Fluxes and gradients. *Boundary-Layer Meteorol*, **49**, 197–217, doi:10.1007/BF00116411.

Högström, U., J. Hunt, and A. Smedman, 2002: Theory and measurements for turbulence spectra and variances in the atmospheric neutral surface layer. *Boundary-Layer Meteorol*, **103**, 101–124.

Holtslag, A., and H. de Bruin, 1988: Applied modeling of the nighttime surface energy balance over land. *J Appl Meteorol*, **27**, 689–704.

Holtslag, A., and F. Nieuwstadt, 1986: Scaling the atmospheric boundary layer. *Boundary-Layer Meteorol*, **36**, 201–209, doi:10.1007/BF00117468.

Horvath, K., D. Koračin, R. Vellore, J. Jiang, and R. Belu, 2012: Sub-kilometer dynamical downscaling of near-surface winds in complex terrain using wrf and mm5 mesoscale models. *J Geophys Res: Atmos*, **117 (D11)**, doi:10.1029/2012JD017432, d11111.

Howell, J. F., and L. Mahrt, 1997: Multiresolution Flux Decomposition. *Boundary-Layer Meteorol*, **83**, 117–137, doi:10.1023/A:1000210427798.

Howell, J. F., and J. Sun, 1999: Surface-layer fluxes in stable conditions. *Boundary-Layer Meteorol*, **90 (3)**, 495–520, doi:10.1023/A:1001788515355.

Kaimal, J. C., 1973: Turbulence spectra, length scales and structure parameters in the stable boundary layer. *Boundary-Layer Meteorol*, **4**, 289–309, doi:10.1007/BF02265239.

Kaimal, J. C., and J. J. Finnigan, 1994: *Atmospheric boundary layer flows: their structure and measurements*. University Press, New York, 289 pp.

Kaimal, J. C., and J. Wyngaard, 1990: The Kansas and Minesota experiments. *Boundary-Layer Meteorol*, **50**, 31–47, doi:10.1007/BF00120517.

Kaimal, J. C., J. C. Wyngaard, D. A. Haugen, O. R. Coté, Y. Izumi, S. J. Caughey, and C. J. Readings, 1976: Turbulence structure in the convective boundary layer. *J Atmos Sci*, **33 (11)**, 2152–2169, doi:10.1175/1520-0469(1976)033⟨2152:TSITCB⟩2.0.CO;2.

Kaimal, J. C., J. C. Wyngaard, Y. Izumi, and O. Coté, 1972: Spectral characteristics of surface-layer turbulence. *Q J R Meteorol Soc*, **98**, 563–589, doi:10.1002/qj.49709841707.

Katul, G., S. M. Goltz, C. Hsieh, Y. Cheng, F. Mowry, and J. Sigmon, 1995: Estimation of surface heat and momentum fluxes using the flux-variance method above uniform and non-uniform terrain. *Boundary-Layer Meteorol*, **74 (3)**, 237–260, doi:10.1007/BF00712120.

Katul, G., and Coauthors, 1999: Spatial variability of turbulent fluxes in the roughness sublayer of an even-aged pine forest. *Boundary-Layer Meteorol*, **93**, 1–28, doi:10.1023/A:1002079602069.

Klipp, C. J., and L. Mahrt, 2004: Flux-gradient relationship, self-correlation and intermittency in the stable boundary layer. *Q J R Meteorol Soc*, **130 (601)**, 2087–2103, doi:10.1256/qj.03.161.

Kljun, N., P. Calanca, M. W. Rotach, and H. P. Schmid, 2015: A simple two-dimensional parameterisation for flux footprint prediction (FFP). *Geoscientific Model Development*, **8 (11)**, 3695–3713, doi:10.5194/gmd-8-3695-2015.

Kolmogorov, A. N., 1941: The local structure of turbulence in incompressible viscous fluid for very large Reynolds numbers. *Proceedings of the USSR Academy of Sciences (in Russian) 30: 299–303. Translated into English: Proceedings of the Royal Society (1991)*, **A 434**, 9–13.

Koračin, D., and L. Enger, 1994: A numerical study of boundary-layer dynamics in a mountain valley. *Boundary-Layer Meteorology*, **69 (3)**, 249–283, doi:10.1007/BF00708858.

Kral, S. T., A. Sjöblom, and T. Nygård, 2014: Observations of summer turbulent surface fluxes in a High Arctic fjord. *Q J R Meteorol Soc*, **140**, 666–675, doi:10.1002/qj.2167.

Kristensen, L., 1998: Time series analysis: Dealing with imperfect data. Tech. report I-12289, Riso National Laboratory, Roskilde, Denmark.

Lau, K.-M., and H. Weng, 1995: Climate signal detection using wavelet transform: How to make a time series sing. *Bull Amer Meteorol Soc*, **76**, 2391–2402.

Leclerc, M. Y., K. C. Beissner, R. Shaw, G. den Hartog, and H. H. Neumann, 1990: The influence of atmospheric stability on the budgets of the Reynolds stress and turbulent kinetic energy within and above a deciduous forest. *J Appl Meteorol*, **29**, 916–933.

Lee, X., 1996: Turbulence spectra and eddy difusivity over forests. *J App Meteorol*, **35**, 1307–1318.

Lenschow, D., J. Mann, and L. Kristensen, 1994: How long is long enough when measuring fluxes and other turbulent statistics? *J Atmos Oceanic Tech*, **11**, 661–673.

Li, X., N. Zimmerman, and M. Princevac, 2008: Local imbalance of turbulent kinetic energy in the surface layer. *Boundary-Layer Meteorol*, **129**, 115–136, doi:10.1007/s10546-008-9304-z.

Liang, J., L. Zhang, Y. Wang, X. Cao, Q. Zhang, H. Wang, and B. Zhang, 2014: Turbulence regimes and the validity of similarity theory in the stable boundary layer over complex terrain of the Loess Plateau, China. *J Geophys Res Atmos*, **119**, 6009–6021, doi:10.1002/2014JD021510.

Liu, S., and Coauthors, 2001: Turbulence spectra and dissipation rates above and within a forest canopy. *Boundary-Layer Meteorol*, **98 (1)**, 83–102, doi:10.1023/A:1018715812229.

Liu, Y., X. Liang, and R. Weisberg, 2007: Rectification of the bias in the wavelet power spectrum. *J Atmos Oceanic Tech*, **24**, 2093–2102, doi:10.1175/2007JTECHO511.1.

Lumley, J., and H. A. Panofsky, 1964: *The structure of atmospheric turbulence*. John Wiley and Sons: New York, 239 pp.

Mahrt, L., 1998: Stratified atmospheric boundary layers and breakdown of models. *Theoret Comput Fluid Dynamics*, **11**, 263–279.

Mahrt, L., 1999: Stratified atmospferic boundary layers. *Boundary-Layer Meteorol*, **90 (3)**, 375–396, doi:10.1023/A:1001765727956.

Mahrt, L., 2000: Surface heterogeneity and vertical structure of the boundary layer. *Boundary-Layer Meteorol*, **96 (1-2)**, 33–62, doi:10.1023/A:1002482332477.

Mahrt, L., 2007: The influence of nonstationarity on the turbulent flux-gradient relationship for stable stratification. *Boundary-Layer Meteorol*, **125**, 245264, doi:10.1007/s10546-007-9154-0.

Mahrt, L., 2011: The near-calm stable boundary layer. *Boundary-Layer Meteorol*, **140**, 343–360, doi:10.1016/s10546-011-9616-2.

Mahrt, L., 2014: Stably stratified atmospheric boundary layers. *Annu Rev Fluid Mech*, **46**, 23–45, doi:10.1146/annurev-fluid-010313-141354.

Mahrt, L., C. Thomas, S. Richardson, N. Seaman, D. Stauffer, and M. Zeeman, 2013: Non-stationary generation of weak turbulence for very stable and weak-wind conditions. *Boundary-Layer Meteorol*, **147**, 179–199, doi:10.1007/s10546-012-9782-x.

Mahrt, L., D. Vickers, P. Frederickson, K. Davidson, and A.-S. Smedman, 2003: Sea-surface aerodynamic roughness. *J Geophys Res*, **108(C6)**, 3171, doi:10.1029/2002JC001383.

Mahrt, L., D. Vickers., R. Nakamura, M. R. Soler, J. Sun, S. Burns, and D. H. Lenschow, 2001: Shallow drainage flows. *Boundary-Layer Meteorol*, **101 (0)**, 242–260.

Malhi, Y., 1996: The behaviour of the roughness length for temperature over heterogeneous surfaces. *Q J R Meteorol Soc*, **122 (533)**, 1095–1125, doi:10.1002/qj.49712253305.

Mammarella, I., E. Dellwik, and N. O. Jensen, 2008: Turbulence spectra, shear stress and turbulent kinetic energy budgets above two beech forest sites in Denmark. *Tellus*, **60B**, 179–187, doi:10.1111/j.1600-0889.2007.00326.x.

Marques Filho, E., L. D. A. Sá, H. Karam, R. Alvalá, A. Souza, and M. Pereira, 2008: Atmospheric surface layer characteristics of turbulence above the Pantanal wetland regarding the similarity theory. *Agric For Meteorol*, **148**, 883–892, doi:10.1016/j.agrformet.2007.12.004.

Martins, C., O. Moraes, O. Acevedo, and G. Degrazia, 2009: Turbulence intensity parameters over a very complex terrain. *Boundary-Layer Meteorol*, **133 (1)**, 35–45, doi:10.1007/s10546-009-9413-3.

Mauritsen, T., and G. Svensson, 2007: Observations of stably stratified shear-driven atmospheric turbulence at low and high richardson numbers. *J Atmos Sci*, **64**, 645–655, doi:10.1175/JAS3856.1.

Mauritsen, T., G. Svensson, S. S. Zilitinkevich, I. Esau, L. Enger, and B. Grisogono, 2007: A total turbulent energy closure model for neutrally and stably stratified atmospheric boundary layers. *J Atmos Sci*, **64 (11)**, 4113–4126, doi:10.1175/2007JAS2294.1.

McBean, G., and J. Elliot, 1975: Vertical transports of kinetic energy by turbulence and pressure in the boundary layer. *J Atmos Sci*, **32**, 753–766.

McMillen, R., 1988: An eddy correlation technique with extended applicability to non-simple terrain. *Boundary-Layer Meteorol*, **43**, 231–245.

Metzger, M., and H. Holmes, 2008: Time scales in the unstable atmospheric surface layer. *Boundary-Layer Meteorol*, **126 (1)**, 29–50, doi:10.1007/s10546-007-9219-0.

Meyers, T., and D. D. Baldocchi, 1991: The budgets of turbulent kinetic energy and Reynolds stress within and above a deciduous forest. *Agric For Meteorol*, **50**, 1–16.

Miller, N. E., and R. Stoll, 2013: Surface heterogeneity effects on regional-scale fluxes in the stable boundary layer: Aerodynamic roughness length transitions. *Boundary-Layer Meteorol*, **149**, 277–301, doi:10.1007/s10546-013-9839-5.

Mironov, D. V., and P. P. Sullivan, 2010: Effect of horizontal surface temperature heterogeneity on turbulent mixing in the stably stratified atmospheric boundary layer. *Proc. 19th Symp on Boundary Layers and Turbulence*, CO, USA, paper 6.3, 10 pp, Amer. Meteor. Soc.

Mölder, M., A. Grelle, A. Lindroth, and S. Halldin, 1999: Flux-profile relationships over a boreal forest-roughness sublayer corrections. *Agric For Meteorol*, **98-99**, 645–658, doi:10.1016/s0168-1923(99)00131-8.

Moncrieff, J., R. Clement, J. Finnigan, and T. Meyers, 2004: *Averaging, detrending, and filtering of eddy covariance time series*, 7–31. Lee, X., Massman, W. and Law, B. (editors), Kluwer Academic Publishers, Dordrecht, The Netherlands.

Monin, A., and A. Obukhov, 1954: Basic laws of turbulent mixing in the ground layer of the atmosphere. *Trudy Geofiz Inst Akad Nauk SSSR*, **151**, 163–187.

Monteith, J. L., and M. H. Unsworth, 1990: *Principles of environmental physics*. 2nd ed., Edward Arnold, London, 291 pp.

Moore, C., 1986: Frequency response corrections for eddy correlation systems. *Boundary-Layer Meteorol*, **37**, 17–35.

Moraes, O. L. L., O. C. Acevedo, G. A. Degrazia, D. Anfossi, R. da Silva, and V. Anabor, 2005: Surface layer turbulence parameters over a complex terrain. *Atmos Environ*, **39**, 3103–3112, doi:10.1016/j.atmosenv.2005.01.046.

Nadeau, D. F., E. R. Pardyjak, C. W. Higgins, and M. B. Parlange, 2013: Similarity scaling over a steep Alpine slope. *Boundary-Layer Meteorol*, **147**, 401–419, doi:10.1007/s10546-012-9787-5.

Nakamura, R., and L. Mahrt, 2001: Similarity theory for local and spatially averaged momentum fluxes. *Agric For Meteorol*, **108**, 265–279.

Nappo, C., 2012: *An Introduction to Atmospheric Gravity Waves*. 2nd ed., Academic Press, New York, 359 pp.

Nieuwstadt, M. T. F., 1984: The structure of the stable, nocturnal boundary layer. *J Atmos Sci*, **41 (14)**, 2202–2216, doi:10.1175/1520-0469(1984)041⟨2202:TTSOTS⟩2.0.CO;2.

Nilsson, E., F. Lohou, M. Lothon, E. Pardyjak, L. Mahrt, and C. Darbieu, 2015: Turbulence Kinetic Energy budget during the afternoon transition - Part 1: Observed surface tke budget and boundary layer description for 10 intensive observation period days. *Atmos. Chem. Phys. Discuss.*, **15**, 29 747–29 805, doi:10.5194/acpd-15-29747-2015.

Obukhov, A. M., 1946: Turbulence in the atmosphere with a non-uniform temperature. *Trudy Inst Theoret Geophys Akad Nauk SSSR*, **1**, 95–115 (translation in: *Boundary–Layer Meteorol* 1971, 2:7–29), doi:10.1007/BF00718085.

Olesen, H., S. Larsen, and J. Hojstrup, 1984: Modelling velocity spectra in the lower part of the planetary boundary layer. *Boundary-Layer Meteorol*, **29**, 285–312.

Oncley, S., C. Friehe, J. LaRue, J. Businger, E. Itsweire, and S. Chang, 1996: Surface-layer fluxes, profiles, and turbulent measurements over uniform terrain under near-neutral conditions. *J Atmos Sci*, **53**, 1029–1044.

Oncley, S. P., J. A. Businger, E. C. Itsweire, C. A. Friehe, J. C. LaRue, and S. S. Chang, 1990: Surface layer profiles and turbulence measurements over uniform land under near-neutral conditions. *Proc. 9th Symp. on Boundary Layer and Turbulence*, Roskilde, Denmark, Amer. Meteor. Soc.

Pahlow, M., M. Parlange, and F. Porté-Agel, 2001: On Monin-Obukhov similarity in the stable atmospheric boundary layer. *Boundary-Layer Meteorol*, **99**, 225–248, doi:10.1023/A:1018909000098.

Panofsky, H. A., and J. A. Dutton, 1984: *Atmospheric Turbulence: Models and Methods for Engineering Applications*. John Wiley and Sons: New York, 397 pp.

Piper, M., and J. K. Lundquist, 2004: Surface layer turbulence measurements during a frontal passage. *J Atmos Sci*, **61 (14)**, 1768–1780, doi:10.1175/1520-0469(2004)061⟨1768:SLTMDA⟩2.0.CO;2.

Pope, S., 2000: *Turbulent flows*. Cambridge University Press, Cambridge, UK, 771 pp.

Poulos, G. S., and Coauthors, 2002: CASES-99: A comprehensive investigation of the stable nocturnal boundary layer. *Bull Amer Meteorol Soc*, **83**, 555–581.

Rannik, Ü., 1998: On the surface layer similarity at a complex forest site. *J Geophys Res*, **103 (D8)**, 8685–8697, doi:10.1029/98JD00086.

Rannik, U., and T. Vesala, 1999: Autoregressive filtering versus linear detrending in estimation of fluxes by the eddy covariance method. *Boundary-Layer Meteorol*, **91**, 256–280.

Raupach, M., 1979: Anomalies in flux-gradient relationships over forest. *Boundary-Layer Meteorol*, **16**, 467–486.

Raupach, M., 1981: Turbulence in and above plant canopies. *Ann Rev Fluid Mech*, **13**, 97–129.

Raupach, M., 1994: Simplified expressions for vegetation roughness length and zero-plane displacement as function of canopy height and area index. *Boundary-Layer Meteorol*, **71 (1)**, 211–216, doi:10.1007/BF00709229.

Raupach, M., P. Coppin, and B. Legg, 1986: Experiments on scalar dispersion within a model plant canopy. Part I: the turbulence structure. *Boundary-Layer Meteorol*, **35**, 21–52.

Raupach, M., J. Finnigan, and Y. Brunei, 1996: Coherent eddies and turbulence in vegetation canopies: The mixing layer analogy. *Boundary-Layer Meteorol.*, **78**, 351–382, doi:10.1007/BF00120941.

Reynolds, O., 1895: On the dynamical theory of incompressibile viscous fluids and the determination of the criterion. *Phil Trans R Soc Lond A*, **186**, 123–164.

Richardson, L. F., 1920: The supply of energy from and to atmospheric eddies. *Proc R Soc Lond A*, **97**, 354–373.

Rotach, M. W., 1993: Turbulence colse to a rough urban surface part II: Variances and gradients. *Boundary-Layer Meteorol*, **66 (1)**.

Rotach, M. W., M. Andretta, P. Calanca, A. P. Weigel, and A. Weiss, 2008: Boundary layer characteristics and turbulent exchange mechanisms in highly complex terrain. *Acta Geophys*, **56 (1)**, doi:10.2478/s11600-007-0043-1.

Rotach, M. W., and P. Calanca, 2014: *Microclimate*, Vol. 1, 258–264. Gerald R. North (editor-in-chief), John Pyle and Fuqing Zhang (editors), Academic Press.

Rotach, M. W., and Coauthors, 2004: Turbulence structure and exchange processes in an Alpine valley: The Riviera project. *Bull Am Meteorol Soc*, **85**, 1367–1385, doi: 10.1175/BAMS-85-9-1367.

Roth, M., 2000: Review of atmospheric turbulence over cities. *Q J R Meteorol Soc*, **126**, 941–990.

Roth, M., J. A. Salmond, and A. N. V. Satyanarayana, 2006: Methodological considerations regarding the measurement of turbulent fluxes in the urban roughness sublayer: The role of scintillometery. *Boundary-Layer Meteorol*, **121 (2)**, 351–375, doi: 10.1007/s10546-006-9074-4.

Sakai, R. K., D. Fitzjerrald, and K. Moore, 2001: Importance of low-frequency contributions to the eddy fluxes observed over rough surfaces. *J Appl Meteorol*, **40**, 2178–2192.

Salmond, J., 2005: Wavelet analysis of intermittent turbulence in a very stable nocturnal boundary layer: implications for the vertical mixing of ozone. *Boundary-Layer Meteorol*, **114**, 463–488, doi:10.1007/s10546-004-2422-3.

Sanz Rodrigo, J., and S. P. Anderson, 2013: Investigation of the stable atmospheric boundary layer at Halley Antarctica. *Boundary-Layer Meteorol*, **148**, 517–539, doi:10.1007/s10546-013-9831-0.

Shaw, R., Y. Brunet, J. Finnigan, and M. Raupach, 1995: A wind tunnel study of air flow in waving wheat: Two-point velocity statistics. *Boundary-Layer Meteorol*, **76**, 349–376.

Shaw, R., J. Finnigan, and E. Patton, 2006: Eddy structure near the plant canopy interface. *17th Symposium on Boundary Layers and Turbulence*, J2.1.

Shaw, R., R. Silversides, and G. Thurtell, 1974: Some observations of turbulence and turbulent transport within and above plant canopies. *Boundary-Layer Meteorol*, **5**, 429–449.

Simpson, I., G. W. Thurtell, H. H. Neumann, G. Den Hartog, and G. C. Edwards, 1998: The validity of similarity theory in the roughness sublayer above forests. *Boundary-Layer Meteorol*, **87**, 69–99.

Sorbjan, Z., and A. A. Grachev, 2010: An evaluation of the flux-gradient relationship in the stable boundary layer. *Boundary-Layer Meteorol*, **135 (3)**, 385–405, doi:10.1007/s10546-010-9482-3.

Sozzi, R., and M. Favaron, 1997: Sonic anemometry and thermometry: Theoretical basis and data-processing software. *Environ Software*, **11**, 259–270.

Sreenivasan, K., A. Chambers, and R. Antonia, 1978: Accuracy of moments of velocity and scalar fluctuations in the atmospheric surface layer. *Boundary-Layer Meteorol*, **14**, 341–359.

Stiperski, I., and M. W. Rotach, 2016: On the measurement of turbulence over complex mountainous topography. *Boundary-Layer Meteorol*, **159**, 97121, doi:10.1007/s10546-015-0103-z.

Stoll, R., and F. Porté-Agel, 2009: Surface heterogeneity effect on regional-scale fluxes in stable boundary layers: Surface temperature transitions. *J Atmos Sci*, **66**, 412–431, doi:10.1175/2008JAS668.1.

Stull, R. B., 1988: *An Introduction to Boundary-Layer Meteorology*. Kluwer Academic Publishers: Dordrecht, 680 pp.

Su, H.-B., H. P. Schmid, C. S. B. Grimmond, C. S. Vogel, and A. J. Oliphant, 2004: Spectral characteristics and correlation of long-term eddy-covariance measurements over two mixed hardwood forests in non-flat terrain. *Boundary-Layer Meteorol*, **110**, 213–253.

Sun, J., and Coauthors, 2002: Intermittent turbulence associated with a density current passage in the stable boundary layer. *Boundary-Layer Meteorol*, **105**, 199–219.

Terradellas, E., G. Morales, J. Cuxart, and C. Yague, 2001: Wavelet methods: application to the study of the stable boundary layer under non-stationary conditions. *Dyn Atmos Oceans*, **34**, 225–244.

Terradellas, E., M. Soler, E. Ferreres, and M. Bravo, 2005: Analysis of oscillations in the stable atmospheric boundary layer using wavelet methods. *Boundary-Layer Meteorol*, **114**, 489–518.

Thom, A., J. Stewart, H. Oliver, and J. Gash, 1975: Comparison of aerodynamic and energy budget estimates of fluxes over a pine forest. *Q J R Meteorol Soc*, **101**, 93–105, doi:10.1002/qj.49710142708.

Torrence, C., and G. P. Compo, 1998: A practical guide to wavelet analysis. *Bull Amer Meteorol Soc*, **79 (1)**, doi:10.1175/1520-0477(1998)079⟨0061:APGTWA⟩2.0.CO;2.

Townsend, A. A., 1961: Equilibrium layers and wall turbulence. *J Fluid Mech*, **11**, 97–120.

Trini Castelli, S., and S. Falabino, 2013: Analysis of the parameterization for the wind-velocity fluctuation standard deviations in the surface layer in low-wind conditions. *Meteorol Atmos Phys*, **119 (1-2)**, 91–107, doi:10.1007/s00703-012-0219-3.

van de Wiel, B., A. Moene, O. K. Hartogensis, H. A. R. DeBruin, and A. A. M. Holtslag, 2003: Intermittent turbulence and oscillations in the stable boundary layer over land. Part III. A classification for observations during CASES-99. *J Atmos Sci*, **60**, 2509–2522.

van de Wiel, B., A. Moene, G. Steeneveld, P. Baas, F. Bosveld, and A. A. M. Holtslag, 2010: A conceptual view on inertial oscillations and nocturnal low-level jets. *J Atmos Sci*, **67**, 2679–2689, doi:10.1175/2010JAS3289.1.

van de Wiel, B., A. Moene, G. J. Steeneveld, O. K. Hartogensis, and A. A. M. Holtslag, 2007: Predicting the collapse of turbulence in stably stratified boundary layers. *Flow Turb Combust*, **79**, 251–274.

van den Kroonenberg, A., and J. Bange, 2007: Turbulent flux calculation in the polar stable boundary layer: Multiresolution flux decomposition and wavelet analysis. *J Geophys Res Atmos*, **112**, D06 112, doi:10.1029/2006JD007819.

van der Hoven, I., 1957: Power spectrum of horizontal wind speed in the frequency range from 0.0007 to 900 cycles per hour. *J Meteorol*, **14**, 160–164.

Van Gorsel, E., 2003: Aspects of flow characteristics and turbulence in complex terrain. Dissertation, University of Basel, Switzerland, 58 pp.

Večenaj, Ž., D. Belušić, and B. Grisogono, 2010: Characteristics of the near-surface turbulence during a bora event. *Ann Geophys*, **1**, 155–163.

Večenaj, Ž., D. Belušić, V. Grubišić, and B. Grisogono, 2012: Along-coast features of bora-related turbulence. *Boundary-Layer Meteorology*, **143 (3)**, 527–545, doi:10.1007/s10546-012-9697-6.

Večenaj, Ž., S. F. J. De Wekker, and V. Grubišić, 2011: Near-surface characteristics of the turbulence structure during a mountain-wave event. *J Appl Meteor Climatol*, **50**, 1088–1106, doi:10.1175/2010JAMC2450.1.

Vercauteren, N., L. Mahrt, and R. Klein, 2016: Investigation of interactions between scales of motion in the stable boundary layer. *Q J R Meteorol Soc*, doi:10.1002/qj.2835.

Večenaj, Ž., and S. F. J. De Wekker, 2015: Determination of non-stationarity in the surface layer during the T-REX experiment. *Q J R Meteorol Soc*, **141**, 1560–1571, doi:10.1002/qj.2458.

Vickers, D., and L. Mahrt, 2003: The cospectral gap and turbulent flux calculations. *J Atmos Ocean Technol*, **20**, 660–672, doi:10.1175/1520-0426(2003)20⟨660:TCGATF⟩2.0.CO;2.

Wieringa, J., 1976: An objective exposure correction method for average wind speeds measured at a shelter location. *Q J R Meteorol Soc*, **102**, 241–253.

Wilczak, J., S. Oncley, and S. Stage, 2001: Sonic anemometer tilt correction algorithms. *Boundary-Layer Meteorol*, **99**, 127–150, doi:10.1023/A:1018966204465.

Willis, G. E., and J. W. Deardorff, 1976: On the use of taylor's translation hypothesis for diffusion in the mixed layer. *Quarterly Journal of the Royal Meteorological Society*, **102 (434)**, 817–822.

Wood, C., and Coauthors, 2010: Turbulent flow at 190 m height above London during 2006-2008: a climatology and the applicability of similarity theory. *Boundary-Layer Meteorol*, **137**, 77–96, doi:10.1007/s10546-010-9516-x.

Wyngaard, J., 1975: Modeling the planetary boundary layer - Extension to the stable case. *Boundary-Layer Meteorol*, **9 (4)**, 441–460, doi:10.1007/BF00223393.

Wyngaard, J., 2010: *Turbulence in the atmosphere*. Cambridge University Press: Cambridge, 393 pp.

Wyngaard, J., and O. Coté, 1971: The budgets of turbulent kinetic energy and temperature variance in the atmospheric surface layer. *J Atmos Sci*, **28**, 190–201, doi:10.1175/1520-0469(1971)028⟨0190:TBOTKE⟩2.0.CO;2.

Wyngaard, J., and O. Coté, 1972: Cospectral similarity in the atmospheric surface layer. *Q J R Meteorol Soc*, **98 (417)**, 590–603, doi:10.1002/qj.49709841708.

Wyngaard, J., O. Coté, and Y. Izumi, 1971: Local free convection, similarity and the budgets of shear stress and heat flux. *J Atmos Sci*, **28**, 1171–1182, doi:10.1175/1520-0469(1971)028⟨1171:LFCSAT⟩2.0.CO;2.

Wyngaard, J. C., 1973: *On surface layer turbulence*, 135–141. Haugen, D.A. (editor).

Yang, B., A. Morse, R. Shaw, and K. T. Paw U, 2006: Large eddy simulation of turbulent flow across a forest edge. Part II: momentum and turbulent kinetic energy budgets. *Boundary-Layer Meteorol*, **121**, 433–457.

Zilitinkevich, S., T. Elperin, N. Kleeorin, and I. Rogachevskii, 2007: Energy- and flux-budget (efb) turbulence closure moel for stably stratified flows. part I: steady-state, homogeneous regimes. *Boundary-Layer Meteorol*, **125 (2)**, 167–191.

Zilitinkevich, S., I. Esau, N. Kleeorin, I. Rogachevskii, and R. Kouznetsov, 2010: On the velocity gradient in the stably stratified sheared flows. part I: asymptotic analysis and applications. *Boundary-Layer Meteorol*, **135 (3)**, 505–511.

Acknowledgments

First of all, I would like to express my gratitude to my supervisor Zvjezdana Bencetić Klaić. I am thankful for the great deal of trust that she had in me and for believing I had all the necessary skills to tackle this challenging topic. She gave me all the possible freedom to find my own way in the field, which helped me to develop my own ideas. Her support to go abroad and exchange with the top researchers in the field as well as all the benevolent advices on the way are highly appreciated.

This thesis would have never been possible without the support of one person - Mathias Rotach. Mathias hosted my stay at the Institute of Atmospheric and Cryospheric Sciences (AcInn) at University of Innsbruck in Innsbruck, where I spent 13 months in total during my PhD. The collaboration with Mathias was crucial for successful delivery of many results presented in this thesis. I am thankful for the support he provided during the last few years, many scientific discussions and for having his door always open when a problem arose. Most of all, I am grateful for the opportunity to work with him and to learn from him as he is an amazing scientist of great scientific curiosity and expertize. Thank you, Mathias. I am forever indebted.

Special thanks go to Željko Večenaj and Ivana Stiperski who supported me each in his own way. I am deeply thankful to Željko for his help especially during the first few years. He gave me guidance regarding the data analysis tools and procedures as well as helped to obtain the first results of this work. He helped in many occasions when I needed someone to discuss and clarify certain things for myself, which I appreciate. Ivana welcomed me in her office during my stay at AcInn and was the best office mate one can wish for. During this time through our daily exchange of thoughts and ideas I have learned a lot from her. Besides, she provided encouragement and support in moments when I needed it.

Many thanks go to my professors Branko Grisogono and Darko Koračin. Branko has been my professor since my undergraduate studies and has contributed significantly to my professional development through constantly challenging me to be the best I can be. I would like to thank Darko for evaluating my thesis and providing encouragement in this last phase.

Maja Telišman Prtenjak was my diploma thesis supervisor and she will always be a role

model of what a great mentor should be. During my PhD she showed a great support and was always there to advise me when needed. Thank you for including me in many different activities within the Croatian meteorological research community and for many fun moments we had. I would like to thank Danijel Belušić for introducing me to a worldwide leading scientist on stable boundary layer Larry Mahrt during the Boundary Layers and Turbulence Symposium in Leeds, UK. This was one of the highlights of my PhD. The support I got from Andrey A. Grachev is highly appreciated. It was always a pleasure to meet him at a conference in different parts of the world and to receive his ideas on stable boundary layer and my work.

Many thanks to Lukas Strauss, Johannes Sachsperger and Nevio Babić for the inspiration and motivation they provided. Big thanks go to all AcInn members who made me feel like at home during my time in Innsbruck, especially to Wolfgang Gurgiser, Anna Wirbel, Lindsey Nicholson and Markus Dabernig. The support provided by the Scholarship Foundation of the Republic of Austria through the Scholarship for Undergraduates, Graduates and Postgraduates and by the Austrian Federal Ministry of Science, Research and Economy (BMWFW) through the Ernst Mach Grant - Worldwide is greatly appreciated.

Finally, my deepest gratitude goes to my family and friends whose support and love during all these years was crucial for my success. I have been sharing this journey with my dear friends Martina and Dražen, Nikolina, Petra, Gabrijela and Goran and I hope we will do this for many years to come. I am deeply thankful to Mihael for the everyday support he provides, and for believing in me and encouraging me at the most important moment. To my parents and sister for their constant love and support to choose my own way knowing that they will always be there for me, which is essential for my happiness and personal growth. My love for you is immense.

Zagreb, September 2016
Karmen Babić

Curriculum Vitae

Karmen Babić
University of Zagreb, Faculty of Science, Department of Geophysics
Horvatovac 95, 10000 Zagreb, Croatia
e-mail: *babick@gfz.hr*

Education

2011–2016	Ph.D. in Atmospheric Sciences at the Department of Geophysics, Faculty of Science, University of Zagreb.
2003–2010	Diploma in Meteorology and Physical Oceanography (Master of Physics–Geophysics). Diploma thesis *"Effects of sea/land breezes on deep convection development over Istria"* under the supervision of Dr. Telišman Prtenjak, Department of Geophysics, Faculty of Science, University of Zagreb.

Relevant courses

Jul 2015	Flux Measurements Fundamentals (Karlsruhe Institute of Technology, IMK-IFU, Garmisch-Partenkirchen, Germany)
Aug 2015	International Summer School on Global Greenhouse Gasses (School of Geosciences, University of Edinburgh, Edinburgh, Scotland)

Professional training

2015	Visiting scientist at the Institute of Atmospheric and Cryospheric Sciences, University of Innsbruck (9 months).
2014	Visiting scientist at the Institute of Atmospheric and Cryospheric Sciences, University of Innsbruck (former IMGI, 4 months).

Peer-Reviewed Publications

(1) **Babić, K.**, M. W. Rotach and Z. B. Klaić, 2016: Evaluation of Local Similarity Theory in the Wintertime Nocturnal Boundary Layer over Heterogeneous Surface. *Agric. For. Meteorol.*, **228**, 164–179.

(2) Klaić, Z. B., S. J. Ollier, **K. Babić**, I. Bešlić, 2015: Influences of outdoor meteorological conditions on indoor wintertime short-term PM1 levels. *Geofizika*, **32**(2), 237–264.

(3) Poljak, G., Telišman Prtenjak, M., Kvakić, M., Strelec Mahović, N. and **Babić, K.**, 2014: Impact of the large-scale wind and mesoscale shallow flows on the cumulonimbus cloud development over Istria, *Ann. Geophys.*, **32**, 401–420.

(4) **Babić, K**., Bencetić Klaić, Z. and Večenaj, Ž., 2012: Determining a turbulence averaging time scale by Fourier analysis for the nocturnal boundary layer. *Geofizika*, **29**(1); 35–51.

(5) **Babić**, K., Mikuš, P. and Telišman Prtenjak, M., 2012: The relationship between shallow thermal circulation regimes and cumulonimbus clouds along the northeastern Adriatic coast. *Geofizika*, **29**(1); 103–120.

Selected Conference and Workshop Presentations

• Local Similarity Scaling in the Nocturnal Boundary Layer over Heterogeneous Terrain. *22nd Symposium on Boundary Layers and Turbulence.* Salt Lake City, Utah, USA, 20–24 June 2016.

• Turbulence Spectra, Dissipation and Turbulent Kinetic Energy Budgets in the Stable Boundary Layer over Inhomogeneous Terrain. *22nd Symposium on Boundary Layers and Turbulence.* Salt Lake City, Utah, USA, 20–24 June 2016. (Poster)

• Evaluating local similarity scaling in the stable, wintertime boundary layer influenced by complex topography. *33rd International Conference on Alpine Meteorology.* Innsbruck, Austria, 31 August–4 September 2015.

• Timescales in the nocturnal, wintertime boundary layer over heterogeneous surface. *21st Symposium on Boundary Layers and Turbulence.* Leeds, Great Britain, 9–13 June 2014.

• Observations of turbulence in the stable surface layer over inhomogeneous terrain. *32nd International Conference on Alpine Meteorology.* Kranjska Gora, Slovenia, 3–7 June 2013.

• Analysis of convective indices over the northeastern Adriatic. *Croatian–USA Workshop on Mesometeorology.* Zagreb, Croatia, 18–20 June 2012.

Awards and Scholarships

2016	Best Student Poster Award by the American Meteorological Society, 22nd Symposium on Boundary Layers and Turbulence, Salt Lake City, Utah
2016	Young Meteorologist Award by Croatian Meteorological Society
2015	ClimMani Travel Award
01–09/2015	Ernst Mach Grant Worldwide
02–05/2014	Scholarship of the Scholarship Foundation of the Republic of Austria for Undergraduates, Graduates and Postgraduates
2013	*Young Scientist Travel Award* by European Meteorological Society for the presentation at International Conference on Alpine Meteorology, 3–7 June 2013, Kranjska Gora, Slovenia
2009	University of Zagreb Rector's Award for the student paper: *"Interaction between the sea-breeze and the cumulonibus cloud over Istria during summer months"*

Skills

Programming	Fortran, Matlab
Data analysis	High-frequency data analysis (towers), Numerical model output analysis, Time series analysis, Spectral analysis, Wavelet analysis
Applications	Microsoft office, Libre Office, LaTeX, Inkscape, Eddy-Covariance Softwares: EdiRe, TK3

Teaching experience

2012–Present	Dynamic meteorology I, II and III
2013–2014	Introduction to geophysical fluid dynamics
2011–2013	Weather analysis and forecasting I and II

Scientific memberships

2012–Present	American Geophysical Union, American Meteorological Society, Royal Meteorological Society
2011–Present	European Geosciences Union, Croatian Meteorological Society